論文 / 著書情報
Article / Book Information

題目(和文)	
Title(English)	Adsorbent fabrication from shrimp shell waste for sustainable shrimp cultivation through nutrient cycles
著者(和文)	YamsomphongKANOKWAN
Author(English)	Kanokwan Yamsomphong
出典(和文)	学位:博士(工学), 学位授与機関:東京科学大学, 報告番号:甲第342号, 授与年月日:2025年3月26日, 学位の種別:課程博士, 審査員:高橋 史武,CROSS JEFFREY SCOTT,吉村 千洋,江頭 竜一,中村 隆志
Citation(English)	Degree:Doctor (Engineering), Conferring organization: Institute of Science Tokyo, Report number:甲第342号, Conferred date:2025/3/26, Degree Type:Course doctor, Examiner:,,,,
学位種別(和文)	博士論文
Type(English)	Doctoral Thesis

Doctoral Dissertation

Adsorbent fabrication from shrimp shell waste for sustainable shrimp cultivation through nutrient cycles

By

Kanokwan YAMSOMPHONG

Academic advisor

Professor Dr. Fumitake TAKAHASHI

Thesis submitted for the degree of Doctor of Engineering

Department of Transdisciplinary Science and Engineering,

School of Environment and Society,

Institute of Science Tokyo

March 2025

Abstract

The shrimp cultivation produces significant wastes, including shrimp shell waste and nutrient-rich wastewater, posing environmental challenges. This study developed a sustainable shrimp shell-derived adsorbent (SSs), rich in Calcium (Ca), for phosphate (PO_4^{3-}) adsorption from shrimp aquaculture wastewater.

Furthermore, methyl Orange (MO) dye, selected as a model anionic pollutant, was employed to evaluate the SSs performance in wastewater treatment applications. The results revealed effective PO_4^{3-} adsorption and notable MO removal, highlighting its dual functionality in nutrient recovery and water purification. By transforming waste into high-value products, this "waste-to-wealth" strategy promotes sustainability and a circular system in the shrimp aquaculture. Future applications might include scalable wastewater treatment systems in shrimp cultivation and utilize the PO_4^{3-} adsorbed SSs as a sustainable fertilizer.

Keyword: Shrimp shell, Adsorption, Pyrolysis, phosphate, methyl Orange

Acknowledgment

Foremost, I would like to express my sincere gratitude to my advisor Prof. Fumitake Takahashi for his helpful guidance and support for my study and research. It has been a great pleasure and honor for having him as my supervisor. Also, I would like to express my gratitude to all my referees: Prof. Jeffrey S. Cross, Prof. Yoshimura Chihiro, Assoc. Prof. Egashira Ryuichi, and Assoc. Prof Takashi Nakamura for valuable suggestions and support to improve my work. I sincerely appreciate Yokoi Laboratory for providing the necessary equipment that greatly supported this research. I would like to thank you Mrs. Eriko Ohno for the administrative work during my study. I would be very pleased to express my gratitude to NSK Scholarship for the financial support and to TAIST-SciTokyo staffs for their administrative work regarding all the scholarship work. I would love to thank all my lab mates for the stimulating working environment and for all the fun we have had in the past years. Last but not least, I would be delighted to thank my friends and the most important to my family for their unconditional love and endless support.

Table of Contents

Abstract ii
Acknowledgment iii
Table of Contents iv
List of Figures vi
List of Tables viii
List of Abbreviations ix
Chapter 1 Introduction 1
1.1 Shrimp cultivation 1
1.1.2 Shrimp aquaculture production 2
1.1.3 Shrimp shell processing 3
1.2 Environmental issues in shrimp aquaculture 5
1.2.1 Shrimp waste generation 5
1.2.2 Shrimp aquaculture wastewater 5
1.3 Shrimp shell waste utilization 7
1.3.1 Shrimp shell waste utilization for wastewater application 8
1.4 Adsorbent-derived biochar for adsorption applications 9
1.4.1 Pyrolysis for biochar production 10
1.4.2 Biochar for water pollutant adsorption 11
1.5 Recent shrimp shell-derived biochar for adsorption applications 13
1.6 Research gap in shrimp shell derived-adsorbent in water pollutant removal 18
1.7 Objective of present work 18
1.8 Thesis structure 19
Chapter 2 Fabrication and characterization of the shrimp shell derived-adsorbent 22
2.1 Background 22
2.2 Fabrication of the shrimp shell-derived adsorbent 23
2.2.1 Materials 23
2.2.1 Fabrication method 23
2.3 Characterization of physical and chemical properties 24
2.3.1 Surface morphology and porosity 24
2.3.2 Surface chemistry 29
2.4 Chapter summary 33
Chapter 3 Phosphate Removal and Recovery 34
3.1 Background 34

3.2 Phosphate adsorption experiment 34
3.3 Phosphate removal performance 35
3.3.1 Comparison of adsorption performances 35
3.3.2 Adsorption kinetics 36
3.3.3 Adsorption isotherm 39
3.4 Adsorption thermodynamic 42
3.5 Adsorption mechanisms of phosphate onto shrimp shell-derived adsorbent 44
3.5.1 Ca^{2+}-induced chemical precipitation 45
3.5.2 Other mechanisms including ligand exchange and anion–π interaction. 48
3.6 Recovery of phosphate from real shrimp pond wastewater 50
3.7 Chapter summary 53
Chapter 4 Methyl orange removal 54
4.1 Background 54
4.2 Methyl orange adsorption experiment 54
4.3 MO removal performance 55
4.3.1 Comparison of adsorption performances 55
4.3.2 Adsorption kinetics 57
4.3.3 Adsorption Isotherm 59
4.4 Adsorption thermodynamics 62
4.5 MO desorption 64
4.6 Adsorption mechanisms 65
4.6.1 The large adsorption capacity of SSs for anionic MO 66
4.6.2 Dual characteristics including both reversible and irreversible adsorption proces 71
4.7 Chapter Summary 72
Chapter 5 Conclusion and recommendations 73
5.1 Overall conclusions 73
5.2 Recommendations 74
5.3 List of Publications 76
References 77
Appendix 95

List of Figures

Figure 1.1 Aquaculture shrimp production……2
Figure 1.2 Aquaculture shrimp production by country……3
Figure 1.3 Schematic presentation of shrimp processing……4
Figure 1.4 Nitrogen (N) and phosphorus (P) cycle in aquaculture shrimp pound…….....7
Figure 1.5 The preparation procedure of waste shrimp shell-based hydrochar……...9
Figure 1.6 Lab-scale pyrolysis set-up……10
Figure 1.7 Heavy metal adsorption mechanisms of biochar……..11
Figure 1.8 Nutrients adsorption mechanisms of biochar……...12
Figure 1.9 The chemical composition of crayfish/ crawfish and shrimp……...17
Figure 1.10 The thesis's content and its relationship……19
Figure 2.1 Appearance and SEM images of SSs……25
Figure 2.2 EDS mapping of the SSs under different modification methods. ……26
Figure 2.3 N_2 adsorption–desorption isotherms (BET) diagram for SSs at different modification methods……27
Figure 2.4 Zeta potential of SSs with different modification conditions……28
Figure 2.5 XRD pattern of SSs with different modification conditions……29
Figure 2.6 FT-IR spectra of SSs with different modification conditions……..30
Figure 2.7 XPS spectra of SSs with different modification conditions……31
Figure 3.1 Adsorption data of PO_4^{3-} onto SSs……..34
Figure 3.2 Adsorption of PO_4^{3-} by using SSs with different modification……38
Figure 3.3 Adsorption isotherm of PO_4^{3-} by using SSs with different modification……40
Figure 3.4 Adsorption thermodynamic of PO_4^{3-} by using SSs with different modification…43
Figure 3.5 Distribution of PO_4^{3-} species in varying pH conditions……...44
Figure 3.6 XRD pattern of SSs with different modification conditions before and after PO_4^{3-} adsorption…...……..45
Figure 3.7 FT-IR spectra of SSs before and after PO_4^{3-} adsorption……..46
Figure 3.8 XPS spectra of SSs before and after PO_4^{3-} adsorption ……46
Figure 3.9 Non-covalent interactions involving π systems……..47
Figure 4.1 Adsorption data of MO onto SSs……..54
Figure 4.2 Adsorption kinetics of MO adsorption by SSs……57

Figure 4.3 Adsorption isotherm of MO by using SSs with different modification……...60
Figure 4.4 K 2p XPS spectra of SSs before and after MO adsorption……..61
Figure 4.5 Adsorption thermodynamic of MO by using SSs with different modification..……63
Figure 4.6 MO desorption/adsorption ratio by SSsCA at different concentration (100 and 1000 mg/L) and pH (2 and 9)…….……64
Figure 4.7 XPS spectra of SSs before and after MO adsorption……67
Figure 4.8 FTIR spectra of each SSs before and after MO adsorption……..67
Figure 4.9 The relation between q_{max} and S_{BET} and external surface area..…….…….69
Figure 4.10 Adsorption kinetics of MO adsorption (1000 mg/L) by SSsCA……..…..…….69
Figure 4.11 An illustration of the concept of irreversibility at high MO concentration system..71
Figure 5.1 Proposed shrimp cultivation wastewater treatment.……76

List of Tables

Table 1.1 Shrimp shell waste in wastewater treatment applications……..……9
Table 1.2 Various types of biochar and their potential for the adsorption of heavy metals and nutrients..……..13
Table 1.3 Thermochemical conversion methods and properties of shrimp shell biochars……...……14
Table 1.4 Application of shrimp shell biochars as adsorbent for removal of contaminants from wastewater…….……...……..15
Table 2.1 Chemical composition of raw shrimp shell by XRF analysis……..23
Table 2.2 Specific surface area, external surface area, and total pore volume of the raw shrimp shell and SSs……...27
Table 3.1 Experimental data and standard errors of PO_4^{3-} (300 mg/L) adsorption capacity for each SSs as a function of time……...35
Table 3.2 Adsorption kinetic models……..36
Table 3.3 Adsorption kinetic parameters for SSs at 20 ℃……...…..…….37
Table 3.4 Adsorption isotherms models…….38
Table 3.5 Adsorption kinetic isotherm parameters for SSs at 20 ℃……..39
Table 3.6 Comparison of the adsorption performances of PO_4^{3-} with other reported crustacean based-biochars……..41
Table 3.7 Thermodynamic parameters for SSsCA…….……42
Table 3.8 Possible PO_4^{3-} adsorption mechanism in each SSs…….……48
Table 4.1 Experimental data and standard errors of MO adsorption (1000 mg/L) capacity for each SSs as a function of time……55
Table 4.2 Adsorption kinetics models…….56
Table 4.3 Adsorption kinetic parameters for SSs at 20 ℃…….57
Table 4.4 Adsorption isotherms models…….……58
Table 4.5 Adsorption kinetic parameters……59
Table 4.6 Comparison of the adsorption performances of MO with other reported biochars ……61
Table 4.7 Thermodynamic parameters……...62
Table 4.8 Comparison of adsorption characteristics……..…….…...70

List of Abbreviations

Ca^{2+}	Calcium ion
$CaCO_3$	Calcium carbonate
HDL	Hydroxylellestadite
CSH	calcium silicate hydrate
KSC	Potassium sodium calcium chloride carbonate hydrate
KOH	Potassium hydroxide
SSs	Shrimp shell derived-adsorbent
SSsN	Shrimp shell-derived adsorbent pyrolyzed at 700 °C
SSsH	Shrimp shell-derived adsorbent pyrolyzed at 800 °C
SSsCA	Shrimp shell-derived adsorbent pyrolyzed at 700°C with $Ca(OH)_2$ activation
SSsK	Shrimp shell-derived adsorbent pyrolyzed at 700°C with KOH activation
MO	Methyl orange
PO_4^{3-}	Phosphate
P	Phosphorous
N	Nitrogen
Monocalcium phosphate	$Ca(H_2PO_4)_2$
Dicalcium phosphate	$CaHPO_4$
SEM	Scanning electron microscope
XRD	X-ray diffraction
FTIR	Fourier-transform infrared
XPS	X-ray photoelectron spectroscopy

Chapter 1 Introduction

1.1 Shrimp cultivation

Shrimp is a popular seafood item, with high consumer demand. They are obtained via two methods: shrimp catching (wild capture), and shrimp cultivation (farming or aquaculture). Shrimp catching is a traditional method of harvesting wild shrimp from their natural habitats such as oceans, rivers, and estuaries, whereas shrimp farming uses controlled environments to grow shrimp in ponds, tanks, or other aquatic systems. Wild shrimp catching has been a challenge and has dropped dramatically because of overfishing, habitat destruction, and seasonal limitations. According to Food and Agriculture Organization (FAO) (2020) [7], the global shrimp catch reached 3.35 million tons in 2003, and there has been no increasing trend According to FAO (2020), suggesting no significant growth in global shrimp production from shrimp catching over the years. Therefore, the shift from shrimp catching to shrimp farming occurred largely in the shrimp production to meet growing global demand and ensure long-term productivity. Expansion of the aquaculture is crucial for ending overfishing by 2020, following Sustainable Development Goals (SDGs) [8]

Shrimp cultivation, also known as shrimp aquaculture, is the farming of shrimp or prawns in controlled aquatic environments. It is a rapidly expanding sector of the aquaculture industry, due to its sustainable and high-yield production. Shrimp farming systems can yield up to 15–25 tons per hectare per cycle, compared to the limited availability of wild shrimp stocks (2–10 kg of bycatch per kg of shrimp) [9]. Shrimp farming involves three main systems with differences in scale, technology, and environmental impact including extensive, semi-intensive and intensive systems [10]. While intensive systems generate large yields, they also pose environmental issues and necessitate appropriate environmental management for the generated wastewater and waste. Extensive and semi-intensive systems are typically more environmentally friendly but yield lower production [10, 11]. Each type contributes to the growing global shrimp farming industry, and many producers attempt to maintain a balance between profitability and sustainability, especially as shrimp demand rises globally.

In 2018, shrimp farming accounted for 63.5% of total shrimp production. Shrimp farms occupied an estimated 3.490 million hectares (Mha), and 2.426 Mha were assigned to production ponds, with an annual increase of 3−5%. The extensive shrimp farms occupied 1.804 Mha of farm area and produced 11.4% of global shrimp production, including 1.377 Mha of producing ponds. Semi-intensive and intensive farming areas combined accounted for 1.049

Mha of the global shrimp pond areas. Shrimp pond aquaculture is essential for supplying the increasing global demand for shrimp, and sustainable practices are necessary to reduce its environmental impact.

1.1.2 Shrimp aquaculture production

Shrimp aquaculture is one of the leading contributors to the global food production industry due to its high demand and market value [7].The global shrimp production has shown significant expansion in recent decades (See **Figure 1.1**). In 1980, production was around 70,000 tones. By 1990, this had dramatically increased to 700,000 tones, signifying a tenfold augmentation within a decade. By the year 2000, production surpassed 1 million tones (Mt). The upward trend continued, attaining 3.6 Mt in 2010 and reaching a peak of 6.0 Mt by 2019. In 2020, the global shrimp production was projected to reach 5.1 Mt, with a compound annual growth rate (CAGR) of 6.1% from 2020 to 2026 [12]. This decline in 2020 was largely attributed to the disruptions caused by the COVID-19 pandemic. The annual production is expected to rise, and it is estimated to be around 7.28 Mt in 2025 [12, 13]. This remarkable growth has been influenced by the expansion of shrimp aquaculture, which has steadily replaced shrimp catching as the predominant source of global shrimp supply.

Figure 1.1 Aquaculture shrimp production.

The increase in production from 1980 to 2000 was mainly for *P. monodon* (giant tiger prawn) in Asia. However, the introduction of *L. vannamei* (pacific white shrimp) in Asia drastically transformed worldwide shrimp production, and it exceeded that of *P. monodon* by 2004. In 2010, 73.9% of shrimp aquaculture production derived from *L. vannamei*. In 2018,

global shrimp production rose markedly, with *L. vannamei* constituting 82.7% of the total, *P. monodon* contributing 12.5%, and 4.8% coming from other species. This transition highlights the importance of *L. vannamei* in current shrimp aquaculture, because of its rapid growth, adaptability, and enhanced productivity in intensive farming systems.

Global farmed shrimp production originated from 59 countries. However, six countries —China, Ecuador, India, Indonesia, Thailand, and Vietnam—each exceeded 300,000 tones and accounted for 88.1% of global aquaculture production. These countries also provided 83.6% of *L. vannamei* and 80.1% of *P. monodon* production. On the other hand, the remaining around 12% is produced mostly from Latin America, especially Brazil, and Mexico. China is the top producer of farmed shrimp in Asia, growing almost 2.12 Mt in 2019. In Southeast Asia, Indonesia produced over 0.93 Mt in 2029, follow by Vietnam (0.88 Mt). Thailand's farmed shrimp production was 0.38 Mt, and Thailand is the largest exporter of farmed shrimp to the USA, Europe, Canada, Japan, and South Korea [14]. As part of In Latin America, Ecuador had the largest output with 1.3 Mt in 2021 (**Figure 1.2**).

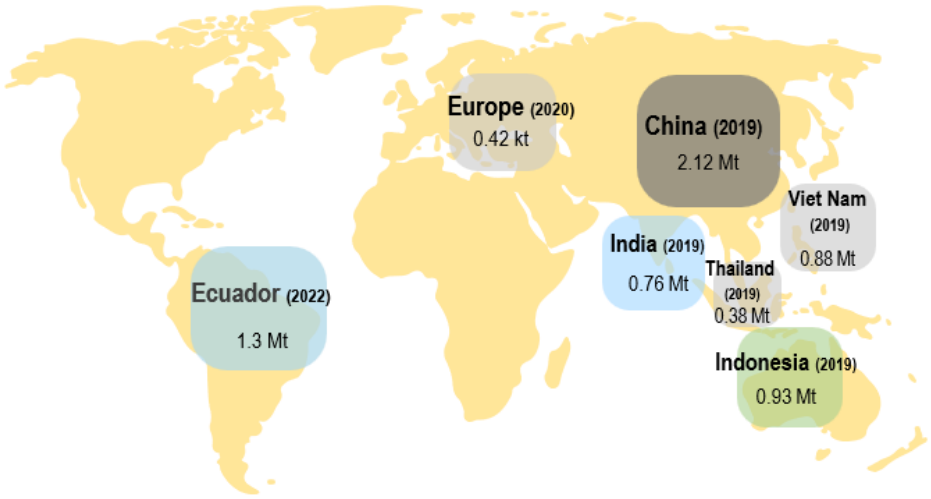

Figure 1.2 Aquaculture shrimp production by country.

1.1.3 Shrimp shell processing

Generally, shrimp are stored and exported in the frozen form, either with or without shells, based on market demand. Shrimps are processed in three major types, such as i) whole shrimp, ii) de-headed shrimp, and iii) peeled shrimp [15]. As shown in **Figure 3.3,** when shrimps arrive at the processing plants, they can be processed on the same day or could be stored in a frozen room if not processed immediately. Initially, shrimp are washed with regular water to eliminate

any visible impurities. These shrimps are sorted and graded following the requirements, with damaged and undesirable samples, classifying as low-grade products or garbage. Graded shrimp are subsequently washed with iced chlorinated water for hygiene purposes and then divided into three separate groups depending on demand. The first group is whole shrimp, which undergo additional processing with additive treatment to maintain their quality. The second group involves de-head shrimp, where shrimp are beheaded either manually or by using a machine. All de-headed shrimps are washed again to remove any unwanted debris and then soaked in an iced additive solution. The third group is called peeled shrimp, in which shrimp are initially immersed in cooled water for maturation up to 48 h or more. The maturation phase weakens the muscle-shell attachment to aid in the peeling process. After the peeling process, shrimp meat is gathered, rinsed, and subjected to an additive treatment. All shrimp are rewashed and graded again. All graded shrimp are weighed and packaged of 1 or 2 kg of shrimp per package before freezing. Frozen shrimp are thereafter located at the frozen storage facility at −20 °C until exportation (See **Figure 1.3**).

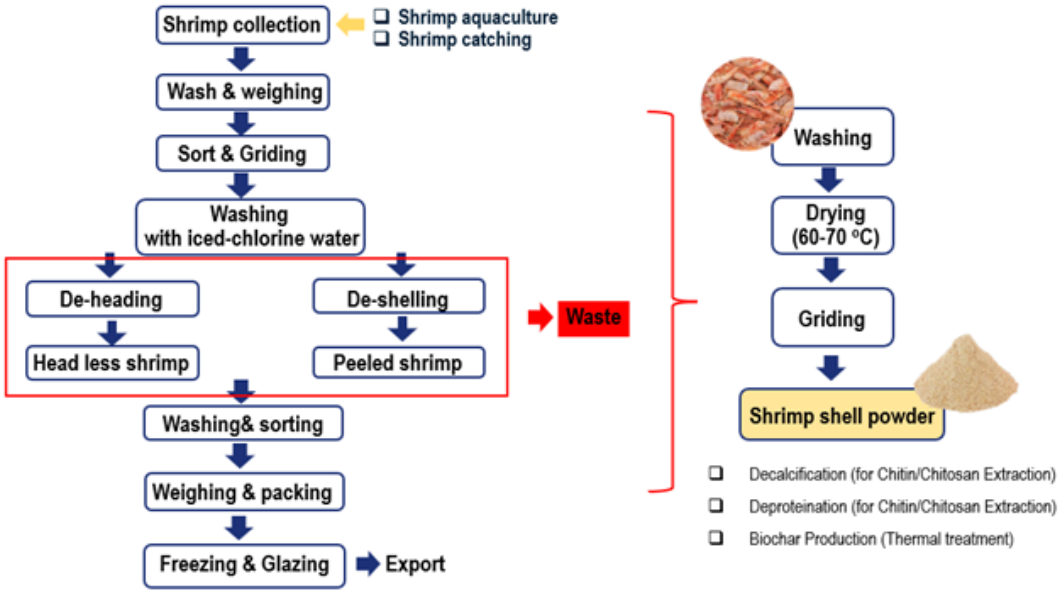

Figure 1.3 Schematic presentation of shrimp processing.

In the production of shrimp shell powder, fresh shrimp shells are thoroughly washed with purified water and/or neutralized by an acid-base treatment. The washed shrimp shells are then dried at 60-70°C for 24 h, after which they are ground into a fine powder and stored in a sealed container to preserve their quality [16, 17]. Shrimp shell powder can be transformed shrimp shell powder into valuable components, including chitin, chitosan, and biochar vis additional

processes such as chemical, biological (microbial) methods and thermal treatment [17] (See **Figure 1.3**). In the traditional chemical method, strong acids and bases are used to remove proteins and minerals from shrimp shells. HCL is employed for demineralization, while NaOH is used for deproteinization, yielding chitin. In the biological extraction process, proteolytic microorganisms or enzymes (such as Lactobacillus pentoses) are used for the demineralization and deproteinization of shrimp shells to extract chitin [16]. Chitosan can be obtained by removing the acetyl groups from chitin, a process known as deacetylation, using NaOH at high temperatures. In recent years, shrimp shell powder can be converted into biochar through thermal treatment, typically through pyrolysis. The shrimp shell-derived derived-biochar is very effective in environmental applications such as wastewater treatment, soil amendment, and others [17].

1.2 Environmental issues in shrimp aquaculture

1.2.1 Shrimp waste generation

During shrimp processing (sorting, beheading, peeling, and washing) processes (See **Figure 3.3**), nearly 35%–65% of waste is generated as shrimp head, viscera, and shell etc. [18]. Furthermore, the washing and cooking processes generate wastewater pollution, approximately 1 gallon of wastewater per ton of cooked shrimp. In focus, every year, 6–8 Mt of crab, shrimp, and lobster shells are discarded globally [19], and specifically, shrimp waste alone is estimated at around 3.8 Mt annually, generated during processing. About 1.5 Mt of shrimp shell waste are threw away in Southeast Asia alone. [20]. Due to the high cost of waste disposal, shrimp waste management is a global concern, particularly in developing nations. This serves environmental issue associated with land disposal, ocean dumping, or incineration. These shrimp wastes can cause odor production (gases, fumes, and dust) and rapid decomposition, resulting in environmental pollution affecting the economy, ecosystem and livelihood of the people [21]. Though a small amount of shrimp waste of shrimp shell waste can be utilized as animal feed, large amounts of this byproduct still available and pollute the environment [22]. Therefore, appropriate utilization of shrimp shell waste toward a zero-waste strategy can enhance the economic value of these by products and reduce environmental pollution.

1.2.2 Shrimp aquaculture wastewater

Shrimp aquaculture wastewater contains excessive nutrients, especially inorganic nitrogen (N) and phosphorus (P), leading to water quality deterioration and eutrophication [23].

The primary source of nutrient input is protein-rich feed and fertilizer as shrimp require protein for growth, accounting for 76–92% of N and 70–91% of P in the total inputs [24, 25]. Protein-rich feed is extensively utilized in intensive shrimp aquaculture to meet the high protein demands of shrimp, which are approximately two to three times higher than those of mammals. However, the digestibility of fish (snakehead, shrimp, crab, etc.) is limited due to its short gut [26]. Only 21–24% of N and 10–13% of P in this feed are incorporated into shrimp bodies, and the remaining amount is consequently retained in the pond water as waste [27, 28].

As shown in **Figure 1.4**, the sinks for N are the sediments (24%), and discharged water (27%). This leaves approximately 30% of the N unaccounted for which is assumed to be N lost to the atmosphere as Nitrogen gas (N_2) or ammonia (NH_3) [29, 30]. This volatilization of nitrogen results from the microbial decomposition processes in ponds particularly the bacterial conversion of nitrogen, primarily nitrate (NO_3^-), to N_2. Interestingly, aquaculture is recognized as a significant anthropogenic source of N_2O emission (3.83×10^{11} g in 2030), which is a potent greenhouse gas that contributes to ozone layer depletion and global climate change [31]. NH_3 is a significant atmospheric contaminant that affects environmental and public health, as well as climate change. On the other hand, 53.5% of P was assumed to be the eroded pond bottom, and effluent water accounted for 43.1% of P in the budget [30]. Excessive N and P residues in the pond may cause significant N and P contamination in natural water bodies via effluent discharge, which potentially causes eutrophication in water bodies receiving effluents from shrimp farms. Eutrophication disrupts ecological balance, dissolved oxygen level and potentially lead to significant mortality of aquatic organisms [32].

Additionally, poor shrimp farming practices, including the frequent use of antibiotics, pesticides, food additives, water and soil treatment agents, and hormones, are major contributors to the significant increase in pollution levels in aquaculture environments [33]. Large amounts of chemicals are used in shrimp ponds for controlling water quality problems, and the high risk of disease, and improve production. In both intensive and semi-intensive shrimp production, approximately 8.2 ton of chemicals and 41.7 tons of biological products are utilized alongside food additives. Food additives enhance the nutritional content of wastewater, and harmful compounds including antibiotics, disinfectants, and pesticides persist in the water as residues and remain in the environment for a very long period after being released [34].

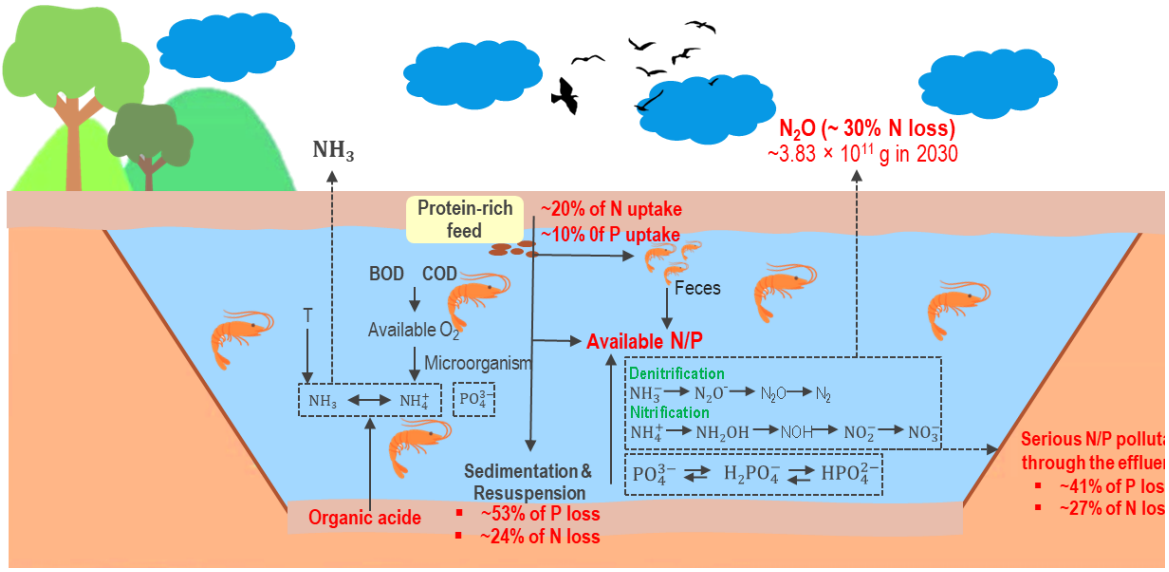

Figure 1.4 Nitrogen (N) and phosphorus (P) cycle in aquaculture shrimp pound.

As a result, shrimp pond wastewater contains N, such as nitrite (NO_2) and ammonia (NH_3); P, including phosphate (PO_4^{3-}); organic pollutants from chemical residues in feed, fertilizers, and antibiotics; and a high level of total organic matter. It also exhibits high biological oxygen demand (BOD) and chemical oxygen. [35] Overfeeding during the shrimp production stage, the use of fertilizers that increase eutrophication, and poor farm management practices are the major activities that might significantly enhance the pollutant load of the shrimp farmed wastewater. Shrimp aquaculture generates wastewater that poses significant environmental challenges due to its unsuitability for reuse, recycling, or discharge into natural water bodies.

1.3 Shrimp shell waste utilization

Shrimp shell wastes contained valuable compounds such as protein/peptides [36], chitin/chitosan [37], minerals [38] and vitamins [39], and others. The exact amounts of each composition vary depending on the sources and conditions of processing. Typically, shrimp shell waste contained valuable chitin (15–40%), protein (20–40%), and calcium carbonate ($CaCO_3$, 20–40%) [40, 41]. The shrimp waste composition also includes nutritious and beneficial compounds, such as essential and nonessential amino acids, minerals (calcium and phosphorus), and fat-soluble vitamins (vitamins A, D, and E). Moreover, several bioactive substances have been identified, including astaxanthin, protein hydrolysate (peptide), polyunsaturated fatty acids, and α-tocopherol [42].Many researchers have been developed value-added products derived from shrimp shell waste, including applications in the fields of

pharmaceutical [43], food [44], feed [45], environment [46], energy conversion [47], and other industrial approach.

Bioactive compounds derived from shrimp processing byproducts can be utilized in the food and feed industries. Chitosan, obtained from shrimp waste through chemical procedures, served as a food ingredient due to its antibacterial properties and non-toxic nature [48]. Astaxanthin, extracted from shrimp byproducts, was also utilized in poultry quality assessment [49]. Additionally, shrimp processing waste can boost the growth performance and immunity of aquaculture fish [50]. On the other hand, resent research has demonstrated the utilization of active chemicals derived from shrimp processing waste for metal and dye removal from wastewater, bioplastic production, and energy conservation, among other applications. Hydrothermal carbonization of shrimp waste produced hydrocar containing 39–40% carbon, 21–25% ash, and a calorific value of 18–23 MJ/kg. This carbon-rich shrimp shell waste utilized for energy conservation and carbon sequestration [51]. In another study, Thammahiwes et. al. (2018) [52] employed calcified shrimp shell powder in the fabrication of bioplastics. The use of shrimp shell powder shown notable enhancements in tensile, thermal, and morphological characteristics. Yuan et. al. (2020) [53] recently created biodegradable composite films by utilizing protein and chitosan derived from shrimp shell waste, which exhibited enhanced antioxidant characteristics and ultraviolet barrier efficacy.

1.3.1 Shrimp shell waste utilization for wastewater application

Recent studies have reported the application of active compounds derived from shrimp processing waste in the full removal of water pollutants, from inorganic (i.e., heavy metals) and organic pollutants (i.e., dyes) (see **Table 1.1**).

For example, shrimp shell powder was evaluated as a biopolymer for the removal of Fe, Al, Mn, Co, and Ni from mine-impacted water. Due to its high concentrations of chitin and $CaCO_3$, shrimp shell powder efficiently removed heavy metals from mine wastewater (rich in Fe, Mn, Hg, Zn, and Ni). The metal removal was accomplished through the physisorption, resulting in 90% removal overall [54, 55]. Shrimp shell waste serve as a cost-effective adsorbent for the removal of heavy metals from wastewater. Non-treated shrimp-shells were sun-dried and pulverized, and the produced powder was analyzed for its efficacy in textile color removal. Powdered shrimp shell (2.1 mg/L) effectively removed 90% of the color within 2 h. The mechanism exhibited the monolayer adsorption process enhanced by improved micro-porosity [56]. Shrimp shell waste was generated as hydrochar adsorbent via deproteinization and deacetylation procedures, subsequently followed by hydrothermal

carbonization (See **Figure 1.5**). The shrimp shell derived-hydrochar had an excellenct adsorption capacity of 755.1 mg/g for methyl orange dye at pH 4, attributable to its increased specific surface area and the presence of nitrogen-containing functional groups with elongated aliphatic chains [3].

Table 1.1 Shrimp shell waste in wastewater treatment applications.

Active compound	Application	Activity/ Function	Ref.
Chitin/ chitosan/ dried and ground shrimp shell	Dye/ heavy metal (Mn, Fe, Cu, etc.) removal from wastewater	Micro-porosity/ adsorption capacity and efficiency	[3, 54-58]
Calcified shrimp waste	Benzene degradation	Supporter for Pd NPs catalytic activity	[59]
Chitin nanofibrous-based membrane	Oil dispersion, Oil/water emulsion separation,	Antifouling activity/ emulsification activity	[60]

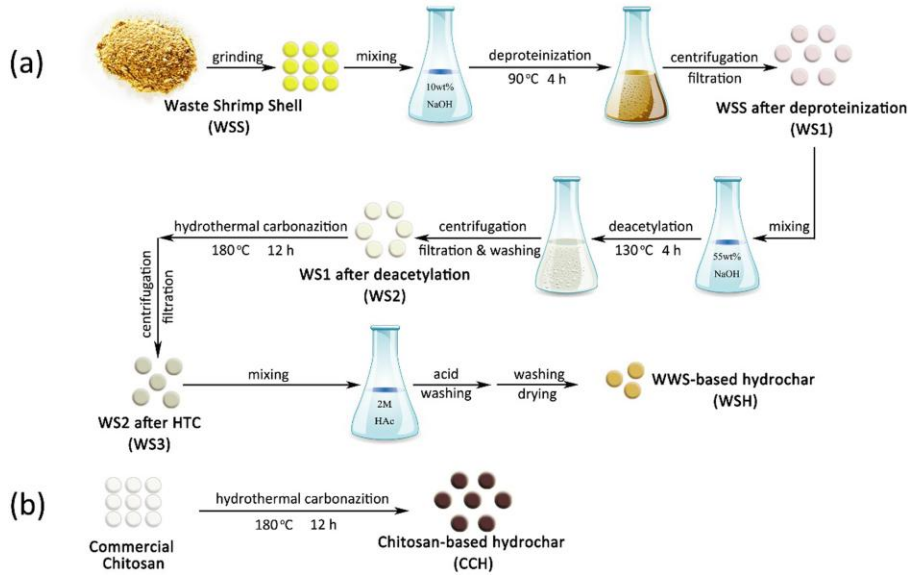

Figure 1.5 The preparation procedure of waste shrimp shell-based hydrochar [3].

1.4 Adsorbent-derived biochar for adsorption applications

These days, it is necessary to develop more sustainable approaches, cost-effective, and less complicate for wastewater treatment. Many researchers have investigated that adsorption

is preferable to other methods for removing pollutants from wastewater. Although a wide range of adsorbent materials are described in the previous studies, the use of waste materials is a creative disposal and waste removal strategy, referring to as a "waste to wealth". Pyrolysis is a preferred method to convert waste to biochar adsorbents with excellent physicochemical properties, including agricultural residues [61], egg shells [62], crab shells [63] and others. If biochar is used to adsorb nutrients such as PO_4^{3-}, PO_4^{3-} adsorbed-biochar can also be used as a soil amendment or fertilizer without generating secondary pollutants [62, 64].

1.4.1 Pyrolysis for biochar production

Biochar, a carbon-rich solid produced through the thermochemical conversion of biomass under limited or oxygen-free conditions at temperatures above 250 °C, has gained recognition as an effective material for addressing organic and inorganic environmental pollutants, particularly in water treatment applications. Though various thermochemical processes including include hydrothermal carbonization (HTC), pyrolysis, and gasification are employed to convert biomass into biochar and byproducts such as bio-oil and non-condensable gases, because of its effectiveness and adaptability for producing high-quality biochar [4, 5]. Pyrolysis is a thermochemical process that breaks down biomass in the absence of oxygen at temperatures between 300 and 900 °C, producing biochar, bio-oil, and gaseous byproducts [65]. The basic process of pyrolysis is illustrated in **Figure 1.6**.

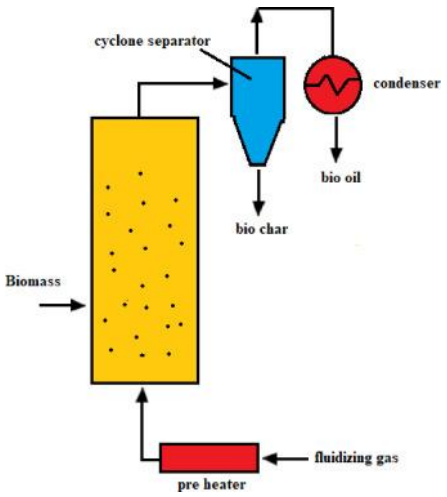

Figure 1.6 Lab-scale pyrolysis set-up [4].

Pyrolysis can be categorized into **slow (conventional)** and **fast processes**, depending on the operating conditions [4, 5].

❖ **Slow Pyrolysis**

Slow pyrolysis, a traditionally established method for charcoal the production, conduct over a wide temperature range (300–700 °C), with a long residence time (> 2 h), and low heating rates (5–7 °C/min). The process operates at atmospheric pressure, producing biochar, bio-oil, and gas in approximately similar amounts, regardless of the biomass type.

❖ **Fast Pyrolysis**

Fast pyrolysis is performed at higher temperatures (500–1000 °C) for short reaction durations, and high heating rates (≥200 °C/min). This technique primarily generates large amounts of bio-oil and non-condensable gases, whereas the yields of biochar are comparatively smaller than those obtained from slow pyrolysis. It is generally necessary to pre-dry the biomass to a moisture level of less than 10%.

1.4.2 Biochar for water pollutant adsorption

Recently, biochar production from biomass via pyrolysis has gained attention for its effectiveness in pollutants removal. Many previous studies have explored the effectiveness of different types of biochar in removing heavy metals from contaminated water. For example, pristine biochar, derived from Japanese oak wood and pyrolyzed at 500 °C, showed promising performance in sorbing arsenite (As) [66]. Burton et al. [67] found that biochar produced at 700 °C was more effective than that produced at 300 °C for As adsorption, particularly due to its higher specific surface area and increased surface aromaticity. The mechanisms of heavy metals adsorption by biochar from wastewater primarily involve complex formation, electrostatic interactions, and ion exchange (see **Figure 1.7**).

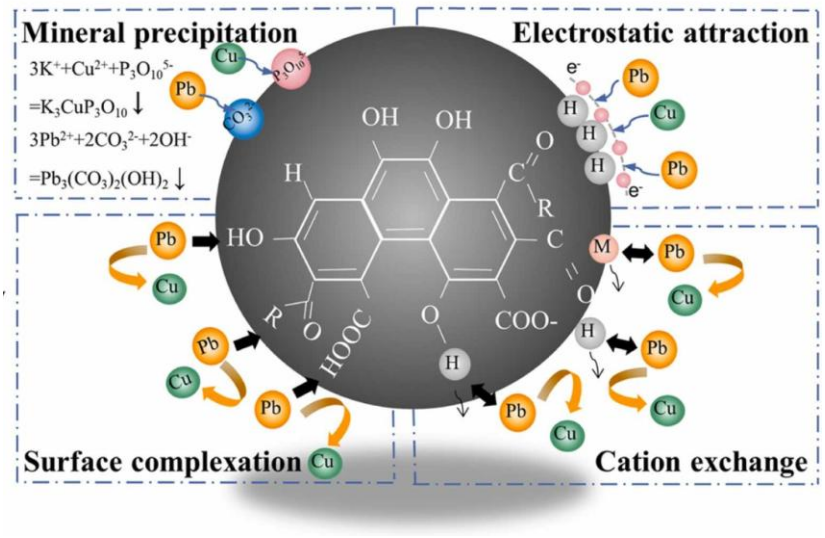

Figure 1.7 Heavy metal adsorption mechanisms of biochar. (modified form Liao et al. [6])

Biochar also has been investigated as an adsorbent for nutrient removal via adsorption. [5, 68]. However, biochar is primarily negatively charged, anions such as PO_4^{3-} and NO_3^- are typically repelled rather than adsorbed. Modifying biochar is essential to greatly improve its ability to adsorb nutrients by minimizing electrostatic repulsion or enhancing surface interactions. Without modification, no NO_3^- removal was observed for 12 biochars derived from three different biomass [69]. Similar findings were reported for biochars made from corn stover and oak wood pyrolyzed at 300-450 °C [70] and cacao shell and corn cob pyrolyzed at 300-350 °C [71]. On the other hand, biochar pyrolyzed from Lanthanum (La)-immersed oak sawdust significantly increased the NO_3^- adsorption capacity, from 2.02 mg/g (unmodified) to 22.58 mg/g. The enhancement in NO_3^- removal was due to an increase in the functional groups. The mechanism of nutrients adsorption was illustrated in **Figure 1.8**. Similarly, biochar derived from magnesium (Mg)-enriched tomato leaves demonstrated a high capacity for adsorbing PO_4^{3-}, with > 100 mg/g. The study also suggested that the PO_4^{3-}-loaded biochar could be utilized as a soil amendment or slow-release fertilizer due to its content of more than 10% P [72].

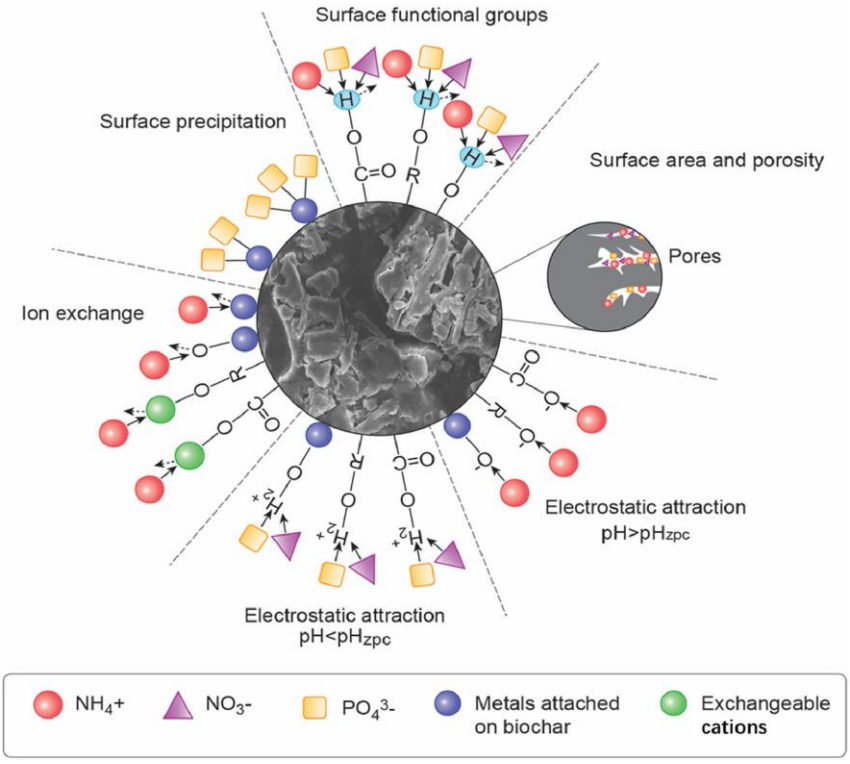

Figure 1.8 Nutrients adsorption mechanisms of biochar [5].

Table 1.2 Various types of biochar and their potential for the adsorption of heavy metals and nutrients.

Pollutants	Biochar Origin	Temperature	Adsorption capacity (mg/g)	Ref.
Pb^{2+}	Pine wood char	Fast pyrolysis 400–450 °C	4.13	[73]
	Buffalo Weed biochar	300, 500 and 700 °C	333.33 (700 °C)	[74]
Cd^{2+}	Cow manure biochar	400 and 600 °C	118.4	[75]
Cu^{2+}	Soybean straw char	400 °C	0.03	[76]
	Dairy manure biochar	200 °C and 350 °C	48.41 (350 °C)	[77]
Ni^{2+}	Taihu blue algae biochar	800 °C	2.2	[78]
	Chlorella sp. residue biochar	450 °C	27.45	[79]
NO_3^-	Bagasse	600 °C	28.21	[80]
	Al-modified poplar chips	550 °C	89.58	[81]
PO_4^{3-}	Crawfish char	800 °C	70.90	[14]
	Chitosan modified Mg impregnated corn straw biochar	400 °C	221.89	[16]
	Al-modified poplar chips	550 °C	57.49	[81]

1.5 Recent shrimp shell-derived biochar for adsorption applications

To date, various thermochemical conversion methods have been developed to produce and modify shrimp shell biochar. Slow pyrolysis is commonly preferred for shrimp waste recovery, due to its simpler setup, ease of control, and absence of additional instruments. Additionally, slow pyrolysis of shrimp shell wastes at higher temperatures (800 °C) and longer residence times (2 h) provides sufficient energy for more thorough carbonization into biochar. Biochar produced via slow pyrolysis exhibits a higher S_{BET} (449 m^2/g) compared to biochar from HTC (12.65 m^2/g) (see **Table 1.3**).

Table 1.3 Thermochemical conversion methods and properties of shrimp shell biochars.

Conversion methods	Operating parameters	Biochar properties	Ref.
Slow pyrolysis	800 °C, 5 °C/min, 2 h, N_2 gas Post-oxidation: HCl, Room temperature, 24 h	S_{BET}: 594 m^2/g Carbon content: 84 wt%	[82]
Slow pyrolysis	800 °C, 5 °C/min, 2 h, N_2 gas Post-oxidation: HCl, Room temperature, 24 h	S_{BET}: 449 m^2/g	[83]
Slow pyrolysis	800 °C; 5 °C/min; 2 h Pre-oxidation: 2 M NaOH; Room temperature; 24 h Chemical coating: Na_2SiO_3 and $MnSO_4$; 25 °C; 12 h	Carbon content: 10% S_{BET}:13 m^2/g V_{pore}: 0.0655 cm^3/g	[84]
HTC	180 °C, 12 h Pre-oxidation: 2.5 M NaOH (90 °C, 4 h); 50% NaOH (130 °C, 4 h) Post-oxidation: 1.5 M HCl; Room temperature; 1.5 h	C–H group: 16.77% Protonated amino group: 19% S_{BET}: 12.65 m^2/g	[85]

However, previous studies on the direct application of shrimp shells have been limited. Currently, most research has focused on synthesizing chitosan (the deacetylated form of chitin) from shrimp shells and modifying chitosan-based adsorbents. Chitosan can be readily available for crosslinking and modification with multivalent metals or clays to enhance its adsorption properties [86]. For example, a novel KOH deacetylated calcite-chitosan-based adsorbent (CCM) demonstrated the maximum adsorption capacity (q_{max}) of 21.56 mg/g for PO_4^{3-} removal at 22 °C after 120 min [87]. Besides, chitosan/Ca-organically modified montmorillonite beads (Cs/Ca-OMMT) achieved a q_{max} of 76.15 mg/g at 25°C after 120 minutes [88]. Various adsorption pathways have been explored, primarily adsorbing anionic contaminants through its N functional groups, particularly the $–NH_3^+$ groups. The limited number of studies on the direct use of shrimp shell biochar as an adsorbent, particularly when produced through pyrolysis, is summarized in **Table 1.4.**

Table 1.4 Application of shrimp shell biochars as adsorbent for removal of contaminants from wastewater.

Feedstock	Biochar synthesis method	Experimental conditions	Contaminants	Adsorption capacity (mg/g)	Removal mechanism	Ref.
Shrimp shell	Pyrolysis and chemical modification	Pyrolysis at 800 °C + magnetic modification + N-doped graphene oxide.	Cr^{4+}	350.4	Pore filling, electrostatic adsorption (ion-pair)	[89]
Shrimp shell	Pyrolysis	Pyrolysis at 800 °C for 2 h	Tris(2-chloroethyl) phosphate (-)	108 μmol/g	Pore filling, hydrogen bond interactions, π-H interactions	[90]
Shrimp shell	Pyrolysis and chemical modification	Pyrolysis at 350 °C for 2 h + HCL activation	Methylene blue (+)	575.0	Lewis acid-base interaction, π –π interaction, electrostatic interaction, van der Waals, and pyridinic-N	[91]
Shrimp shell	Pyrolysis and chemical modification	Pyrolysis at 500 °C for 2 h + H_3PO_4 activation	Methylene blue (+)	828	Electrostatic adsorption between the functional groups (PO_4^{3-}, COO^-, O^-)	[92]
Shrimp shell	HTC, Pyrolysis and KOH activation	Hydrothermal at 400 °C + KOH activation + Pyrolysis at 700–850 °C	Sulfamethazine (=) Chloramphenicol (=)	699.3	Physisorption, hydrogen bonds, π-π interactions, electrostatic interactions	[93]

Feedstock	Biochar synthesis method	Experimental conditions	Contaminants	Adsorption capacity (mg/g)	Removal mechanism	Ref.
Crayfish shell	Pyrolysis	Pyrolysis at 300, 500, and 700 °C for 2 h	Pb^{2+}	599.7 to 1166.4	Precipitation, ion exchange, complexation, C–π interaction	[94]
Crayfish shell	Pyrolysis and chemical modification	Pyrolysis at 600 °C + $ZnCl_2$ immersion for 24 h	Trichloroacetic acid (+)	17.8	Surface adsorption, electrostatic attraction	[95]
Crayfish shell	Pyrolysis	Pyrolysis at 800 ℃ for 1.5 h	Methyl violet (+)	1079	Pore filling, Electrostatic adsorption, precipitation, hydrogen bonds, van der Walls forces and π-π interaction.	[96]
Crayfish shell	Pyrolysis and chemical modification e	Pyrolysis at 600 ℃ for 2 h + $FeCl_2$ immersion for 3 h	Cr^{4+} PO_4^{3-}	25.68 3.82	Surface and intra-particle diffusion reactions	[97]
Crawfish waste	Slow pyrolysis	Pyrolysis at 200, 400, 600, and 800 °C for 2 h	PO_4^{3-}	70.9	Precipitation, ion exchange	[98]

Moreover, as shown in **Table 1.4**, scientific researches on shrimp shell-derived adsorbents have mainly focused on the removal of heavy metals and cationic pollutants while a limited number of articles have been published on the removal of anionic pollutants. As mention in the **Section 1.3**, shrimp shells are rich in $CaCO_3$. $CaCO_3$ derived from crustacean waste can remove contaminants through mechanisms such as precipitation, ion exchange, and electrostatic interactions [17]. $CaCO_3$ have been reported to facilitate PO_4^{3-} adsorption [87, 88] via ligand exchange as $CaPO_4^-$ [99]. Ca has a higher affinity for PO_4^{3-} adsorption compared to magnesium (Mg), lanthanum (La), aluminum (Al), and iron (Fe), respectively [100]. Moreover, the $CaCO_3$ could be converted into Ca-apatite-based adsorbents provides two different binding sites, including negatively charged P sites and positively charged Ca sites, on its surface, which offers a dual function for removing both anionic and cationic pollutants [101, 102]. Therefore, developing techniques to efficiently eliminate anionic pollutants would be greatly beneficial because of nutrient execs contaminants in shrimp aquaculture as mentioned in the **Section 1.1.2**.

There have been relatively few studies on crayfish (also called crawfish) compared to shrimp shells. Although both belong to the crustacean family, there are distinct differences in their chemical compositions that can affect adsorption performance. Specifically, crayfish and shrimp shells differ in their Ca content and other structural components, which may influence their effectiveness as adsorbents. The Ca content in these crawfish wastes is relatively lower, ranging from 7.0% to 41.2%, compared to the 80% found in the shrimp shells used in this work (See **Figure 1.9**).

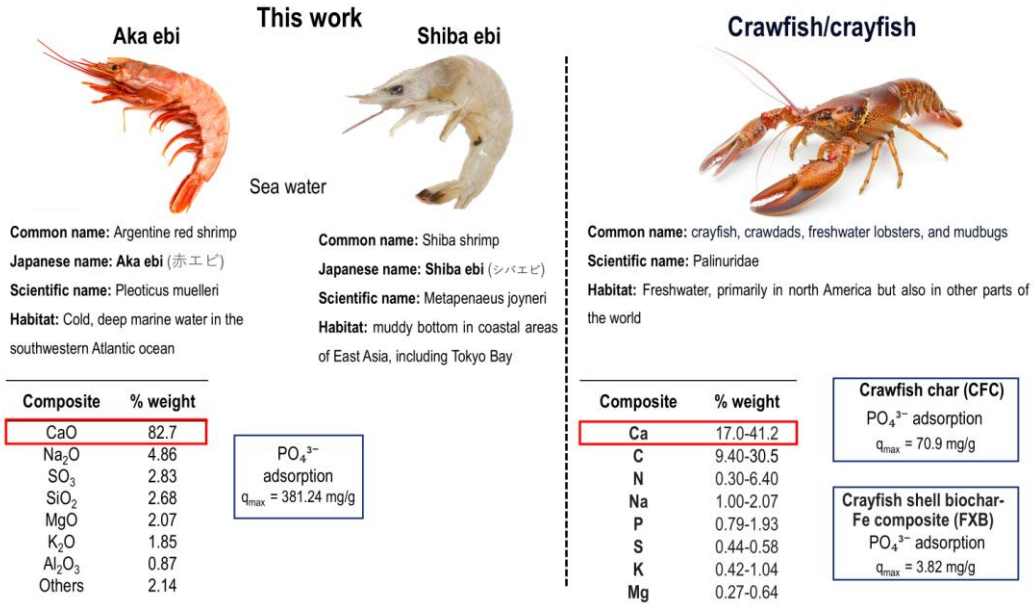

Figure 1.9 The chemical composition of crayfish/ crawfish and shrimp.

While shrimp aquaculture wastewater is known to contain mainly anionic pollutants, especially PO_4^{3-}, the application of shrimp shell-derived biochar for the removal of such pollutants has not been fully explored. More challenges still remain in improving the efficiency of shrimp shell based-adsorbents through the pyrolysis process for the removal of various types of anionic pollutants.

1.6 Research gap in shrimp shell derived-adsorbent in water pollutant removal

Shrimp aquaculture produces nutrient-rich wastewater and solid waste, posing major environmental challenges. Utilizing shrimp shell waste to remove water pollutants, particularly anionic nutrients like PO_4^{3-} from aquaculture wastewater, offers a sustainable solution, enabling waste reduction and nutrient recycling. The aquaculture can move towards a circular and sustainable system.

According to previous studies, shrimp shell-derived biochar produced through the pyrolysis process has demonstrated significant potential in removing various water pollutants, as highlighted in **Table 1.4**. However, the research gaps remain:

1. Research on using shrimp shell biochar as an adsorbent for removing anionic contaminants through pyrolysis is still limited, and additional studies are required to enhance its adsorption capacity and gain a deeper understanding of the mechanisms.

2. The use of shrimp shell waste in shrimp aquaculture presents a promising opportunity to develop a circular system by removing and recovering nutrients, especially PO_4^{3-}. While shrimp shells have been studied for their potential in nutrient removal, only two studies related to shrimp shell-derived biochars produced through pyrolysis for PO_4^{3-} adsorption were found, as shown in **Table 2.2**. Additional research is needed to evaluate the PO_4^{3-} removal and recovery performance in shrimp pond wastewater, contributing to a sustainable nutrient cycle in shrimp aquaculture.

Therefore, the main research gap is the limited research on shrimp shell-derived adsorbents for anion pollutant removal and nutrient recovery, particularly for PO_4^{3-}.

1.7 Objective of present work

The main objective of this study is to utilize shrimp shell waste for the production of shrimp shell-derived adsorbents (SSs) through the pyrolysis process, with the goal of removing anionic pollutants from shrimp aquaculture. In addition, the study aims to recover PO_4^{3-} to promote a circular system within shrimp aquaculture. To achieve this main objective, several

studies were carried out in the following way:

1. **Fabrication and Characterization of shrimp shell-derived adsorbents**: Shrimp shell waste was converted into SSs via the pyrolysis process at temperatures of 700°C and 800°C. A comparative analysis was also conducted with adsorbents produced through pyrolysis followed by alkali activation using (potassium hydroxide (KOH) and calcium hydroxide ($CaOH_2$)). The resulting adsorbents were characterized to assess their physical and chemical properties.

2. **Removal and recovery of phosphate**: The obtained SSs were studied for their performance as adsorbents in removing PO_4^{3-} from synthesized water, as a representative of real shrimp pond wastewater. Adsorption kinetics, isotherms, and thermodynamics were investigated to understand the adsorption process. The mechanism of adsorption was also examined. Finally, the PO_4^{3-} recovery ratio was calculated based on the obtained experimental data using the case study data from the southern part of Thailand.

3. **Removal of Methyl orange**: The obtained SSs were studied for their performance as adsorbents in removing Methyl Orange (MO), a model anionic pollutant from shrimp pond wastewater. Adsorption kinetics, isotherms, and thermodynamics were investigated to understand the adsorption process. The adsorption mechanism was also examined.

1.8 Thesis structure

This thesis consists of 5 chapters. Relationship between each chapter was illustrated in **Figure 1.10**. The details of each chapter are as follows:

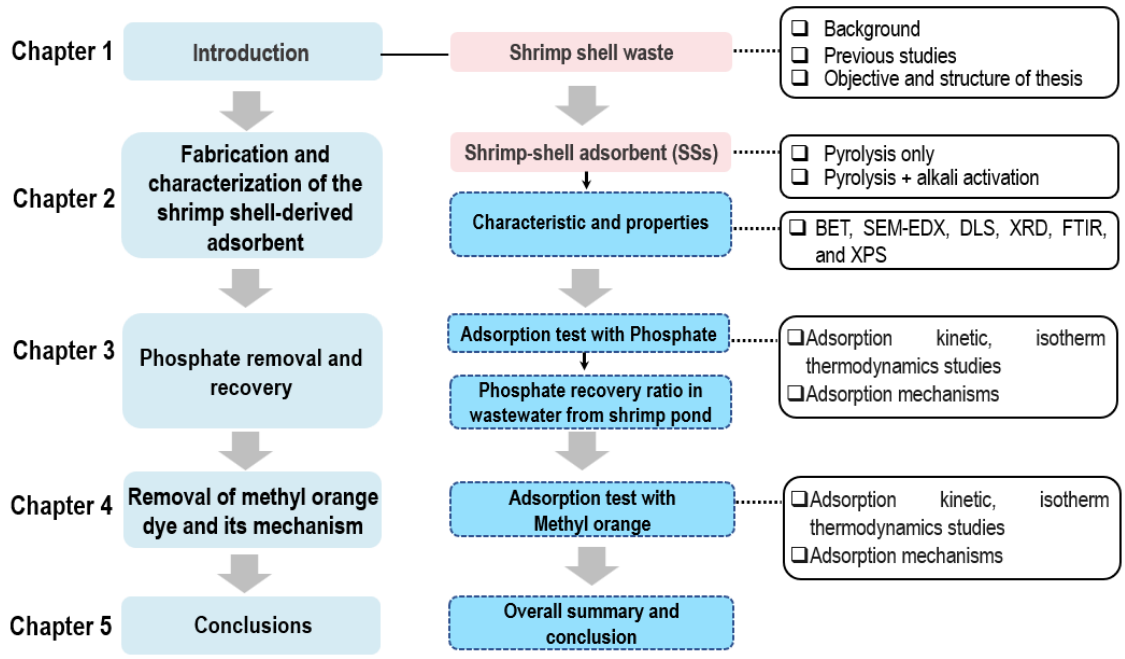

Figure 1.10 The thesis's content and its relationship

Chapter 1: Introduction

In this chapter, the background of this research was described. Firstly, the importance of shrimp cultivation and the processing of shrimp shell was present, highlighting the issues associated with the generation of shrimp shell waste and shrimp pond wastewater. Recent applications of shrimp shell waste, especially for wastewater treatment was stated. Additionally, current developments in shrimp shell waste utilization, including pyrolysis-based adsorbents, were emphasized in this study. Finally, the objectives and structure of this thesis were clarified in detail.

Chapter 2: Fabrication and characterization of the shrimp shell-derived adsorbent

In this chapter, the fabrication of the shrimp shell derived-adsorbent was explained. The shrimp shell derived-adsorbent was called SSs. The SSs was fabricated using different pyrolysis temperatures (700 ℃ and 800℃) and alkali activation (KOH and $CaOH_2$), labeled SSsN (pyrolysis only at 700 ℃), SSsH (pyrolysis only at 800 ℃), SSsCA ($CaOH_2$ activation + pyrolysis at 700 ℃), and SSsK (KOH activation + pyrolysis at 700 ℃), respectively. Each SSs was investigated for morphological, physical, and chemical properties. The properties regarding their different fabrication and composition were discussed. Results indicated that the modified shrimp shell developed a rougher and more porous surface compared to the raw shrimp shell, and SSsH had the highest specific surface area (S_{BET}) and total pore volume (V_{pore}). Calcium oxide (CaO) is the main component in the raw shrimp shell sample, suggesting calcium-rich material. Calcium carbonate ($CaCO_3$), $Ca(OH)_2$, hydroxylellestadite (HDL; $(Ca_{10}(SiO_4)_3(SO_4)_3(OH, F, Cl)_2$), potassium sodium calcium chloride carbonate hydrate (KSC: $K_6NaCa_2(CO_3)_5Cl(H_2O)_6$) were observed the SSs samples. The formation of new chemical structures offered potential for anionic pollutant adsorption.

Chapter 3: Phosphate Removal and Recovery

This chapter aims to examine the performance of SSs in removing PO_4^{3-} from aqueous solutions. All SSs are capable to absorb PO_4^{3-}, with SSsCA exhibited demonstrating the best performance for PO_4^{3-} removal. Adsorption kinetics, isotherms, and thermodynamics indicated that the process involved endothermic chemical adsorption. The removal mechanism revealed that PO_4^{3-} removal primarily occurs via chemical precipitation with Ca^{2+}, facilitating its recovery as various calcium-phosphate (Ca-P) groups. Ca^{2+} originates from HDL, $CaCO_3$, and $Ca(OH)_2$. Finally, the PO_4^{3-} recovery ratio was calculated through a case study utilizing from

a shrimp pond in the southern Thailand, resulting in a recovery ratio of 69.54%. This chapter provided an alternative for handling shrimp shell waste and suggested a promising approach for PO_4^{3-} recovery, thereby contributing to a circular system in shrimp aquaculture.

Chapter 4: Removal of methyl orange dye and its mechanism

This chapter aims to examine the performance of SSs in removing MO dye as a model anionic pollutant from aqueous solutions. The removal performance was investigated under the effect of contact time and initial concentration. Adsorption kinetics, isotherms, and thermodynamics indicated that the process involved endothermic, and primarily controlled by chemisorption, along with physisorption. This study also found excellent MO adsorption onto SSs, in particular SSsCA and SSsN. Moreover, the presence of HDL enabled SSs to demonstrate a large adsorption capacity by releasing Ca^{2+} and expose silanol-like surface properties for adsorbing anionic MO. Significant results showed that the initial MO concentration influenced the adsorption performance and mechanisms of SSs, which involved both reversible and irreversible adsorption processes. The adsorption was reversible at low MO concentration (≤ 100 mg/L). In contrast, it became irreversible at high concentration (>100 mg/L). These MO polymers interacted with SSs through both Si-N linkages and SO_3^-–Ca^{2+} complexes. This chapter highlighted the significance of initial pollutant concentration dependency and evaluated the potential of utilizing SSs for the removal of other anionic pollutants from shrimp aquaculture wastewater.

Chapter 5: Conclusions and recommendations

The important findings from each chapter are summarized in this chapter. In addition, this chapter provided implementation of this research and recommendations for future work.

Chapter 2

Fabrication and characterization of the shrimp shell derived-adsorbent

2.1 Background

The main goal of this thesis is to efficiently employ shrimp shell-derived adsorbents (SSs) for the removal of anionic pollutants from shrimp pond wastewater. The raw shrimp shell waste was transformed into biochar adsorbents to address the serious issue of overcoming large amounts of shrimp shell waste and nutrient rich-wastewater produced by shrimp farming. Transforming shrimp shells into adsorbents offers a sustainable waste management solution and fosters a circular system in shrimp aquaculture.

The conversion of shrimp shell waste into adsorbents through pyrolysis significantly enhances the specific surface area, porosity, and abundance of oxygen-containing functional groups, enabling effective adsorption of a wide range of pollutants [103, 104]. Shrimp shell waste, rich in $CaCO_3$, processes through pyrolysis at high temperatures to transform $CaCO_3$ into a more active form including CaO and Ca-apatite. Calcium (Ca) plays a crucial role in anionic pollutant adsorption, especially phosphate (PO_4^{3-})[100]. Raising the temperature facilitates the release of active Ca^{2+} [105], and incorporating calcium hydroxide ($Ca(OH)_2$) further enhances Ca^{2+} availability. Potassium hydroxide (KOH) activation improves surface properties, as demonstrated in previous studies [106, 107]. Interestingly, this study also found the formation of hydroxylellestadite (HDL), which belongs to the apatite family. HDL has unembedded calcium silicate hydrate (CSH), facilitating the release of release Ca^{2+} and the exposure of silanol-like surface in the pH range of 2–11, which is crucial for the adsorption of anionic pollutants [108, 109] [110].

In this chapter, shrimp shell derived adsorbent (SSs) were fabricated through a pyrolysis process. Alkali modifications using potassium hydroxide (KOH) and calcium hydroxide ($CaOH_2$) were tested and compared with non-alkali-activated pyrolysis samples. This study examined the influence of activation temperature and alkali activator type on the characteristics of SSs. The synthesized samples were characterized to assess their physicochemical properties, offering insights into the impact of synthesis conditions on the structure and effectiveness of SSs for prospective adsorption applications.

2.2 Fabrication of the shrimp shell-derived adsorbent

2.2.1 Materials

v World Co., Ltd., Japan. Methyl orange (MO) dye, potassium hydroxide (KOH), and calcium hydroxide ($Ca(OH)_2$) used in this study were purchased from Wako Pure Chemical Industries, Ltd., Japan. Deionized water (DI) was purified by a Mili-Q Advantage system 119 (Millipore, Billerica).

The chemical composition of the raw shrimp shell was investigated by X-ray fluorescence spectrometer (XRF; S2Langer, Bruker AXS) and shown in **Table 2.1**. The table shows that the raw sample contain 82.7% of calcium (Ca), indicating ca-rich material.

Table 2.1 Chemical composition of raw shrimp shell by XRF analysis.

Composite	CaO	Na_2O	SO_3	SiO_2	MgO	K_2O	Al_2O_3	Others
% composition	82.7	4.86	2.83	2.68	2.07	1.85	0.87	2.14

2.2.1 Fabrication method

Two modification methods were used: pyrolysis of shrimp shell alone and pyrolysis of shrimp shell with alkali activation (KOH and $Ca(OH)_2$). For the pyrolysis alone, the raw shrimp shell powder was pyrolyzed at 700 and 800 ℃ for 1 h at a heating rate of 15 ℃/min. The reactor was purged with nitrogen gas (N_2) for 15 minutes to ensure the absence of oxygen before pyrolysis. This chapter also compared the effects of pyrolysis at different temperatures from 400°C to 700°C, with preliminary methyl orange (MO) adsorption tests. Pyrolysis at 700°C showed significant improvement over 600°C, as detailed in **Appendix A.1**. Therefore, this chapter focused on temperatures starting from 700°C.

The alkali activation of shrimp shell with KOH or $Ca(OH)_2$ was also conducted. The alkali activation with pyrolysis helps enhance surface properties such as surface area and aromatic functional groups [106, 107]. KOH or $Ca(OH)_2$ solutions with 5 w/v% concentration were mixed with shrimp shells at a mass ratio of 0.5:1 and then heated at 150 ℃ for 2 h. The dense suspension was also pyrolyzed under the same conditions as mentioned above. The obtained solid products were ground to pass through a 100-mesh (150 μm) and finally named as **Shrimp shell-derived adsorbent: SSs**, including **SSsN** (pyrolysis only at 700 ℃), **SSsH** (pyrolysis only at 800 ℃), **SSsCA** ($Ca(OH)_2$ activation and pyrolysis at 700 ℃), and **SSsK**

(KOH activation and pyrolysis at 800 °C). The appearance of all sample was exhibited in **Figure 2.1**.

Noted that the alkali activation ratio used in this experiment was adapted from the methodologies described by Pap et at. [111], which were employed in the preparation of adsorbent biochar from mussel and oyster shells, demonstrating high efficiency for PO_4^{3-} as discussed prior the experiment.

2.3 Characterization of physical and chemical properties

2.3.1 Surface morphology and porosity

Each SSs was pulverized and examined for their porosity using scanning electron microscopy (SEM; JSM-6610LA, Japan). SEM magnification of x1000 with an acceleration voltage of 15 kV was selected to observe each sample. The samples were initially coated with platinum (Pt) for 1 min before high-resolution imaging. The elemental distribution on the surface of SSs was measured by LYRA 3 Dual Beam (Tescan) equipped energy dispersive X-ray spectrometry (EDS, Oxford Instruments). The zeta potential was evaluated by dynamic light scattering (DLS) (Horiba sz-100, Japan). The samples were dispersed in DI water and measured within a pH range of 2–10. The duration time was set to 30 s and the number of scans was set to 3. The specific surface area (S_{BET}) and total pore volume (V_{pore}) were determined by the BET method using N_2 adsorption (BET; Belsorp-mini II, MicrotracBEL, Japan). The samples were pretreated at 150 °C for 6 h before measurement.

As shown in **Figure 2.1**, the morphological surface texture of the raw shrimp shell was flat and no porosity, while the pyrolyzed shrimp shells (with or without $Ca(OH)_2$ activation) showed rougher surfaces (see **Figure 2.1a**). As the pyrolysis temperature increased to 800 °C, the surface of SSsH exhibited more cracks compared to SSsN (pyrolysis at 700 °C) (see **Figure 2.1c**). Meanwhile, more small protrusions were observed on the surface of SSsCA and SSsK (see **Fig. Figure 2.1d and e**). The EDS results show that the elemental distribution of Ca is consistent throughout the surface, regardless of the modification method used (See **Figure 2.2**)

The surface area and pore structure of the SSs were studied via nitrogen adsorption-desorption isotherm, classified as a mesoporous adsorbent (type IV in the IUPAC classification) (see **Fig. 2.3**). As listed in **Table 2.1**, the S_{BET} and V_{pore} of SSs increased significantly compared to the raw shrimp shell. The S_{BET} of SSsN, SSsH, SSsCA, and SSsK are 38.23, 96.69, 17.21, and 15.54 m^2/g, respectively. The V_{pore} followed a similar trend to those of S_{BET}. This increase results from devolatilization and gas release during pyrolysis [112].

SSsH had the highest S_{BET} and V_{pore} due to the decomposition of $CaCO_3$ into CaO and CO_2 during the pyrolysis process at 800 °C [105] (see **Fig. 2.1c**). The generation and liberating of CO_2 can develop the surface area and porous structure of the SSsH [62, 113]. In contrast, the S_{BET} of SSsCA decreased slightly due to pore coverage and blockage by loaded Ca^{2+} [114, 115], consistent with SEM images showing small particles on the SSsCA surface (see **Fig. 2.1d**). Similarly, KOH activation (SSsK) also destroyed porosity structure and adsorption sites [116](see Fig. 1e). Interestingly, a significant reduction of the total pore volume was observed for SSsK (0.032 cm^3/g) (See **Table 2.2**). The influence of KOH activation on pore structure, especially at high temperatures, has been thoroughly investigated. Though previous studies demonstrate that KOH activation can substantially enhance the development of pores in carbon materials, excessive amount may result in structural deformation and pore collapse [117]. KOH activation, exhibited a greater impact on pore collapse and tightening up the pore structure, compared to $Ca(OH)_2$ [118]. It was suggested that the pore formation and structural deformation phenomena were due to ionic valency. Monovalent ions like K^+ are smaller than divalent ions like Ca^{2+}, and carries a lowered charge, which allows them to move more freely and distribute more throughout the material. They can therefore tighten and collapse the structure with greater effect than Ca^{2+}.

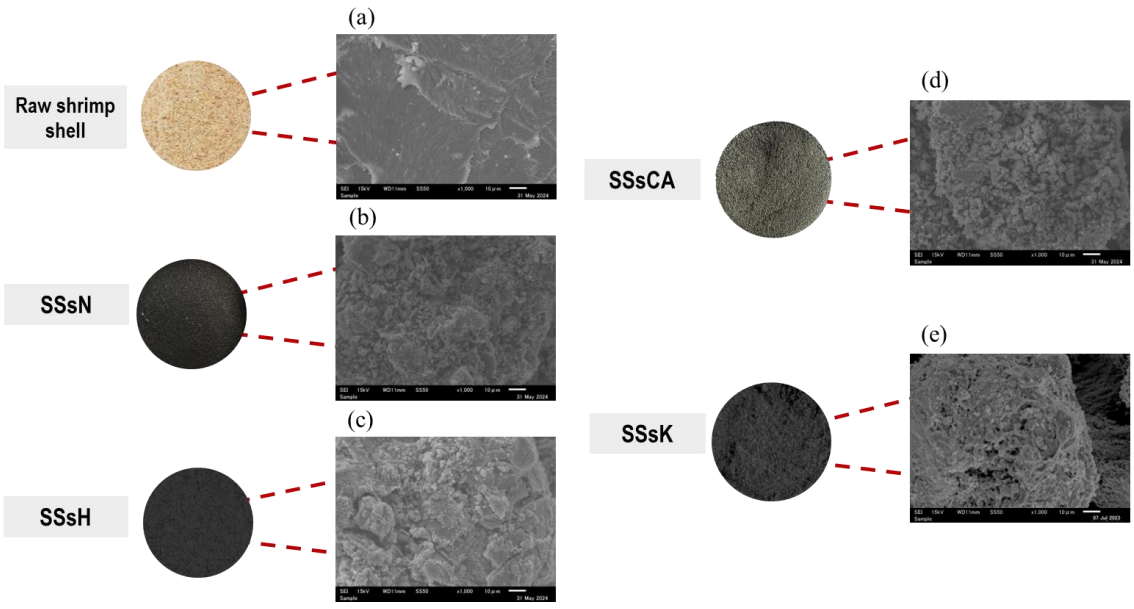

Figure 2.1. Appearance and SEM images of SSs (a) Raw shrimp shell, (b) SSsN (pyrolysis only at 700 °C), (c) SSsH (pyrolysis only at 800 °C), (d) SSsCA ($Ca(OH)_2$ activation and pyrolysis at 700 °C), and (e) SSsK (KOH activation and pyrolysis at 800 °C).

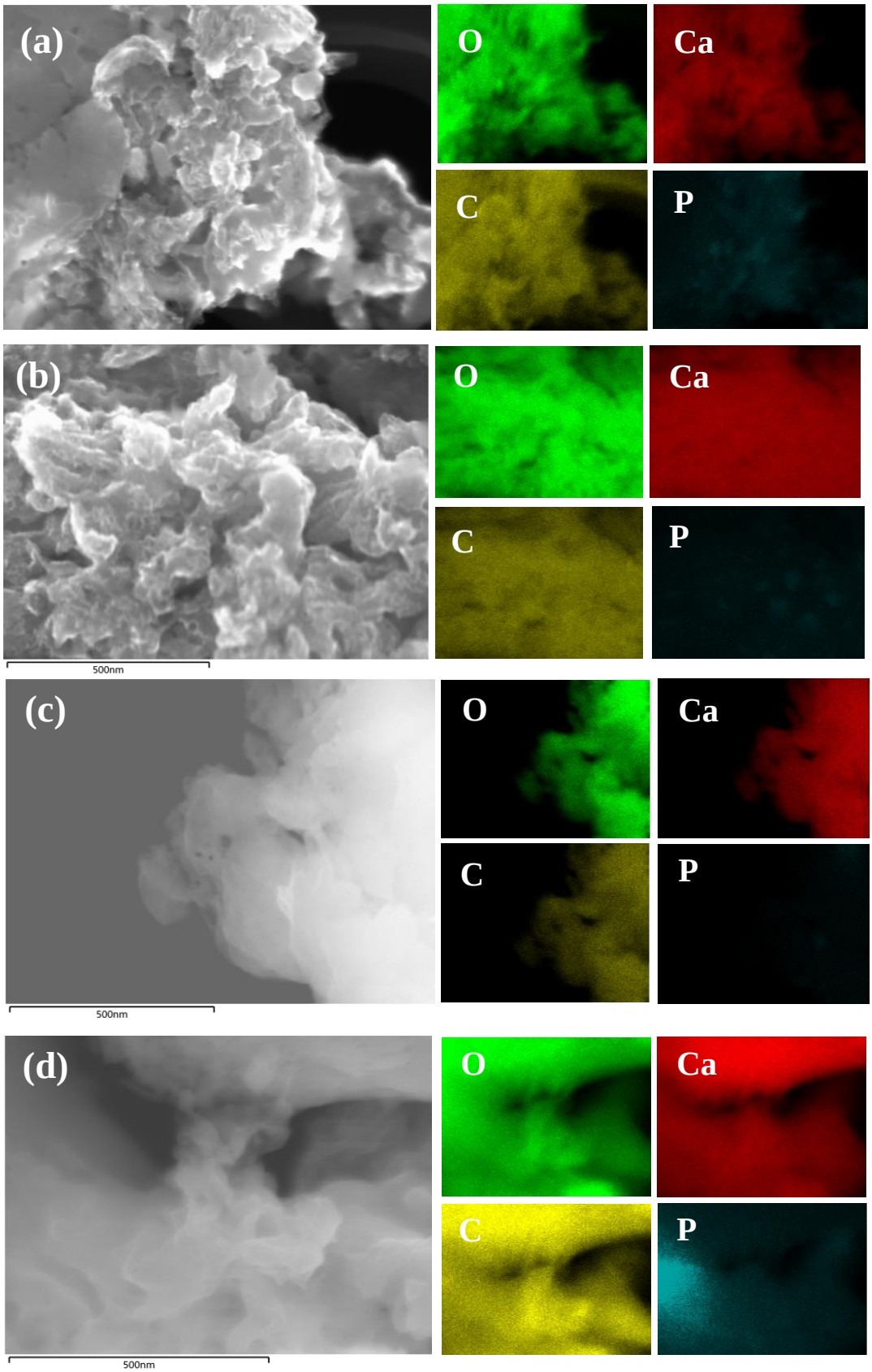

Figure 2.2 EDS mapping of the SSs under different modification methods. (a) SSsN, (b) SSsH, (c) SSsCA, and (d) SSsK.

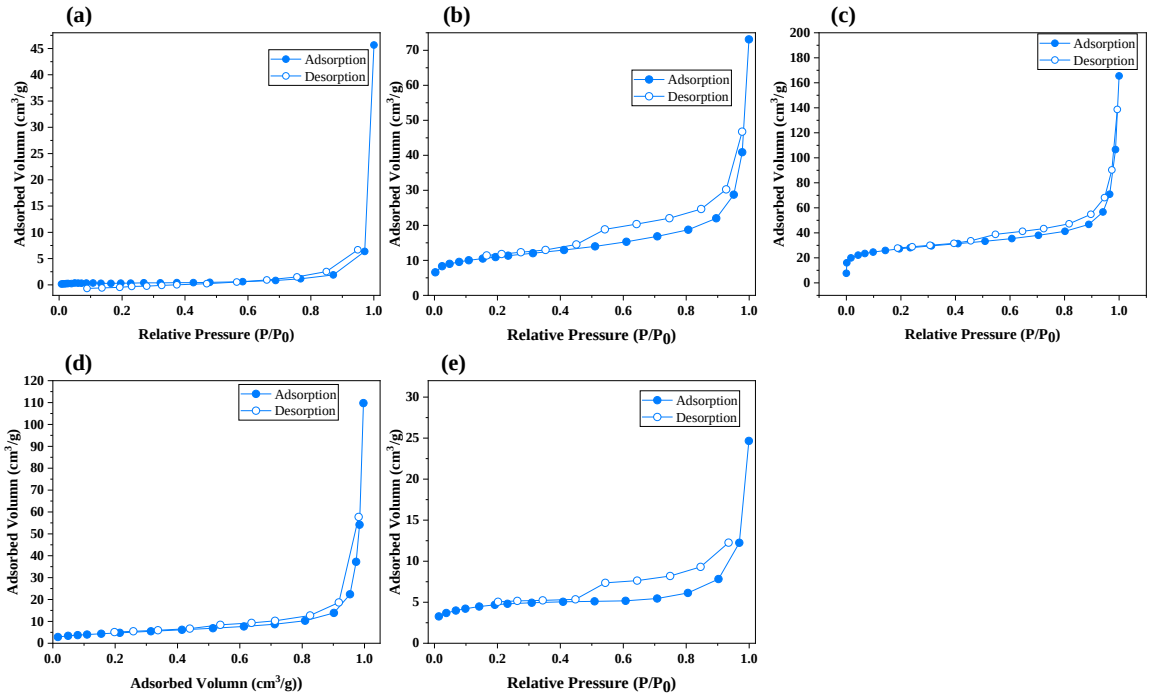

Figure 2.3 N_2 adsorption–desorption isotherms (BET) diagram for SSs at different modification methods: (a) Raw shrimp shells; (b) SSsN; (c) SSsH; (d) SSsCA, and (e) SSsK.

Table 2.2 Specific surface area, external surface area, and total pore volume of the raw shrimp shell and SSs.

Sample	S_{BET} (m^2/g)	External surface area (m^2/g)	V_{pore} (cm^3/g)
Raw shrimp shell	3.762	-	-
SSsN	38.23	17.62	0.091
SSsH	96.69	64.47	0.181
SSsCA	17.21	13.29	0.098
SSsK	15.54	6.45	0.032

The point of zero charge (P_{ZC}) for all SSs was pH 2.5-3, indicating a negatively charged surface when the solution pH exceeded at pH > 3 (see **Fig. 2.4**). Since the pH of the solution in this study was 8 in PO_4^{3-} adsorption experiment and 9 in MO adsorption experiment. Therefore, both the SSs surface and these pollutants carry negative charges, causing electrostatic repulsion that hinders adsorption.

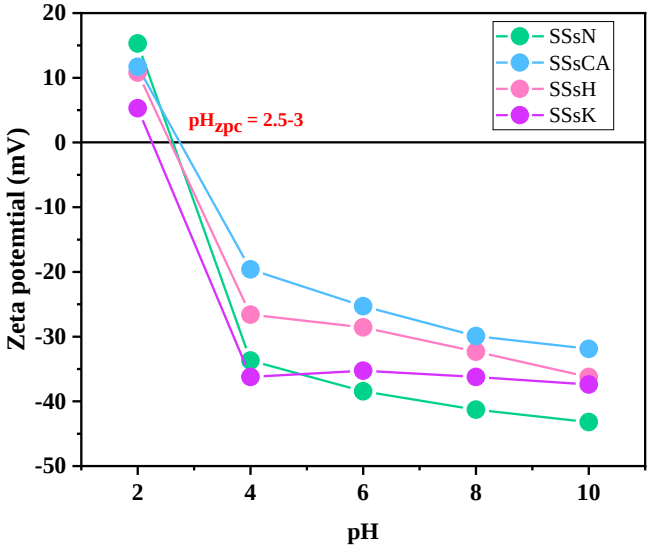

Figure 2.4 Zeta potential of SSs with different modification conditions.

2.3.2 Surface chemistry

The crystalline phases were analyzed by X-ray diffraction (XRD; Rigaku XRD-Ultima IV, Japan) at 40 kV and 40 mA equipped with Cu Kα radiation. The data was collected from 5 to 70° (2θ) at a scan rate of 0.01°. The functional groups on the surface were characterized by Fourier Transform Infrared Spectroscopy (FTIR; 4600, JASCO, Japan) at a spectral resolution of 4 cm^{-1} and 32 scans within the scanning region (4000–400 cm^{-1}). The chemical structures were analyzed by X-ray photoelectron spectroscopy (XPS) using two different sources: the ULVAC-PHI Model 5500 (Japan) and the Ulvac PHI Quantera SXM (Japan), both equipped with a monoenergetic Al Kα source (1487 eV). The binding energy scale of the spectra was referenced to the C 1s peak at 284.60 eV. The chemical structures were also analyzed by X-ray photoelectron spectroscopy (XPS; Model-5500, Ulvac-PHI, lnc., Japan) with a monoenergetic Al Kα source (1487 eV) operating at 25 W. High-resolution spectra were recorded at 46.95 eV pass energy. The binding energy scale of the spectra was referenced to the C 1s peak at 284.60 eV.

The XRD patterns of raw and modified shrimp shells are indicated in **Figure 2.5**. Raw shrimp shell consisted mainly of $CaCO_3$ peak. In the pyrolyzed shrimp shells at 700°C (with or without $Ca(OH)_2$ activation), peaks for $CaCO_3$ and HDL ($Ca_{10}(SiO_4)_3(SO_4)_3(OH, F, Cl)_2$) were identified. Whereas, these $CaCO_3$ peaks disappeared in the SSsH, attributing to the decomposition of $CaCO_3$ into CaO and CO_2 at 800 °C [119, 120]. The generated CaO might

be converted into $Ca(OH)_2$ because of the reaction between CaO and nascent water molecules during pyrolysis [120]. Therefore, the new peaks belonging to $Ca(OH)_2$ appeared, together with HDL. HDL, a member of the apatite group forming at 700 °C [121], can be observed in SSsN, SSsH and SSsCA, except for SSsK. In contrat SSsK showed strong peaks of potassium sodium calcium chloride carbonate hydrate (KSC: $K_6NaCa_2(CO_3)_5Cl(H_2O)_6$) instead of HDL (see **Figure 2.5**).

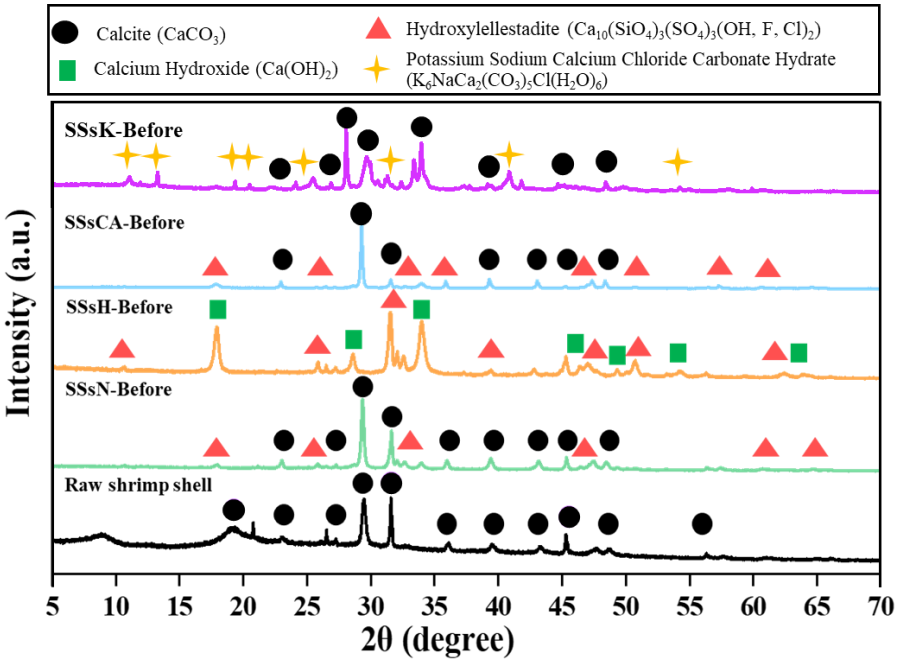

Figure 2.5 XRD pattern of SSs with different modification conditions.

The FTIR results confirmed the XRD findings (see **Figure 2.6**). The functional groups of SSs were significantly changed after the pyrolysis. The pyrolysis caused the organic volatilization, resulting in the disappearance of stretching vibrations of OH at 3300-3500 cm^{-1} [122], C-H, CH_2, and CH_3 at 2960-2880 cm^{-1} regions [123], and C=O (amide-I) at 1631 cm^{-1} and 1531 cm^{-1} in $-NH_2$ (amide II) [124]. After pyrolysis, all SSs (SSsN, SSsH, and SSsCA) showed the characteristic bands of the single-layered silicate structure belonging to HDL. The intense bands at 1085 and 1033 cm^{-1} were corresponded to Si–O from SiO_4 tetrahedra [125, 126], and the bands at 875 cm^{-1} and 713 cm^{-1} indicated the bridging oxygen stretching vibration (Si–O–Si) [127, 128]. The low-frequency bending band of O-P-O at 603 and 570 cm^{-1} was consistent with the previous studies, which reported O-P-O bands in the apatite-ellestadite sites [129, 130]. While the presence of $CaCO_3$ was detected in SSsN, SSsCA, and SSsK at the intense peak of 1400 cm^{-1} (CO_3^{2-}) [122, 131], the broad CO_3^{2-} peak collapsed (lower peak intensity) in SSsH, and a new sharp peak at 3643 cm^{-1} appeared, indicating

$Ca(OH)_2$ formation [132, 133]. Moreover, the low-frequency bands at 873 cm^{-1} and 855 cm^{-1} also represented CO_3^{2-} of $CaCO_3$, but with lower intensities [134].

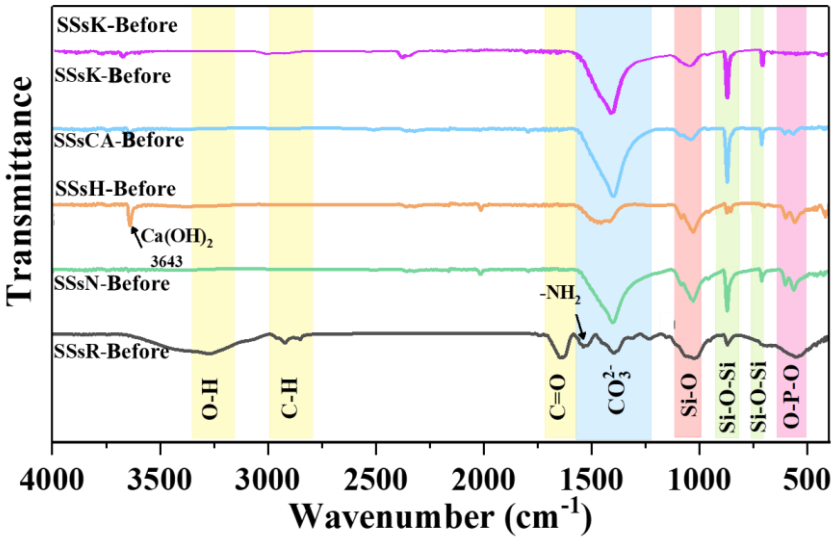

Figure 2.6 FT-IR spectra of SSs with different modification conditions.

XPS scan spectrums of raw shrimp shells and all SSs are presented in **Figure 2.7**. The XPS spectra of Ca 2p from raw and modified shrimp shells showed peaks at 346.60, 346.81, and 350.37 eV for Ca-O in $CaCO_3$ in samples pyrolyzed at 700 °C (SSsN and SSsCA) (see **Figure 2.7a**) [135, 136]. The binding energy of 350.20 eV also indicated Ca^{2+} in dicalcium phosphate dihydrate ($CaHPO_4 \cdot 2H_2O$) of HDL [137]. Similarly, the XPS spectra of O 1s contain two separated peaks at 531.06 and 531.70 eV, suggesting PO_4^{3-} in the apatite group (that might be HDL in this work) and oxygen in CO_3^{2-}[138, 139], respectively (see **Figure 2.7b**). These peaks did not show significant changes between SSs treated with and without $Ca(OH)_2$ (SSsN and SSsCA). Interestingly, in SSsCA, the peak of C 1s at 284.38 eV representing aromatic C-C/C=C bonds appeared, which is beneficial for PO_4^{3-} adsorption (see **Figure 2.7c**). On the contrary, in SSsH, the major peaks of Ca 2p at 346.94 eV and 350.44 eV corresponded to Ca-O bond with oxygen in OH^- group [140] (see **Figure 2.7a**). The peaks of O 1s at 531.20 eV were also assigned to the surface adsorbed oxygen species (O_{ads}), relating to Ca-OH from chemisorbed water [105] (see **Figure 2.7b**). Besides, only SSsK showed the peaks of K 2p3/2 and K 2p1/2 at 292.86 and 295.93 eV, indicating the presence of potassium carbonate (K_2CO_3) and oxide (K_2O), respectively [141] (See **Figure 2.7d**). It is noted that the SSsK in **Figure 2.7d** cannot be included in the same graph as other SSs samples (**Figure 2.7c**) due to differences in the XPS series equipment used for analysis.

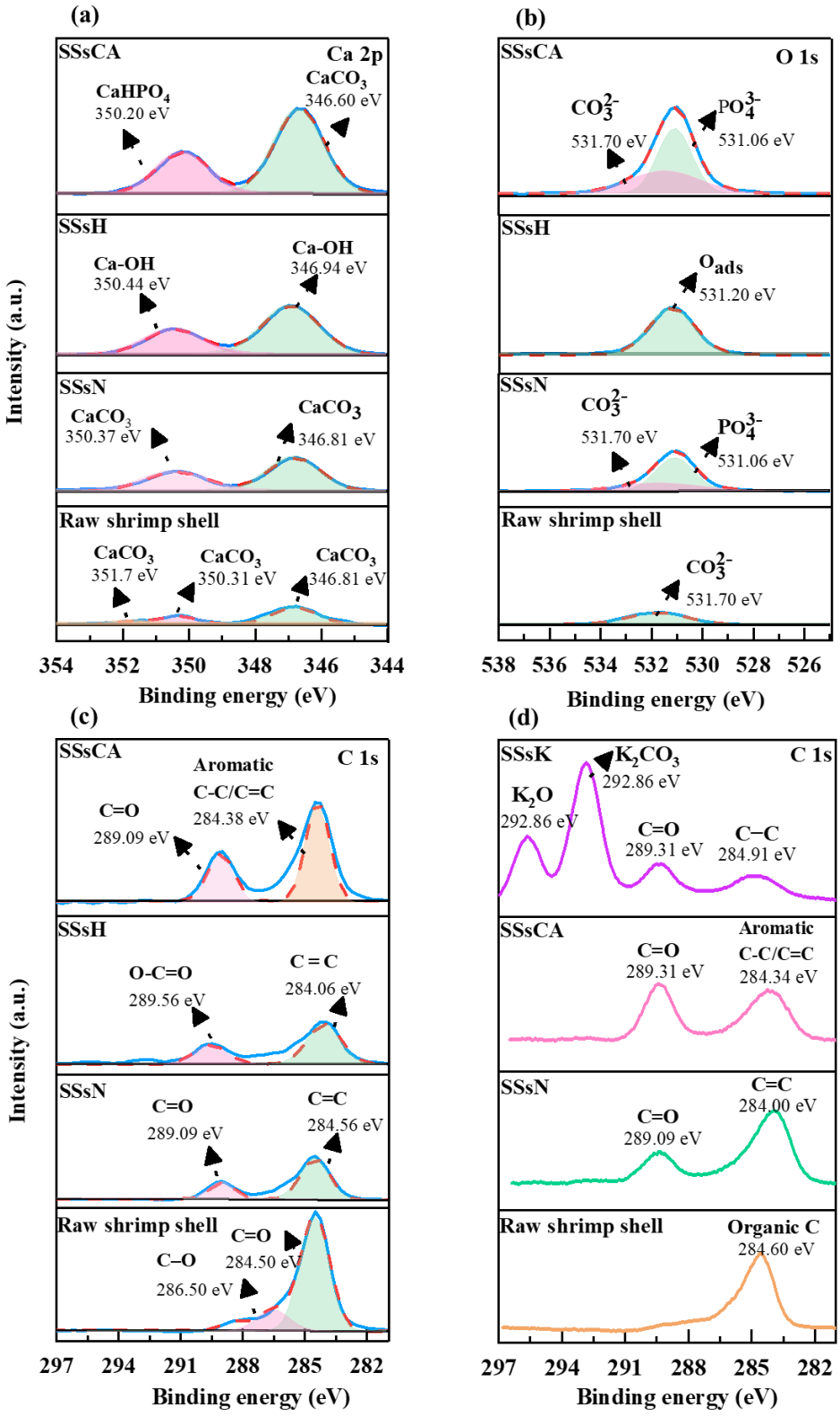

Figure 2.7 XPS spectra of SSs with different modification conditions (a) Ca 2p, (b) O 1s, (c) C 1s, and (d) C 1s. Note: **Figure 2.7a-c** were analyzed using XPS Model: 5500 Ulvac-PHI, and **Figure 2.7d** was further analyzed using Model: Ulvac PHI Quantera SXM.

.

2.4 Chapter summary

This chapter describes the successful fabrication of a shrimp shell-derived adsorbent (SSs) from shrimp shell waste via a pyrolysis process and alkali activation using calcium hydroxide ($Ca(OH)_2$) and potassium hydroxide (KOH). Four different formulations were formed through varying the temperature and types of alkali activators, named as SSsN (pyrolysis only at 700 °C), SSsH (pyrolysis only at 800 °C), SSsCA ($Ca(OH)_2$ + pyrolysis at 700 °C), and SSsK (KOH + pyrolysis at 700 °C). All SS samples exhibited noticeable enhancements in both physical and chemical properties. All SS samples demonstrated increased surface area (S_{BET}) and pore volume (V_{pore}). Increasing the pyrolysis temperature from 700 °C to 800 °C led to a more significant improvement in S_{BET} and V_{pore} than the modification of the type of alkali activator applied. All SSs samples demonstrated a point of zero charge (PZC) ranging from 2.5 to 3. This resulted in a negatively charged surface of SSs during phosphate (PO_4^{3-}) and methyl orange (MO) adsorption, as discussed in the next chapter, which might hinder their adsorption efficiency. As part of chemical property, the formation of hydroxylellestadite (HDL), $CaCO_3$, $Ca(OH)_2$, and potassium sodium calcium chloride carbonate hydrate (KSC) was observed following modification, highlighting a significant change in chemical property. The pyrolyzed samples at 700°C (SSsN and SSsCA) exhibited HDL and $CaCO_3$, whereas the sample activated with KOH (SSsK) demonstrated KSC formation instead of HDL. Furthermore, increasing the temperature to 800°C (SSsH) resulted in the transformation of $CaCO_3$ into $Ca(OH)_2$. The formation was validated through XRD, FTIR, and XPS analyses. The formation of these Ca-based elements may influence the potential adsorption of PO_4^{3-} and MO, as examined in the next chapter.

Chapter 3 Phosphate Removal and Recovery

3.1 Background

The expansion of shrimp aquaculture due to increasing global demand has led to nutrient-rich wastewater and solid waste challenges. This chapter utilized the shrimp shell-derived adsorbent (SSs), produced in the **Chapter 2**, to remove phosphate (PO_4^{3-}) from aqueous solutions. The focus on the removal and recovery of PO_4^{3-} is due to its greater eutrophication risk compared to nitrogen (N) in ecosystems, as well as its status as a limited resource estimated to be exhausted within the next 100 years [142].

From the previous chapter, the SSs are identified as calcium-rich materials. Calcium (Ca) demonstrates a higher affinity for PO_4^{3-} adsorption compared to other elements such as magnesium (Mg), lanthanum (La), aluminum (Al), and iron (Fe), respectively [100]. Moreover, PO_4^{3-} preferentially adsorbs to $CaCO_3$ via ligand exchange as $CaPO_4^-$ [99]. Therefore, this chapter examined the adsorption behavior of SSs in the removal of PO_4^{3-} from aqueous solutions. Adsorption studies and modeling were performed to assess the PO_4^{3-} adsorption efficiency and clarify potential mechanisms on SSs. Additionally, the PO_4^{3-}recovery ratio was calculated using real shrimp pond wastewater data, highlighting the potential of SSs for environmental PO_4^{3-} recovery.

3.2 Phosphate adsorption experiment

To enhance the availability of Ca, SSs prepared through pyrolysis at 700 °C (SSsN) and 800 °C (SSsH), as well as calcium hydroxide ($Ca(OH)_2$)-activated SSs (SSsCA), were selected for testing with PO_4^{3-}.

Dipotassium hydrogen phosphate (K_2HPO_4; 99%, Wako Pure Chemical Industries, Ltd., Japan) was used to prepare synthetic PO_4^{3-} wastewater. SSs were added to the solution at the adsorbent (SSs) to solution ratio (w/v) of 500 mg/L. The pH of the PO_4^{3-} solution was around 8, indicating the basicity of the PO_4^{3-} solution. The mixtures were kept stirring at 400 rpm at room temperature (20 °C) until adsorption equilibrium was reached. The residual concentration of PO_4^{3-} was measured by molybdenum blue method with ascorbic acid using a UV-VIS spectrophotometer (UV-VIS; UV-2550, Shimadzu, Japan) at a maximum wavelength of 880 nm [143]. PO_4^{3-} adsorption capacity(q_t) of SSs was determined from the following **Equation 3.1**.

$$q_t = \frac{(C_0 - C_t)}{m} V \quad \textbf{(3.1)}$$

where C_0 and C_t represent the initial and the residual PO_4^{3-} concentration (mg/L), respectively, V is the volume of the solution (L), and m represents the weight of the adsorbent (g).

3.3 Phosphate removal performance

3.3.1 Comparison of adsorption performances

The adsorption performances of each SSs were compared based on the PO_4^{3-} adsorption capacity (q_e) at a concentration of 300 mg/L. The contact time was varied from 0 min to 48 h (2,880 min) as illustrated in **Figure 3.1a, 3.1b, and Table 3.1**.

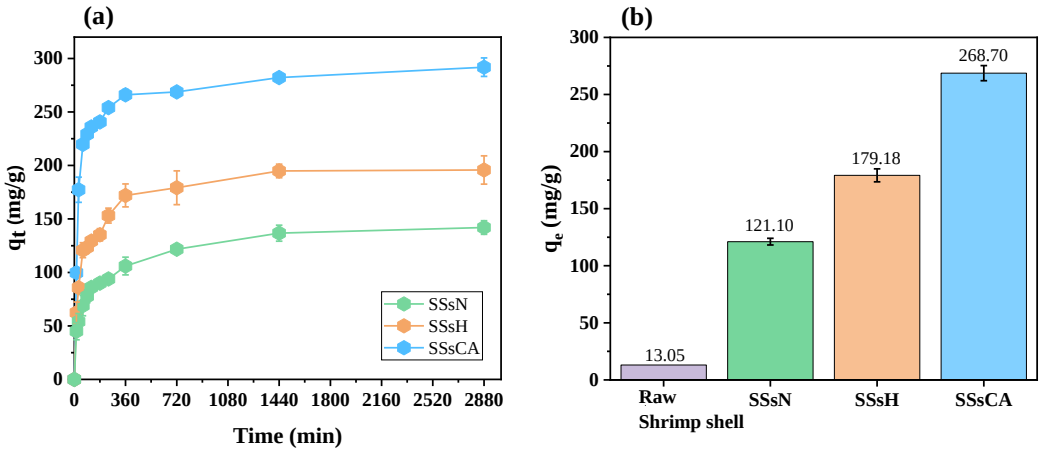

Figure 3.1 Adsorption data of PO_4^{3-} onto SSs (a) Comparison of q_e, and (b) Influence of contact time on PO_4^{3-} removal by each SSs.

Figure 3.1 illustrates that all SSs started the adsorption of PO_4^{3-} ions immediately after initial contact. The adsorption rate was remarkably rapid during the first 2 h and progressively slowed until equilibrium was attained. This result may be ascribed to the abundant adsorption sites of the SSs for capturing PO_4^{3-} ions in the solution during the initial contact. As time progressed, the number of unoccupied active sites reduced leading to a reduced adsorption rate. As illustrated in Figure 3.1a, SSsCA, SSsN, and SSsH approached equilibrium after 12 h (720 min) of contact time in PO_4^{3-} solution. As shown in Figure 3.1b, the q_e of raw shrimp shell performed poorly was very low (13.04 mg/g) due to the lack of active metal component. After modification, all SSs exhibited a high adsorption capacity for PO_4^{3-}, indicating that the prepared SSs samples are suitable for the adsorption of PO_4^{3-}. Notably, SSsCA exhibited the highest adsorption capacities. The q_e of SSsN, SSsH and SSsCA were 121.10, 179.18 and 268.70 mg/g, respectively. The XRD, FTIR and XPS analyses confirmed PO_4^{3-} adsorption onto

all SSs, with the phosphate present in various forms, including calcium apatite (Ca-apatite), monocalcium phosphate ($Ca(H_2PO_4)_2$), and dicalcium phosphate ($CaHPO_4$), as shown in **Figure 2.5.-2.7**.

Table 3.1 Experimental data and standard errors of PO_4^{3-} (300 mg/L) adsorption capacity for each SSs as a function of time.

Time (min)	PO_4^{3-}adsorbed onto each SSs in solution, q_t (mg/g)					
	SSsN		SSsH		SSsCA	
	q_t (mg/g)	Standard deviation	q_t (mg/g)	Standard deviation	q_t (mg/g)	Standard deviation
0	0	0	0.00	0.00	0.00	0.00
15	45.04	8.04	62.42	9.91	99.70	0.63
30	54.07	7.54	85.77	1.53	177.32	11.77
60	69.04	9.51	120.80	6.99	219.75	1.61
90	77.64	6.02	123.50	3.18	229.30	0.43
120	86.02	2.83	129.33	2.54	236.00	3.86
180	90.03	4.3	135.17	5.72	240.67	1.84
240	93.87	3.71	153.13	6.99	254.09	3.37
360	105.99	8.29	172.00	10.72	266.06	4.93
720	121.68	2.86	179.18	15.79	268.70	3.48
1440	136.7	7.45	194.90	6.34	282.12	1.73
2880	141.98	6.31	195.80	13.21	291.88	8.65

3.3.2 Adsorption kinetics

To analyze the kinetic mechanism of adsorption process, the experimental data was fitted with the pseudo-first order (PFO), pseudo-second order (PSO), and Elovich models at an initial PO_4^{3-} concentration of 300 mg/L. The PFO model illustrates the mechanism of adsorption, indicating that the rate at which sites become occupied is directly related to the number of unoccupied sites (physisorption), while the PSO model suggests the rate-limiting step (chemisorption) [144]. Furthermore, the Elovich model describe chemisorption on heterogeneous active sites [145]. To further elaborate the diffusion mechanism, the adsorption

kinetic data was also analyzed using the intraparticle diffusion model. The equations for adsorption kinetic models are described in **Table 3.2**.

Table 3.2 Adsorption kinetic models [146, 147].

Equation	Non-linear form	Parameter
Pseudo-first order	$q_t = q_e(1 - e^{-k_1 t})$	k_1: the pseudo-first order kinetic rate constant (min^{-1})
Pseudo-second order	$q_t = \frac{q_e^2 k_2 t}{1 + q_e k_2 t}$	k_2: the pseudo-second order kinetic rate constant (g/mg.min)
Elovich	$q_t = \frac{1}{\beta}\ln(1 + \alpha\beta t)$	α: the adsorption rate (mg/g.min) β: the desorption constant (g/mg)
Intraparticle diffusion model	$q_t = k_i t^{\frac{1}{2}} + C$	k_i: the intraparticle diffusion rate constant (mg/g. min) C: the intercept, which provides insight into the boundary layer effect (mg/g)

The adsorption experimental data fitted better with the PSO model with a higher regression coefficient range (r^2 = 0.945-0.988) than the PFO model (r^2 = 0.855-0.964) and the Elovich model (r^2 = 0.904-0.939) (see **Table 3.3 and Figure 3.2**). The PSO model suggests that the chemisorption is the primary adsorption mechanism. The PSO model suggests that the chemisorption is the primary adsorption mechanism. Similar findings for PO_4^{3-} adsorption onto crawfish char suggested the possible mechanisms involving surface adsorption, precipitation, exchange of cations, and complexation processes [148, 149]. The PSO model suggests that the chemisorption is the primary adsorption mechanism.

Meanwhile, the intraparticle diffusion model showed a high linear dependency on the square root of time ($r^2 > 0.90$), implying that intraparticle diffusion was also involved in this adsorption. The line did not pass through the origin with high intercept value (C > 0) (see **Fig. 3b**), indicating that the adsorption was governed by multiple processes [150]. The intraparticle diffusion of PO_4^{3-} within all SSs occurred in three stages. The first stage (external diffusion) is a steep slope (high k_{i1} values), reflecting a fast adsorption rate due to available active sites. Subsequently, the diffusion rates decreased ($K_{i2} < K_{i1}$) in the second stage (intraparticle diffusion) (See **Table 3.3 and Figure 3.2**). The external surface-active sites were occupied by PO_4^{3-}, which began to diffuse into the pores. In the third stage (saturation), the slope is close

to 0, indicating the adsorption equilibrium. These findings are in agreement with the results on PO_4^{3-} adsorption onto other biochars [151].

Table 3.3 Adsorption kinetic parameters for SSs at 20 ℃.

Adsorption parameters	SSs samples		
	SSsN	**SSsH**	**SSsCA**
q_e, exp (mg/g)	121.10	179.18	268.70
PFO			
k_1 (min^{-1})	0.012	0.016	0.032
q_e, cal (mg/g)	120.61	173.31	262.46
r^2	0.855	0.899	0.964
PSO			
k_2 (g/mg.min)	$1.29x10^{-4}$	$1.25x10^{-4}$	$1.62x10^{-4}$
q_e, cal (mg/g)	132.51	189.50	283.17
r^2	0.945	0.971	0.988
Elovich			
α (mg/g.min)	0.050	0.038	0.033
k_e (g/mg)	10.527	28.667	315.85
r^2	0.936	0.939	0.904
Intraparticle diffusion			
First step			
k_{i1} ($mg/g.min^{0.5}$)	10.197	15.744	31.149
C (mg/g)	1.256	0.327	0.410
r^2	0.991	0.999	0.987
Second step			
k_{i2} ($mg/g.min^{0.5}$)	3.053	4.681	4.033
C (mg/g)	48.392	79.645	189.85
r^2	0.981	0.976	0.993
Third step			
k_{i3} ($mg/g.min^{0.5}$)	0.723	0.582	0.848
C (mg/g)	104.67	166.98	247.44

r^2	0.933	0.939	0.982

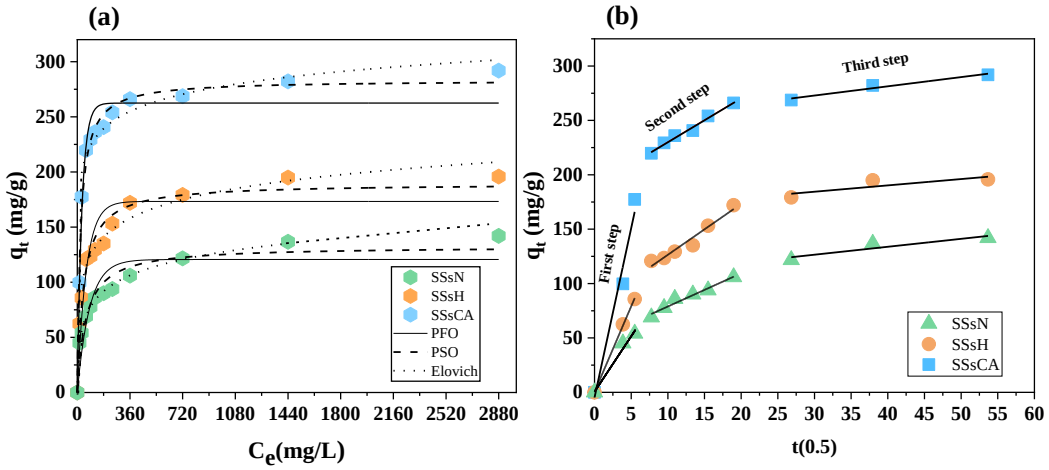

Figure 3.2 Adsorption of PO_4^{3-} by using SSs with different modification (a) Adsorption kinetic, and (b) Intraparticle diffusion model.

3.3.3 Adsorption isotherm

Adsorption isotherm is the equilibrium relationship between adsorbent and adsorbate. The isotherm study provides crucial information on the maximum adsorption capacity and adsorption characteristics [152]. In this work, the obtained adsorption data were fitted with Langmuir, and Freundlich isotherms by varying the initial PO_4^{3-} concentrations (20, 50, 100, 200, 300, 400, and 500 mg/L). The Langmuir model assumes monolayer adsorption occurring on the specific homogeneous site, while the Freundlich model considers multilayer adsorption. The non-linear isotherm equations are shown in **Table 3.4**.

Table 3.4 Adsorption isotherms models [146, 147].

Equation	Non-linear form	Parameter
Langmuir	$q_e = \frac{q_{max} k_L C_e}{1 + k_L C_e}$	k_L: the Langmuir constant (L/mg)
Freundlich	$q_e = k_F . C_e^{1/n}$	k_F: the Freundlich constant (mg/g)(L/mg)$^{1/n}$) n: the adsorption intensity constant

The Langmuir and Freundlich isotherm models were also used to fit the adsorption equilibrium data (see **Figure 3.3**). The adsorption isotherm and calculated parameters of all

SSs are shown in **Table 3.5** and **Figure 3.3**. The adsorption capacity increased with the initial PO_4^{3-} concentration. The experimental data fitted better with the Langmuir model (r^2 = 0.947-0.992) than the Freundlich model (r^2 = 0.911-0.979), indicating monolayer adsorption. Among the three SSs, SSsN had the lowest maximum adsorption capacity (q_{max}) (162.04 mg/g). Since the XRD, FTIR, and XPS results indicated the formation of calcium-phosphate (Ca-P) groups. The adsorption of PO_4^{3-} onto SSs was influenced by surface precipitation via the released Ca^{2+} on the surface from hydroxylellestadite (HDL), calcium hydroxide ($Ca(OH)_2$), and calcium carbonate ($Ca(CO)_3$), along with ligand exchange between CO_3^{2-} in $CaCO_3$ and PO_4^{3-} (as shown in **2.4.-2.6).** The adsorption mechanism would be further discussed in the **section 3.5**. On the other hand, increasing the pyrolysis temperature to 800 ℃ (SSsH) resulted in a higher q_{max} (229.43 mg/g). The heat treatment at 800 ℃ is conducive to increasing the S_{BET} (96.692 m^2/g) and V_{pore} (0.182 cm^3/g), improving the adsorption capacity of SSsH for PO_4^{3-} removal (see **Table 2.1**).

Table 3.5 Adsorption kinetic isotherm parameters for SSs at 20 ℃.

Adsorption parameters	SSs samples		
	SSsN	**SSsH**	**SSsCA**
Langmuir isotherm			
k_L (L/mg)	0.015	0.012	0.012
q_{max} (mg/g)	162.04	229.43	381.24
r^2	0.992	0.947	0.979
Freundlich isotherm			
k_F $(mg/g)(L/mg)^{1/n}$	15.06	24.73	21.00
n	0.379	0.346	0.469
r^2	0.979	0.925	0.911

Furthermore, XRD analysis indicated $Ca(OH)_2$ in SSsH, which has higher reactivity and ability to produce free Ca^{2+} and $CaOH^+$ for favoring calcium phosphate (Ca-P) precipitation than $CaCO_3$ [105, 140]. However, the addition of $Ca(OH)_2$ provided a much higher ability to adsorb PO_4^{3-}, with the highest q_{max} of 381.24 mg/g, than pyrolysis activation alone (SSsN and SSsH) (see **Table 3.5**). It can be speculated that the C═C aromatic bonds in SSsCA should also participate in PO_4^{3-} adsorption as indicated by its decreased peak intensity in XPS spectrum

(see **Fig. 2c**). Owing to its surface containing π electron-rich groups (such as C=C), SSsCA could provide electrons to interact with PO_4^{3-}, promoting the adsorption [115].

Notably, the adsorption capacity of PO_4^{3-} onto SSs exhibited prominent adsorption performance compared to other modified crustacean biochar reported in literature (see **Table 3.6**). In particular, the adsorption of PO_4^{3-} on the shrimp shell-derived biochar (SSs) in this study is strongly influenced by its calcium (Ca) content. Although previous studies used adsorbents made from freshwater shrimp species, such as crawfish or crayfish, these freshwater species generally have a lower calcium content, ranging from 17.0–41.2%, as shown by XRF analysis (see **Figure 1.9**) [98, 149]. In contrast, the shrimp shells used in this research, sourced from marine species, have a much higher Ca content of 82.7% (confirmed through XRF analysis). This higher Ca content is essential for improving PO_4^{3-} adsorption because Ca promotes the formation of Ca-P compounds. The significant difference in Ca content between marine and freshwater shrimp-derived adsorbents explains the better PO_4^{3-} adsorption efficiency achieved in this study. Therefore, these findings clearly distinguish my research from two previous studies, highlighting the benefits of using shrimp shell biochar with higher Ca levels for PO_4^{3-} removal.

Moreover, Yan et al. (2022) [149] studied a novel crayfish shell biochar-Fe composite (FXB), which investigated PO_4^{3-} adsorption in a binary system alongside Cr(VI) removal. However, the exact adsorption performance for PO_4^{3-} was not explicitly reported. In binary systems, competitive interactions between Cr(VI) and PO_4^{3-} can significantly affect the adsorption efficiency of each pollutant. In contrast, this study focuses exclusively on PO_4^{3-} adsorption, enabling a more detailed analysis of the adsorption performance and the underlying mechanisms specific to PO_4^{3-} removal. Hence, using shrimp shell waste as a Ca source for the Ca-loaded adsorbent preparation displays great potential for PO_4^{3-} removal.

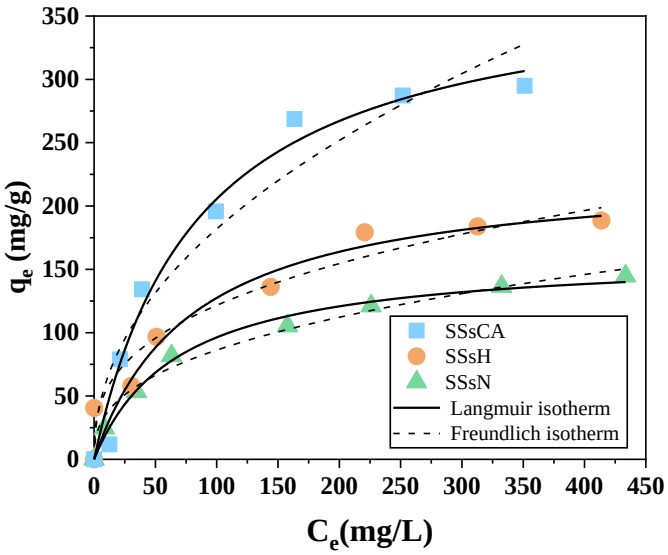

Figure 3.3 Adsorption isotherm of PO_4^{3-} by using SSs with different modification.

Table 3.6 Comparison of the adsorption performances of PO_4^{3-} with other reported crustacean based-biochars.

Adsorbent	q_{max} (mg/g)	q_{max} determination	Ref.
Crayfish shell biochar-Fe composite	3.82	Langmuir	[97]
Chitosan modified sugarcane bagasse biochar	37.20	Langmuir	[153]
Crawfish char	70.90	Langmuir	[148]
Crab shell biochar	209.35	Langmuir	[120]
Chitosan modified magnesium with corn straw biochar	221.89	Langmuir	[154]
SSsN	162.04	Langmuir	This work
SSsH	229.43	Langmuir	This work
SSsCA	381.24	Langmuir	This work

3.4 Adsorption thermodynamic

Three thermodynamic parameters, including changes in the Gibbs free energy (ΔG°), enthalpy (ΔH°), and entropy (ΔS°), were calculated at different temperatures (20, 35, and

45 °C) to examine the feasibility and nature of the adsorption process. The values of ΔH° and ΔS° can be evaluated using the Van't Hoff equation as follows (see **Equation 3.2**):

$$\ln k_L = \frac{\Delta H^\circ}{RT} - \frac{\Delta S^\circ}{R} \quad \textbf{(3.2)}$$

where k_L (L/mg) is the residual PO_4^{3-} adsorption distribution coefficient, R is the universal gas constant (8.314 J/mol/K), and T is the absolute temperature (K). The slope and intercept of the linear plot of $\ln K_d$ *vs.* 1/*T* were used to calculate the ΔH° and ΔS°, thereafter, ΔG° can be derived according to the following **Equation 3.3**:

$$\Delta G^\circ = \Delta H^\circ - T\Delta S^\circ \quad \textbf{(3.3)}$$

The adsorption thermodynamic of PO_4^{3-} onto SSs are shown in **Table 3.7 and Figure 3.4**. The obtained positive values of ΔG° (8.03 - 11.01 kJ/mol) at all the studied temperatures indicated a nonspontaneous reaction. ΔG° values decreased with increasing temperature, suggesting improved PO_4^{3-} removal at higher temperatures. The positive ΔS° (119.21kJ/mol) suggested increased freedom at the interface between the PO_4^{3-} and SSsCA. The positive ΔH° (45.95 kJ/mol) confirmed endothermic adsorption, where the increase of temperature is conducive to the adsorption process. As the temperature increases, the mobility and diffusion of PO_4^{3-} into the inner side of SSs improve, and the internal structure of SSs also expands, allowing PO_4^{3-} to penetrate deeper. This result agrees with previous studies on PO_4^{3-} adsorption by shell biochar, such as oyster shell biochar [155] and iron hydroxide-eggshell biochar [156]. rises with temperature, reflecting its enhanced ability to adsorb the dye molecules.

Simultaneously, the magnitude of ΔH° provides information about the type of adsorption. The ΔH° of physisorption is 2.1–20.9 kJ/mol, while that of chemisorption may reach values between 40 and 120 kJ mol^{-1} [157]. In this study, the values of ΔH° (45.95 kJ/mol) for PO_4^{3-} were in the range of chemisorption. The interpretation of thermodynamic results aligns with the PSO model.

Table 3.7 Thermodynamic parameters for SSsCA.

T (°C)	ln(K_d) (L/g)	ΔH° (KJ/mol)	ΔS° (J/mol•k)	ΔG° (KJ/mol)

20	-4.448			11.01
35	-3.774	45.95	119.21	9.22
45	-2.924			8.03

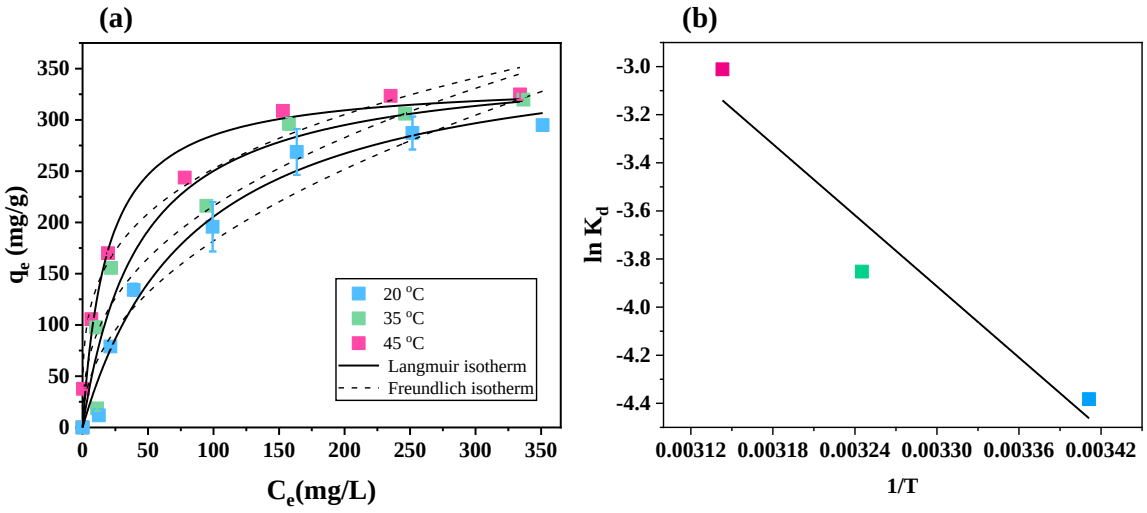

Figure 3.4 Adsorption thermodynamic of PO_4^{3-} by using SSs with different modification (a) Isotherm plots for the PO_4^{3-} adsorption onto SSsCA at different temperatures, and (b) Thermodynamic parameters fitted by the van't Hoff equation of SSsCA.

3.5 Adsorption mechanisms of phosphate onto shrimp shell-derived adsorbent

Based on the results obtained from the isotherm, kinetics, thermodynamic studies, and characterization, it could be concluded that PO_4^{3-} adsorption onto SSs primarily occurs through **3.5.1 Ca^{2+}-induced chemical precipitation**, where Ca^{2+} ions released from the SSs surface combine with PO_4^{3} ions to form Ca-P precipitates. In addition to chemical precipitation, 3.4.2 **3.5.2 other mechanisms including ligand exchange** (where PO_4^{3-} displaces CO_3^{2-} from $CaCO_3$ on SSs surface) and **anion–π interactions** (where PO_4^{3-} interacts with aromatic rings in the SSs m) also contribute to the adsorption process. Besides, the characteristic form of PO_4^{3-} changes with pH due to its ability to exist in different protonated forms in aqueous solutions. PO_4^{3-} could be existed in the forms of H_3PO_4, $H_2PO_4^-$, HPO_4^{2-}, and PO_4^{3-} (pK_1 = 2.15, pK_2 = 7.20, and pK_3 = 12.33) [1, 158] (see **Figure 3.5**). Since the pH of the working solution in this study was 8, $H_2PO_4^-$ and HPO_4^{2-} are the prominent presence of PO_4^{3-} anions.

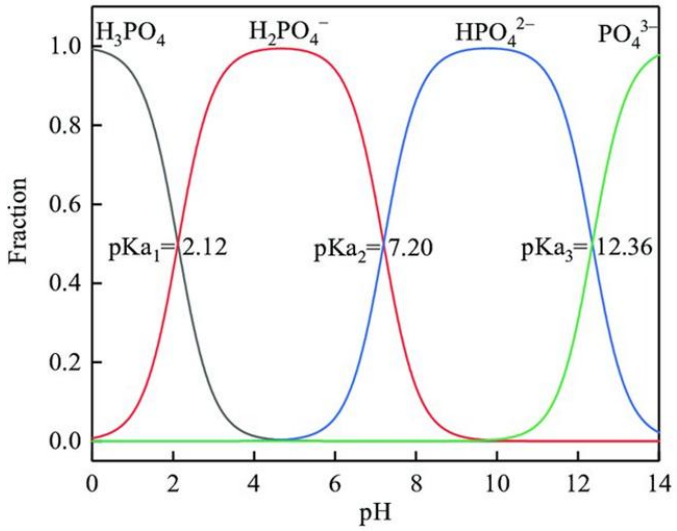

Figure 3.5 Distribution of PO_4^{3-} species in varying pH conditions [1].

3.5.1 Ca^{2+}-induced chemical precipitation

When SSs was added into PO_4^{3-} solution, PO_4^{3-} (mainly HPO_4^{2-} and HPO_4^{3-}) might be primarily attached onto the monolayer surface of SSs due to their enhanced surface morphology and pore structure. Free Ca^{2+} and $CaOH^+$ might be released from the SSs surface for adsorbing PO_4^{3-} via three pathways: **Dissolution of calcium silicate hydrate (CSH) in HDL**, **Hydrolysis of $Ca(OH)_2$**, and **Ligand exchange with $Ca(CO)_3$**.

❖ **Dissolution of calcium silicate hydrate in HDL**

On the SSs surface, HDL has unembeds CSH structure, which could release Ca^{2+} at pH=8. The release of Ca^{2+} from the SSs surface into the surrounding solution can interact with PO_4^{3-}adsorption through chemical precipitation.

❖ **Hydrolysis of $Ca(OH)_2$**

$Ca(OH)_2$ was gradually hydrolyzed to produce Ca^{2+} and $CaOH^+$ (OH^- combined) [140] (see **Equation 3.4 and 3.5**). Finally, these free Ca^{2+} and $CaOH^+$ would combine with PO_4^{3-} to form Ca-P precipitates.

$$Ca(OH)_2 \xrightarrow{water} Ca^{2+} + 2OH^- \quad \textbf{(3.4)}$$

$$Ca^{2+} + H_2O \leftrightarrow CaOH^+ + H^+ \quad \textbf{(3.5)}$$

❖ **Ligand exchange with $Ca(CO)_3$.**

Since PO_4^{3-} has a higher affinity for Ca than carbonate CO_3^{2-} due to the larger ionic radius and higher charge of PO_4^{3-}. Therefore, the weaker ligand (CO_3^{2-}) is displaced by a stronger PO_4^{3-} to further form more stable Ca-P bonds.

The XRD, FTIR, and XPS analyses confirmed the formation of various Ca-P groups, including calcium apatite (Ca-apatite), monocalcium phosphate ($Ca(H_2PO_4)_2$), and dicalcium phosphate ($CaHPO_4$), on the saturated SSs. The Ca-P precipitates consisted of $Ca_{10}(PO_4)_6OH_2$ and $CaHPO_4$, indicated by XRD analysis (see **Figure 3.6**).

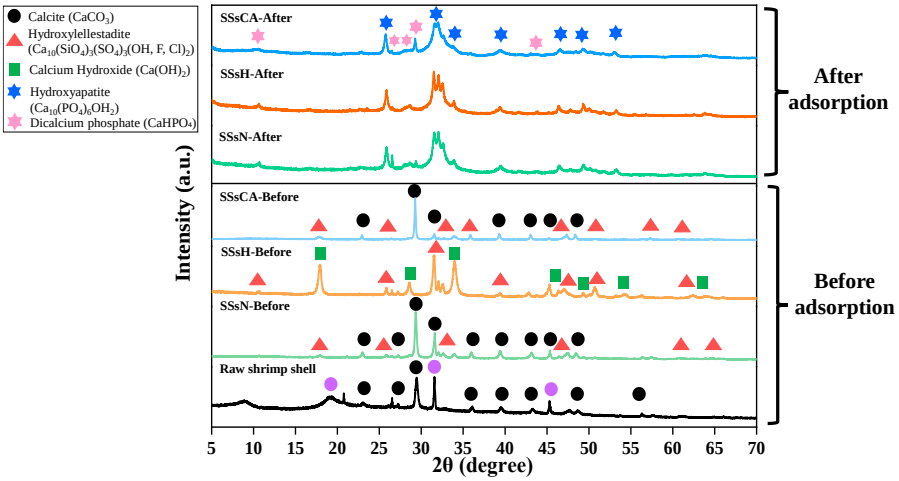

Figure 3.6 XRD pattern of SSs with different modification conditions before and after PO_4^{3-} adsorption.

The contribution of Ca-precipitation into adsorption mechanism can also be reflected by the variations in functional groups before and after adsorption from FTIR and XPS analyses results (see **Figure 3.7 and 3.8**). The FTIR peaks at 1632, 1017, and 970 cm^{-1} were ascribed to PO_4^{3-} and HPO_4^{2-} vibration of $Ca_{10}(PO_4)_6OH_2$ [159-161]. Other peaks at 600 and 560 cm^{-1} also indicated the PO_4^{3-} of Ca-P precipitates, i.e., Ca-apatite and $CaHPO_4$ [162](see **Figure 3.7**). Similarly, **Figure 3.8** shows that All Ca 2p shifted to higher binding energy, indicating the transformation of Ca-O linkages into Ca-P linkages. After adsorption, the Ca 2p spectra were fitted with peaks at 347, 347.50, 350.50, and 350.90 eV, reflecting Ca-P precipitates [163] (see **Fig.3.8a**). A new P 2p peak at 133.05 eV appeared in the XPS spectra, indicating P precipitation with Ca^{2+} from CSH [164]. The peaks at 133.4, 134.4, and 134.8 eV were related to $CaHPO_4$ and $Ca(H_2PO_4)_2$ [88, 165, 166] (see **Fig. 3.8d**).

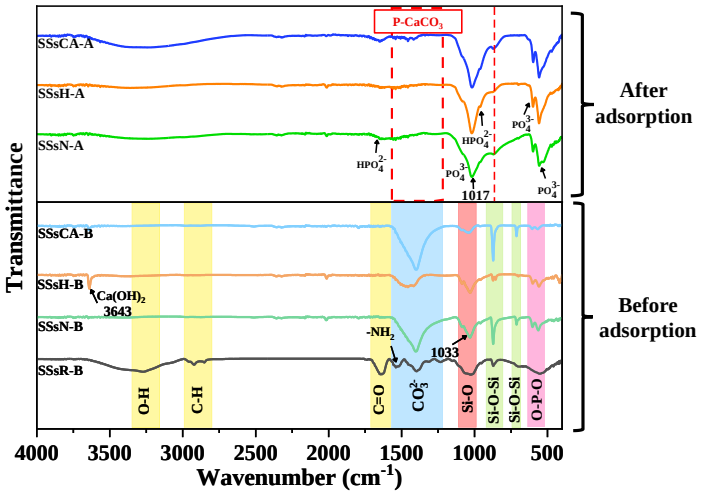

Figure 3.7 FT-IR spectra of SSs before and after PO_4^{3-} adsorption.

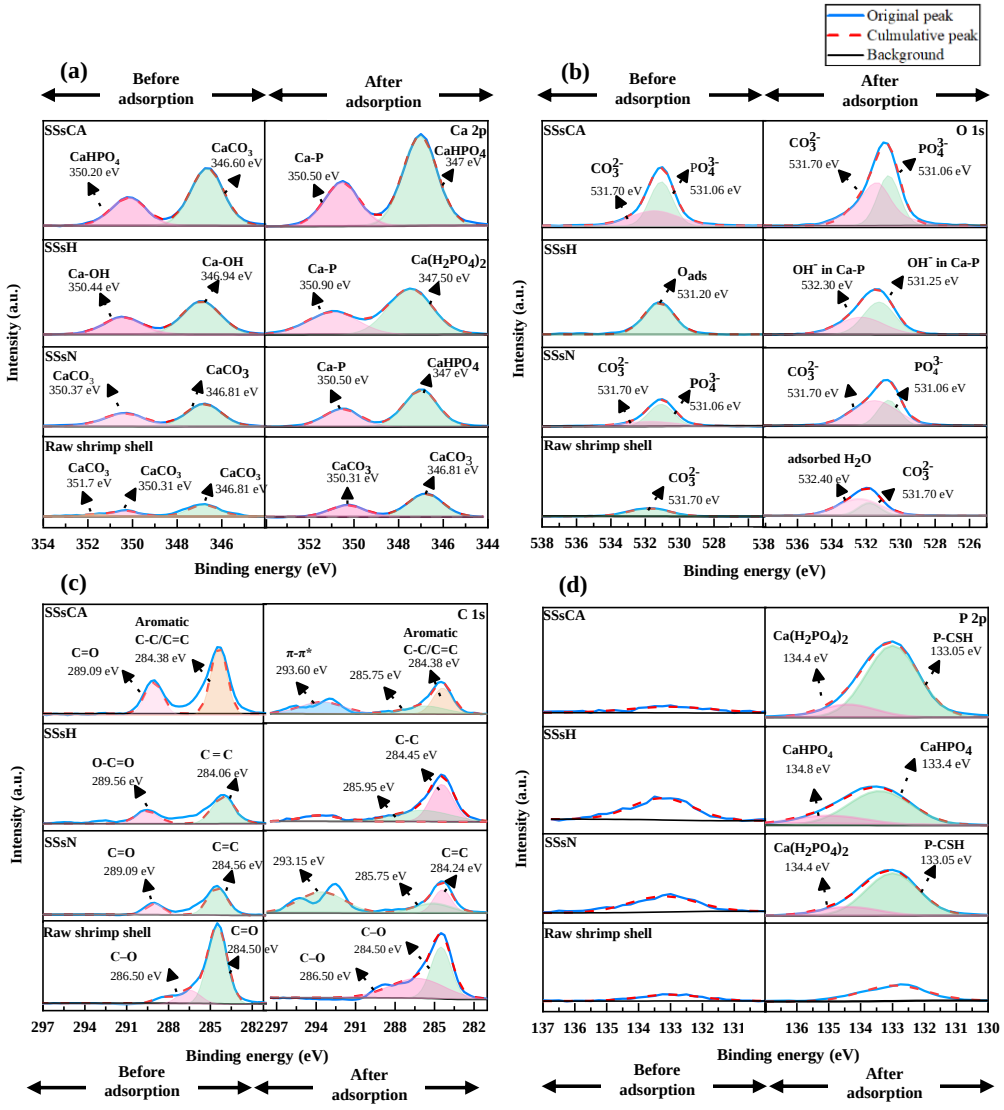

Figure 3.8 XPS spectra of SSs before and after PO_4^{3-} adsorption

(a) Ca 2p, (b) O 1s, (c) C 1s, and (d) P 2p.

3.5.2 Other mechanisms including ligand exchange and anion–π interaction.

Another important removal mechanism under these conditions was ligand exchange whereby $H_2PO_4^-$ and HPO_4^{2-} anions replaced CO_3^{2-} on the SSs surface and formed complexes via Lewis acid-base interactions [87, 167], as confirmed by the FTIR results (see **Figure 3.8**). The disappearance of CO_3^{2-} stretching at ~1400 cm^{-1} and the appearance of CO_3^{2-}-derived peak at ~870 cm^{-1} revealed the occurrence of ligand exchange between PO_4^{3-} and CO_3^{2-}, where PO_4^{3-} replaced CO_3^{2-} to combine with Ca^{2+} to form Ca-P groups [168]. At the same time, CO_3^{2-} may be displaced into the solution, driving the more vigorous intensity of CO_3^{2-} peaks in the O 1s (see **Figure 3.8b**). Moreover, the PO_4^{3-} adsorption on SSsCA also incluced π-π interaction. The content of C 1s peak at 284.38 eV decreased, and the characteristic peak of π–π was observed at 293.60 eV [169] (see **Fig. 3.8c**) in SSsCA sample.

However, normally, π–π interaction happens when two aromatic rings get close [2] (See **Figure 3.9**). In this work, aromatic ring was observed in the SSsCA sample. Aromatic rings, with their electron-rich regions, can interact with negatively charged species like PO_4^{3-} through a type of interaction known as anion–π interaction instead of the typical π–π interaction [2] (see **Figure 3.9**). Therefore, this work indicated anion–π interaction in PO_4^{3-} adsorption by SSsCA.

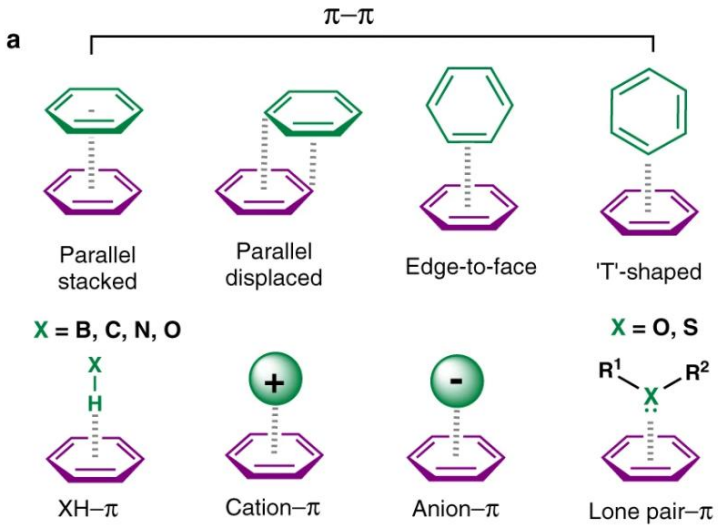

Figure 3.9 Non-covalent interactions involving π systems [2].

Therefore, though electrostatic repulsion existed between SSs and PO_4^{3-} (see **Zeta potential results in section 2.1**), it can be easily overcome by the strong adsorption of PO_4^{3-} onto SSs. Diverse pathways of PO_4^{3-} adsorption with shrimp shell-derived adsorbent, including chemical precipitation, ligand exchange, anion-π interaction, and physical adsorption, occurred. **Table 3.8** concluded the potential adsorption mechanisms in each SSs. In the SSsCa

sample, which exhibited the highest adsorption, these pathways— including Ca-precipitation, Ligand Exchange, π -π interaction, and physical— cooperate to promote efficient adsorption. This study provides a sustainable way to manage shrimp shell waste while enabling P recovery, thus contributing to a circular system in shrimp aquaculture.

Table 3.8 Possible PO_4^{3-} adsorption mechanism in each SSs.

SSs	Ca-precipitation	Ligand Exchange	Anion -π interaction	Surface area and porosity
SSsN	✓	✓		✓
SSsH	✓			✓
SSsCA	✓	✓	✓	✓

The results from this research support the model mechanisms in **Figure 1.8** in some aspects, but there are differences in certain mechanisms. **Figure 1.8** illustrates the nutrient (NH_4^+, NO_3^-, and PO_4^{3-}) adsorption mechanisms of biochar, which include several processes such as surface area, electrostatic adsorption, ion exchange, functional group interactions, and precipitation (see **Table 3.8**). This research focused on PO_4^{3-} adsorption using SSs, and the results align with some of these mechanisms, such as chemical precipitation, ligand exchange, and physical adsorption. However, the model did not fully account for the importance of anion–π interactions, which were significant in this work.

Meanwhile, this study did not observe a significant role for surface functional groups or electrostatic attraction in the adsorption mechanism. Many biochars, particularly those pyrolyzed at lower temperatures, contain oxygenated functional groups (e.g., -OH, COOH) that attract NH_4^+ rather than PO_4^{3-}. The solution pH in this study also exceeded the point of zero charge (pH_{ZCP}) of the SSs, causing the negative surface charge to carry a negative charge. negatively charged surface hindered the adsorption of PO_4^{3-}.

3.6 Recovery of phosphate from real shrimp pond wastewater

Shrimp farming generally produces wastewater that contains high levels of nutrients, particularly PO_4^{3-}. Through the efficient removal and recovery of PO_4^{3-} by using SSs results, PO_4^{3-} was effectively depleted from aqueous solution while promoting an opportunity for nutrient recycling. With the Langmuir model on experimental data from shrimp pond wastewater from **Section 3.3** allows for the prediction of PO_4^{3-} recovery from real shrimp pond wastewater. This model suggests monolayer adsorption on a uniform surface, facilitating theoretical estimations of phosphate recovery efficiency. The recovery ratio determines the amount of phosphate removal from wastewater relating to the initial concentration. The recovery PO_4^{3-} ratio using the following **Equation 3.6**:

$$R(\%) = \frac{C_0 - C_f}{C_0} x\ 100 \quad \textbf{(3.6)}$$

Where q_e represents the recovery ratio, C_0 represents the initial phosphate concentration (mg/L), and C_f represents the final concentration after treatment (mg/L).

The study area was conducted on shrimp ponds located in southern Thailand. Southern Thailand currently serves as a leading producer of shrimp. This region is suitable to shrimp farming due to its coastal geography, adjacency to mangroves and estuaries, availability of brackish water, and tropical temperature, which all provide optimal conditions for intensive aquaculture. However, they can be detected by high nutrient concentrations due to shrimp feed, organic matter decomposition, and the application of fertilizers to promote eutrophication (see **Table 3.6**). Therefore, this area suitable for shrimp cultivation and the study of nutrient recovery measures.

Case study: Phosphate recovery in a shrimp pond in southern thailand background site description

- **Location**: Shrimp farms in Southern Thailand with a pond area of 488,883,200 m²
- **Pond Volume**: Approx. 359,328,480 m³ (359,328,480,000 L)
- **Water Exchange Volume:** 107,798,544 m³/day (107,798,544,000L/day.)
- **Water Quality**:
    - Initial PO_4^{3-} concentration (C_0): 0.54 mg/L.

Methodology

1. **Selection of adsorbent**:

- **Material**: Shrimp shell biochar modified with calcium hydorxide ($Ca(OH)_2$) (SSsCA)
- **Adsorbent Dosage**: Initial trials use 0.5 g/L based on lab-scale optimization.

2. Steps for calculation

2.1 Langmuir isotherm equation:

$$q_e = \frac{q_{max} k_L C_f}{1 + k_L C_f} \quad \textbf{(3.7)}$$

q_e: Adsorbed amount of PO_4^{3-} at equilibrium (mg/g).

q_{max}: Maximum adsorption capacity (mg/g).

C_e: Equilibrium concentration of PO_4^{3-} in solution (mg/L).

K_L: Langmuir constant related to the affinity of binding (L/mg).

Note: Form **Section 3.3**, Maximum adsorption capacity (q_{max}): 381.24 mg/g.

Langmuir constant (K_L): 0.012 L/mg.

2.2 Determine adsorption capacity at target concentration:

$$q_e = \frac{(C_0 - C_f)}{m} . V \quad \textbf{(3.8)}$$

C_0: Initial PO_4^{3-} concentration (mg/L)

C_f: Residual PO_4^{3-} concentration (mg/L)

V: Volume of the solution (L)

M: Weight of the adsorbent (g)

2.3 Solve for C_f by equating langmuir (3.7) and mass balance equations (3.8)

Equating the two equations:

$$\frac{q_{max} . k_L . C_f}{1 + k_L . C_f} = \frac{(C_0 - C_f)}{m} . V$$

Rearranging the equation

Multiply through by $1 + k_L C_f$ to eliminate the denominator:

$$q_{max} . k_L . C_f = \frac{(C_0 - C_f) . v}{m} . 1 + k_L . C_f$$

Expand the terms on the right-hand side:

$$q_{max} . k_L . C_f = \frac{(C_0 - C_f) . v}{m} + \frac{(C_0 - C_f) . v . k_L . C_f}{m}$$

Rearrange the equation to isolate terms with C_f

$$q_{max} . k_L . C_f . m = (C_0 - C_f) . v + (C_0 - C_f) . v . k_L . C_f$$

$$q_{max}.k_L.C_f = \frac{C_0.v}{m} - \frac{C_f.v}{m} + \frac{C_0.v.k_L.C_f}{m} - \frac{C_f.v.k_L.C_f}{m}$$

$$q_{max}.k_L.C_f = \frac{C_0.v}{m} - \frac{C_f.v}{m} + \frac{C_0.v.k_L.C_f}{m} - \frac{C_f.v.k_L.C_f}{m}$$

Bring all terms involving C_f to one side of the equation:

$$\frac{v.k_L.c_f^2}{m} + \left(\frac{v}{m} - \frac{C_0.v.k_L}{m} - q_{max}.k_L\right).C_f - \frac{C_0.v}{m} = 0$$

Solving for C_f

Once the equation is rearranged to isolate C_f

$$a.c_f^2 + b.C_f + c = O$$

Where a, b, and c are constants derived from **q_{max}, C_e, K_L, C_0, V and m**

- $a = \frac{v.k_L}{m}$
- $b = q_{max}.k_L + \frac{v}{m} - \frac{C_0.v.k_L}{m}$
- $c = -\frac{C_0.v}{m}$

This quadratic equation can then be solved using the **quadratic formula**:

$$C_f = \frac{-b \pm \sqrt{b^2 - 4ac}}{2a}$$

Substitute values:

Given: q_{max} = 381.24 mg/g

K_L = 0.012 L/mg

C_0 = 0.54 mg/L

V = 107,798,544,000 L

m = 0.5 g/L

Calculate C_f

Positive Root: $C_f = \frac{-0.66+\sqrt{43.16}}{0.048}$

$$C_f = 0.16 \text{ mg/L}$$

2.4 Calculation of phosphate recovery:

Recovery efficiency (R%):

$$R\% = \frac{C_0 - C_f}{C_0} \text{x } 100$$

$$R\% = \frac{0.54 - 0.16}{0.54} \text{x } 100$$

$$R\% = 69.54\ \%$$

Total PO_4^{3-} recovered for the entire pond:

$$PO_4^{3-} - \text{Recovered (kg)} = \text{Total } PO_4^{3-}\ \text{(kg)} \times \frac{R\%}{100}$$

$$PO_4^{3-} - \text{Recovered (kg)} = 58{,}211 \times \frac{69.54}{100}$$

$$PO_4^{3-} - \text{Recovered (kg)} = 40{,}479\ \text{kg}$$

This case study on PO_4^{3-} recovery from a shrimp pond in Southern Thailand obtained a PO_4^{3-} recovery efficiency (R%) of 69.54%. The technique achieved a total PO_4^{3-} recovery of 40,479 kg, resulting in a notable recovery in PO_4^{3-} in the pond water. This recovery also enabled nutrient recycling, as the recovered PO_4^{3-} can be utilized for agricultural applications. The successful implementation of this recovery technique highlights the potential for sustainable practices in shrimp aquaculture, providing both environmental and economic benefits.

3.7 Chapter summary

This study investigated the adsorption performance of PO_4^{3-} from aqueous solution using shrimp shell-derived adsorbents (SSs). Increasing pyrolysis temperature and activating with $Ca(OH)_2$ addition can improve the adsorption capacity of SSs (q_{max} = 381.24 mg/g). The SSs fitted to the pseudo-second order, and Langmuir models, suggesting the adsorption process is predominantly driven by a chemical reaction. The adsorption mechanism for PO_4^{3-} removal was dominated by chemical precipitation between Ca and P, forming stable Ca-P groups in the adsorbent. Ca^{2+} could be released from hydroxylellestadite (HDL), $Ca(OH)_2$, and $Ca(CO)_3$. Ligand exchange and anion–π interactions also contributed to PO_4^{3-} adsorption, especially in adsorption with SSsCA. Additionally, PO_4^{3-} recovery from the shrimp pond in Southern Thailand was effectively calculated utilizing the Langmuir isotherm and experimental data. The evaluation revealed that a PO_4^{3-} recovery ratio (R%) of 69.54% is possible the recovery of approximately 40,479 kg of $PO_4^{3-}$from the pond water, reflecting a significant decrease of excess PO_4^{3-}. This study provides a sustainable alternative for handling shrimp shell waste and suggests a promising approach for PO_4^{3-} recovery, thereby contributing to a circular system in shrimp aquaculture.

Chapter 4 Methyl orange removal

4.1 Background

Apart from high nutrient contamination in shrimp pond wastewater, the extensive utilization of various organic chemicals, including antibiotics (Sulfonamides), and pesticides (Organophosphates), further water pollution, posing significant risks to both ecological and human health [33]. Therefore, addressing wastewater treatment is also critical challenges in the recent shrimp aquaculture.

The SSs presented the great removal efficiency for PO_4^{3-} as demonstrated in **Chapter 3**. The presence of hydroxylellestadite (HDL) in all SSs samples could release Ca^{2+}, suggesting a Ca-induced precipitation phenomenon, implying that SSs is a suitable material for the removal of anionic pollutants. Besides, scientific researches on shrimp shell-derived adsorbents have mainly focused on the removal of heavy metals and cationic pollutants while a limited number of articles have been published on the removal of anionic pollutants as listed in **Chapter 1; Table 1.4**. Therefore, in this chapter, the SSs were applied for anionic pollutant removal, with methyl orange (MO) dye selected as a model anionic pollutant. MO is a sulfonated anionic azo dye, of which two benzene rings linked by an azo group (N = N), and it has high stability, resistance to degradation, and ease of measurement [170]. MO, thus, is capable of representing pollutants in shrimp shell wastewater. Investigations on adsorption kinetics, isotherms and thermodynamic were carried out. Removal mechanism and desorption experiment was also studied in this chapter.

4.2 Methyl orange adsorption experiment

The MO adsorption experiments were conducted using SSs prepared through pyrolysis alone at 700 °C (SSsN) and compared with two alkali modification methods: $Ca(OH)_2$ (SSsCA) and KOH (SSsK). KOH alkali activation was included in this study based on previous findings, which showed that chitosan-based biochar with KOH activation achieved an excellent MO adsorption capacity of 755.08 mg/g [3].

For the adsorption experiment, 100 mg SSs was added into 200 mL MO solution at different concentrations from 50 to 3500 mg/L. The mixture was stirred for 72 h (600 rpm/min, 20 °C), and collected at different time intervals. The pH of the working solutions varied between 8 and 9, indicating the basicity. The collected samples were then centrifuged to separate SSs particles. The residual MO solution was analyzed spectrophotometrically with

UV-VIS spectrophotometer (UV-2550, Shimadzu, Japan) at a wavelength of 465 nm. MO adsorption capacity of SSs (q_e) was determined from the following Equation **4.1**.

$$q_e = \frac{(C_0 - C_t)}{m} V \qquad \textbf{(4.1)}$$

where C_0 and C_t represent the initial and the residual MO concentration (mg/L), respectively, V is volume of the solution (L) and m represents the weight of the adsorbent (g).

4.3 MO removal performance

4.3.1 Comparison of adsorption performances

The adsorption performances of each SSs were compared based on the MO adsorption capacity (q_e) at a concentration of 1000 mg/L. The contact time was varied from 0 min to 72 h (4320 mins) as illustrated in **Figure 4.1a, 4.1b, and Table 4.1**.

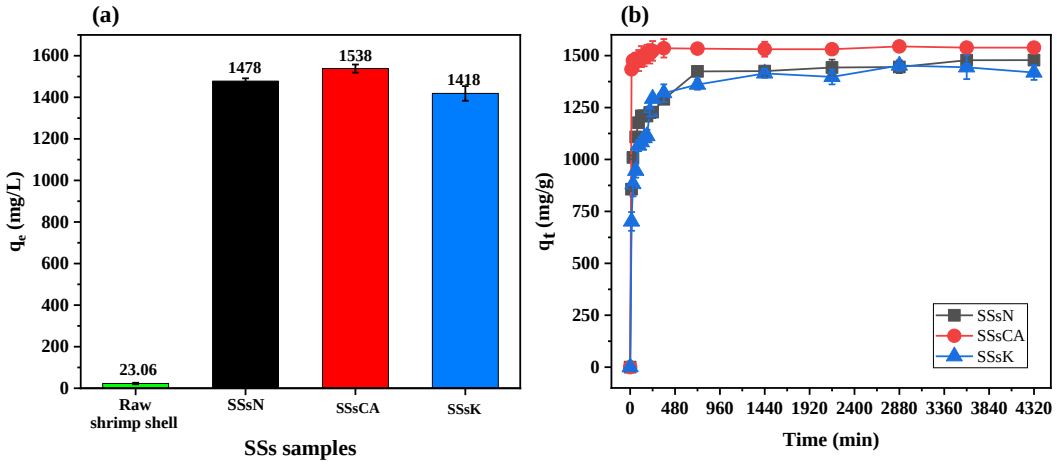

Figure 4.1 Adsorption data of MO onto SSs (a) Comparison of q_e, and (b) Influence of contact time on MO removal by each SSs.

The figure shows that the raw shrimp shells performed poorly. After modification, all SSs showed rapid adsorption in the first 2 h, and then gradually reached equilibrium within 24 h (1440 min) (see **Figure 4.1**). This observation might result from the increased availability of adsorption sites in or around the SSs for interaction with anionic MO present at first contact. The number of unoccupied active sites decreased over time, resulting in a gradual adsorption rate. However, each SSs displayed different adsorption capacities. As demonstrated from **Figure 4.1**, SSsCA had the highest adsorption capacity (q_e) of 1538 mg/g for MO adsorption, compared to 1478 mg/g for SSsN and 1419 mg/g for SSsK. The XPS and FTIR results also confirmed MO adsorption onto SSs (see **Figure 4.8 and 4.9**). A new XPS peak

associated with sulfonate ($-SO_3^-$) groups from MO was observed after adsorption (see Fig. 2f). Similarly, the FT-IR spectra revealed new peaks at 3900 and 3600 cm^{-1} (-OH and $-NH_2$ stretching vibrations), 1700 cm^{-1} ($-NH_2$), and 1032 cm^{-1} (-S=O-), demonstrating the presence of functional groups from the MO molecule [171, 172].

Table 4.1 Experimental data and standard errors of MO adsorption (1000 mg/L) capacity for each SSs as a function of time.

Time (min)	MO adsorbed onto each SSs in solution, q_t (mg/g)					
	SSsN		SSsCA		SSsK	
	qt (mg/g)	Standard deviation	qt (mg/g)	Standard deviation	qt (mg/g)	Standard deviation
0	0.00	0.00	0.00	0.00	0.00	0.00
15	856.91	9.61	1433.97	23.41	701.51	44.95
30	1009.93	8.88	1476.01	27.33	882.03	59.68
60	1108.35	8.80	1484.50	29.42	945.84	33.03
90	1176.59	3.79	1476.43	50.62	1067.17	27.20
120	1210.09	8.45	1495.12	50.32	1083.12	20.81
150	1210.09	6.12	1490.02	41.19	1102.85	18.91
180	1208.85	9.31	1512.53	39.48	1112.93	29.87
210	1225.81	9.62	1508.70	46.74	1230.48	24.29
240	1227.87	2.75	1522.72	47.28	1292.61	18.22
360	1289.50	5.01	1535.46	44.54	1319.48	41.91
720	1423.90	18.40	1533.76	8.83	1360.20	24.50
1440	1478.08	13.30	1538.43	19.50	1418.56	35.32
2160	1442.51	38.05	1530.79	16.23	1397.57	36.17
2880	1445.00	29.11	1544.37	13.26	1452.14	25.28
3600	1477.67	6.59	1538.43	19.50	1443.74	56.97
4320	1425.14	23.62	1530.79	35.95	1414.36	21.38

4.3.2 Adsorption kinetics

To analyze the kinetic mechanism of adsorption process, the experimental data was fitted with the pseudo-first order (PFO), pseudo-second order (PSO), and Elovich models at an initial MO concentration of 1000 mg/L. Adsorption kinetics is crucial to understanding the rate-determining steps and dominant mechanisms involved in the adsorption process [173]. The PFO model describes adsorption where the rate of site occupation is directly proportional to unoccupied sites, reflecting physisorption. The PSO model assumes the rate is proportional to the square of unoccupied sites, suggesting chemisorption as the rate-limiting step [144]. Additionally, the Elovich equation is employed to describe adsorption behavior characteristic of chemisorption with heterogeneous active sites [145]. The corresponding equations are shown in **Table 4.2**.

Table 4.2 Adsorption kinetics models [146, 147].

Equation	Non-linear form	Parameter
Pseudo-first order	$q_t = q_e(1 - e^{-k_1 t})$	k_1: the pseudo-first order kinetic rate constant (min^{-1})
Pseudo-second order	$q_t = \frac{q_e^2 k_2 t}{1 + q_e k_2 t}$	k_2: the pseudo-second order kinetic rate constant (g/mg.min)
Elovich	$q_t = \frac{1}{\beta}\ln(1 + \alpha\beta t)$	α: the adsorption rate (mg/g.min) β: the desorption constant (g/mg)

The results of MO adsorption kinetics are shown in **Figure 4.2** and **Table 4.**3. All regression coefficients (r^2) of PSO model (r^2 = 0.958-0.998) were higher than those of PFO model (r^2 = 0.890-0.996), and the experimental $q_{e,\,exp}$ values were very close to the predicted $q_{e,\,cal}$ values of the PSO model, suggesting that MO adsorption was dominated by chemisorption rather than physisorption [174]. In addition, the Elovich model can also better describe the adsorption behavior of all SSs to MO (r^2 = 0.966-0.987). This indicates the existence of chemisorption on heterogenous surfaces (see **Figure 4.2**).

Table 4.3 Adsorption kinetic parameters at 20 °C.

Adsorption parameters	SSs samples		
	SSsN	**SSsCA**	**SSsK**
q_e, exp mg/g)	1478	1538	1419
PFO			
k_1 (min^{-1})	0.055	0.192	0.044
q_e, cal (mg/g)	1317	1515	1287
r^2	0.890	0.996	0.996
PSO			
k_2 (g/mg.min)	$9.10x10^{-4}$	$5.94x10^{-4}$	$3.85x10^{-5}$
q_e, cal (mg/g)	1391	1526	1379
r^2	0.960	0.998	0.958
Elovich			
α (mg/g.min)	$9.4x10^{4}$	$2.04x10^{9}$	$6.3x10^{3}$
β (g/mg)	0.009	0.062	0.008
r^2	0.987	0.999	0.966

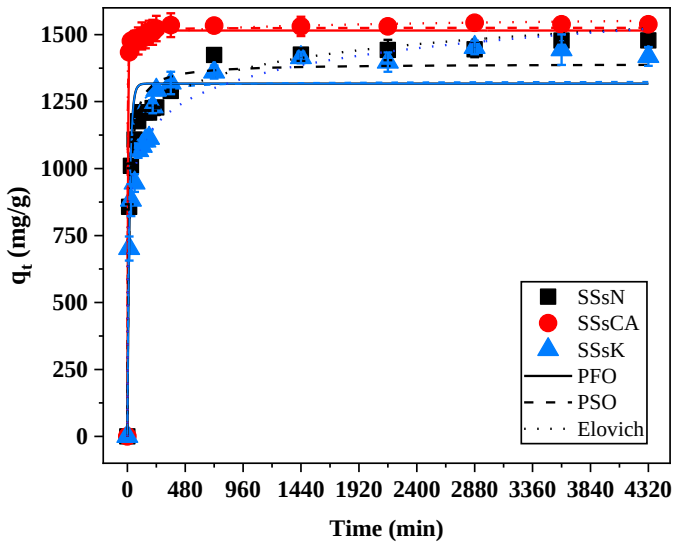

Figure 4.2 Adsorption kinetics of MO adsorption by SSs.

4.3.3 Adsorption Isotherm

Adsorption isotherm is the equilibrium relationship between adsorbent and adsorbate. The isotherm study provides crucial information on the maximum adsorption capacity and adsorption characteristics [152]. In this work, the obtained adsorption data were fitted with Langmuir, Freundlich and Sips isotherms by varying the initial MO concentrations (50, 200, 500, 1000, 2000 and 3550 mg/L). The Langmuir model assumes monolayer adsorption on a homogeneous surface, while the Freundlich model considers adsorption on a heterogeneous surface. The Sips model combines the Langmuir and Freundlich isotherm models, effectively predicting adsorption in both homogeneous and heterogeneous systems [175, 176]. The non-linear isotherm equations are shown in **Table 4.4**.

Table 4.4 Adsorption isotherms models [146, 147].

Equation	Non-linear form	Parameter
Langmuir	$q_e = \frac{q_{max} k_L C_e}{1 + k_L C_e}$	k_L: the Langmuir adsorption constant (L/mg)
Freundlich	$q_e = k_F . C_e^{1/n}$	k_F: the Freundlich constant (mg/g)(L/mg)$^{1/n}$)) n: the adsorption intensity constant
Sips	$q_e = \frac{q_{max} . k_s c_e^n}{(1 + k_s c_e^n)}$	k_s: the Sips constant (L/mg) n: the Sips model exponent

The Langmuir and Freundlich isotherm models were also used to fit the adsorption equilibrium data (see **Figure 4.3**). The MO adsorption process of SSs agreed with the Langmuir model better (r^2 = 0.938-0.986) than the Freundlich model (r^2 = 0.914-0.938) (see **Table 4.5**). However, the Langmuir model assumes monolayer adsorption on a homogeneous surface, where there are no interactions between adsorbed molecules (physisorption) [144]. In contrast, the kinetic results indicated chemisorption on heterogeneous surfaces. The 1/n values of Freundlich model were also below 1 for all SSs (see **Table 4.5**), indicating the heterogenous surface through multilayer adsorption [175, 177]. Therefore, the complexity of the MO adsorption process may not be fully interpreted by the Langmuir model alone. The Sips model can provide a more comprehensive understanding of adsorption behavior in the MO adsorption. It overcomes the limitations of the Freundlich model at higher concentration, accurately describing adsorption across a wide range of concentrations [175, 176]. The highest r^2 values

(r^2 = 0.973-0.991) were also obtained with the sips model (see **Figure 4.3 and Table 4.5**). The n parameter was higher than 1, confirming the surface heterogeneity of the adsorbent (see Table 2). This suggests that MO adsorption onto SSs likely occurs through a combination of monolayer and multilayer adsorption pathways [175]. This is consistent with the previous studies, which highlighted that MO adsorption occurs on other adsorbent materials, including water hyacinth biochar [178], and activated carbon [179, 180].

Table 4.5 Adsorption kinetic parameters.

Adsorption parameters	**SSs samples**		
	SSsN	**SSsCA**	**SSsK**
Langmuir isotherm			
k_L (L/mg)	0.0030	0.0020	0.034
q_L (mg/g)	4063	4772	2363
r^2	0.986	0.985	0.969
Freundlich isotherm			
k_F (mg/g)(L/ mg)$^{1/n}$)	137.1	55.38	119.2
n	2.33	1.81	2.70
r^2	0.914	0.939	0.789
Sips isotherm			
k_s (L/mg)	0.008	0.013	0.015
q_s (mg/g)	3876	4033	2183
n	1.78	4.12	2.15
r^2	0.988	0.991	0.993

Additionally, **Table 4.5** exhibited that the maximum adsorption capacity of the Sips model (q_s) was higher for SSsCA (4033 mg/g) than for SSsN (3876 mg/g) and SSsK (2183 mg/g). A higher MO adsorption capacity is expected for adsorbents with a higher surface area since more active sites are available for adsorption [181, 182]. However, the q_s of SSs are indirectly proportional to both the S_{BET} and the external surface area with a low correlation coefficient (r^2 = 0.209-0.789) (see Fig. 3d). Chemisorption is likely more predominant than physisorption, which aligns with the kinetic and isotherm results.

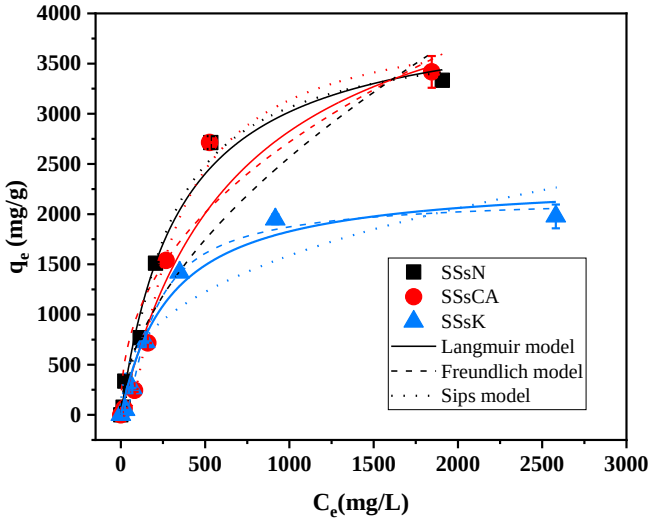

Figure 4.3 Adsorption isotherm of MO by using SSs with different modification.

The maximum adsorption capacity value found in this work was higher than previous studies (see **Table 4.6**). The excellent performance of SSs for MO adsorption can be governed by two parts: (1) MO properties and (2) SSs structure. The detailed mechanism would be discussed more in the section 4.3.2. SSsN and SSsCA included HDL, which plays essential role for MO adsorption. HDL has unembeds calcium silicate hydrate (CSH) [108, 109], potentially releasing Ca^{2+} and exposing silanol-like surface properties on SSs particles for MO adsorption. In contrast, the moderate MO adsorption of SSsK likely occurs via different adsorption mechanism compared to SSsN and SSsCA, as evidenced by the significant presence of K_2CO_3 and K2O, along with the the limited formation of HDL in SSsK. The K_2CO_3 in MO aqueous solution possibly decompose to K_2O, leading K^+ generation for MO adsorption [183], as an evidenced by the appearance and intensity reduction of K1S in the XPS results of SSsK (**Figure 4.4**). Obviously, SSsCa had the highest adsorption capacity for MO (see **Table 4.5**). Furthermore, though physisorption is not the main mechanism, the lower surface area of SSsK might affect its adsorption performance. KOH activation destroyed the pore structure and adsorption sites, as shown by lower external surface area and smaller total pore volume than those of SSsN and SSsCa (see **Chapter 2: Table 2.1**), thereby decreasing the available adsorptive sites for MO. Because SSsCA had the highest adsorption capacity for MO (see **Table 4.5**), it was selected for adsorption thermodynamics analysis in the next section.

Table 4.6 Comparison of the adsorption performances of MO with other reported biochars.

Adsorbent	q_{max} (mg/g)	q_{max} determination	Ref.
Protonated amine-modified hydrochar	909.09	Langmuir	[184]
Biochar from cellulose	306.13	Temkin	[183]
Activated biochar from pomelo peel waste	163.11	Langmuir	[185]
Chitosan-modified biochar	38.75	Langmuir	[186]
SSsCA	4033	Slips	This work
SSsN	3876	Slips	This work
SSsK	2183	Slips	This work

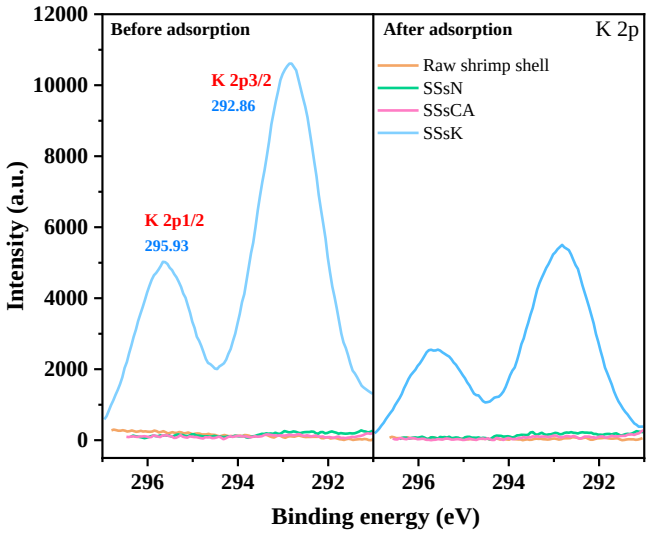

Figure 4.4 K 2p XPS spectra of SSs before and after MO adsorption.

4.4 Adsorption thermodynamics

Three thermodynamic parameters, including changes in the Gibbs free energy (ΔG°), enthalpy (ΔH°), and entropy (ΔS°), were calculated at different temperatures (20, 35, and 45 °C) to examine the feasibility and nature of the adsorption process. The values of ΔH° and ΔS° can be evaluated using the Van't Hoff equation as follows (See **Equation 4.2)**:

$$\ln k_s = \frac{\Delta H^\circ}{RT} - \frac{\Delta S^\circ}{R} \quad \textbf{(4.2)}$$

where k_s (L/mg) is the residual MO adsorption distribution coefficient, R is the universal gas constant (8.314 J/mol/K), and T is the absolute temperature (K). The slope and intercept of the linear plot of $\ln k_s$ *vs.* 1/*T* were used to calculate the ΔH° and ΔS°, thereafter, ΔG° can be derived according to the following **Equation 4.3**:

$$\Delta G^\circ = \Delta H^\circ - T\Delta S^\circ \quad \textbf{(4.3)}$$

The thermodynamic parameters of MO adsorption onto SSsCA are presented in **Figure 4.5 and Table 4.7.** The positive value of ΔH° confirmed the endothermic adsorption according to the larger MO adsorption capacity at higher temperature. The ΔH° value also indicates the type of adsorption. The ΔH° for physisorption is 2.1–20.9 kJ/mol, while chemisorption is in a range of 40-120 kJ mol kJ/mol [187, 188]. In this study, the ΔH° of 33.97 kJ/mol suggested that MO adsorption onto SSsCA was driven by physicochemical sorption. Alijani et al. [187] similarly proposed dual adsorption mechanisms for mercury (II) adsorption on multi-walled carbon nanotubes, with ΔH° values of 24.74–28.75 kJ/mol. These also did not clearly fall within the typical ranges for either physisorption or chemisorption. Meanwhile, the positive value of ΔS° indicated an increase in randomness (or disorder) of the capture process at the adsorbent-solution interface during MO adsorption [189]. The positive ΔG° values suggested non-spontaneous adsorption onto SSsCA. The decrease in values of the ΔG° with an increase in temperature indicates more spontaneous at high temperature.

The endothermic nature of the adsorption process is driven by interactions that become more favorable at higher temperatures. At high temperatures, the enhanced mobility and diffusion of MO molecules facilitate their movement toward the adsorbent surface. Simultaneously, the swelling effect within the internal structure of adsorbent expands the pores, allowing pollutants to penetrate deeper into the material [190, 191]. This combination of factors enhances the overall adsorption capacity at higher temperatures.

Table 4.7 Thermodynamic parameters.

T (°C)	ln(k_s) (L/g)	ΔH° (KJ/mol)	ΔS° (J/mol.k)	ΔG° (KJ/mol)
20	-4.347			10.82
35	-3.990	33.97	78.98	9.63
45	-3.196			8.84

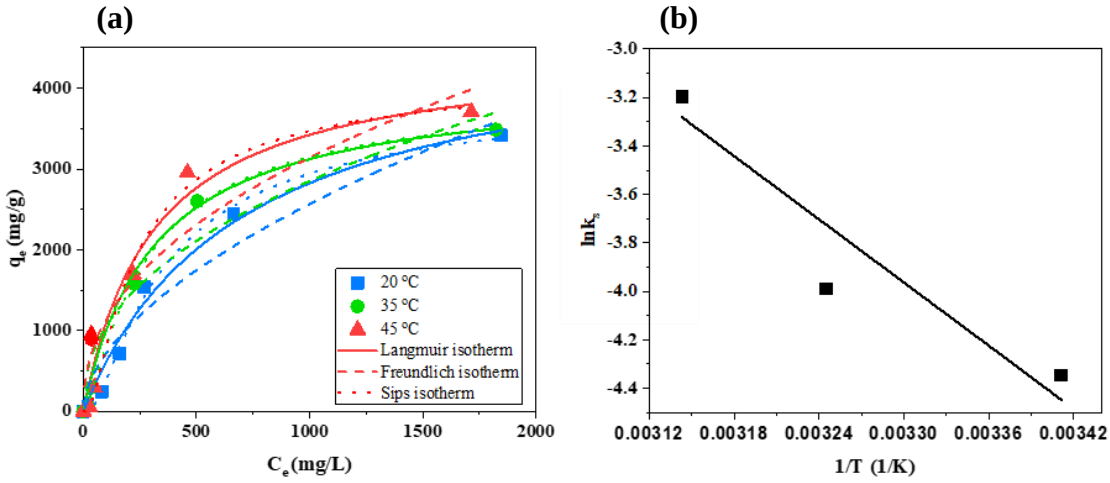

Figure 4.5 Adsorption thermodynamic of MO by using SSs with different modification (a) Isotherm plots for the MO adsorption onto SSsCA at different temperatures, and (b) Thermodynamic parameters fitted by the van't Hoff equation of SSsCA.

4.5 MO desorption

Desorption studies can provide insights into the adsorption mechanism. In this study, two SSsCA samples adsorbed at different initial concentrations of MO—100 mg/L (low concentration) and 1000 mg/L (high concentration)—were selected to desorb MO molecules. The desorption experiment was conducted when the above-mentioned adsorption process was completed. The adsorbent was rinsed with distilled water to eliminate unabsorbed MO, and then dried in the oven at 100 °C for 24 h. After that, 50 mg MO-loaded adsorbent (100 mg/L and 1000 mg/L) was added into 100 mL of deionized water at pH = 2 and 9 and kept stirring until equilibrium was reached. The adsorbent was separated, and the concentration of released MO in the solution was measured using the same procedure.

As shown in **Figure 4.6**, nearly complete desorption from the samples adsorbed at 100 mg/L (low concentration) was observed (reversible adsorption), regardless of pH. When pH is decreased to 2, the reduced electrostatic repulsion between MO and the SSs surface should enhance desorption efficiency. However, the results indicated lower efficiency. This suggests that the existing electrostatic repulsion acts as a significant driving force for MO release, and this weakened repulsion still facilitates MO retention on the surface. Meanwhile, the samples adsorbed at 1000 mg/L (high concentration) showed significantly low desorption efficiency (irreversible adsorption). This indicates the different adsorption mechanisms between low and high MO concentrations, and the stronger interaction between SSsCA and MO observed at

high MO concentration. These detailed mechanisms of adsorption would be discussed further in the following section.

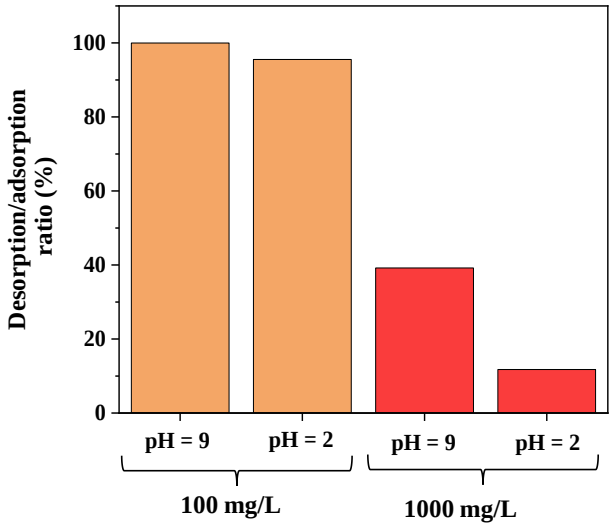

Figure 4.6 MO desorption/adsorption ratio by SSsCA at different concentration (100 and 1000 mg/L) and pH (2 and 9).

4.6 Adsorption mechanisms

The findings of this study raise crucial questions about MO adsorption onto SSs and they would be discussed in this section. Because SSsCA exhibited the highest adsorption performance, the detailed mechanism of MO adsorption was explained focusing on SSsCA. In the MO aqueous solution at pH = 9, SSsCA has a negative surface charge on its surface (see **Chapter 2: Figure 2.4**). Therefore, anionic MO is expected not to easily reach to the adsorption site owing to electrostatic repulsion. However, some of MO molecules can move more actively at higher temperature. This allowed active MO to pass over the electrostatically repulsive barrier and reach the outer surface of SSsCA. The MO molecules were first adsorbed onto the active sites of the external SSsCA, followed by gradual transfer into inner pores MO interparticle diffusion is accelerated, allowing it to penetrate deeper into the pores, while the internal structure of SSs expands. Overall, higher MO adsorption is achieved at higher temperature, which looks the endothermic adsorption of MO onto SSsCA. Moreover, SSs exhibit excellent performance in anionic MO adsorption despite the electrostatic repulsion caused by their negative surface charge. Most importantly, the MO adsorption onto SSs shows dual characteristics, involving both reversible and irreversible adsorption processes, which will be explained as follows:

4.6.1 The large adsorption capacity of SSs for anionic MO

The large adsorption capacity of SSs for anionic MO, despite the negative surface charge of SSs, raises a challenging question. This study proposes that the excellent performance of SSs for MO adsorption can be governed by two parts: (1) the nature of MO molecules and (2) the structure of SSs. MO molecules have the ability to exhibit the self-aggregation behavior when the initial concentration is above 100 mg/L. MO dye molecules tend to form more dimers (non-single molecules) at higher concentration [192]. Once MO molecules occupied the adsorption sites on SSs, the adsorption capacity decreased. However, the interactions between MO molecules continued agglomerate, resulting in multilayer adsorption that ultimately increases the overall adsorption capacity.

Meanwhile, SSsN and SSsCA included HDL, which plays essential role for MO adsorption. HDL has agglomerates of compact crystals in hexagonal prism morphology which unembeds calcium silicate hydrate (CSH) [108, 109]. The MO adsorption at pH=9 could release Ca^{2+} and expose silanol-like surface properties from the SSs particles, which might provide the active sites for MO adsorption onto the SSs surface [110]. The released Ca^{2+} inside HDL might form a complex with SO_3^- of MO molecule, which is supported by the decrease of Ca 2s intensity (see **Figure 4.7a**) and the new peak appearance of sulfonate functional groups (see **Figure 4.7b**) after adsorption. The FT-IR results also indicate the new peak at 1032 cm^{-1} (see **Figure 4.8**), which demonstrates the involvement of -S=O- of MO molecule [193, 194]. Meanwhile, the Si of silanol-like surface of HDL might form a complex with azo group N of MO molecule, which was evidenced by the new peak appearance of Si–N linkage after adsorption (see **Figure 4.7c**). A loan electron pair of azo group N of MO interacts with Si of silanol to form hydrogen bonding between silanol and the π-system of azo group [195].

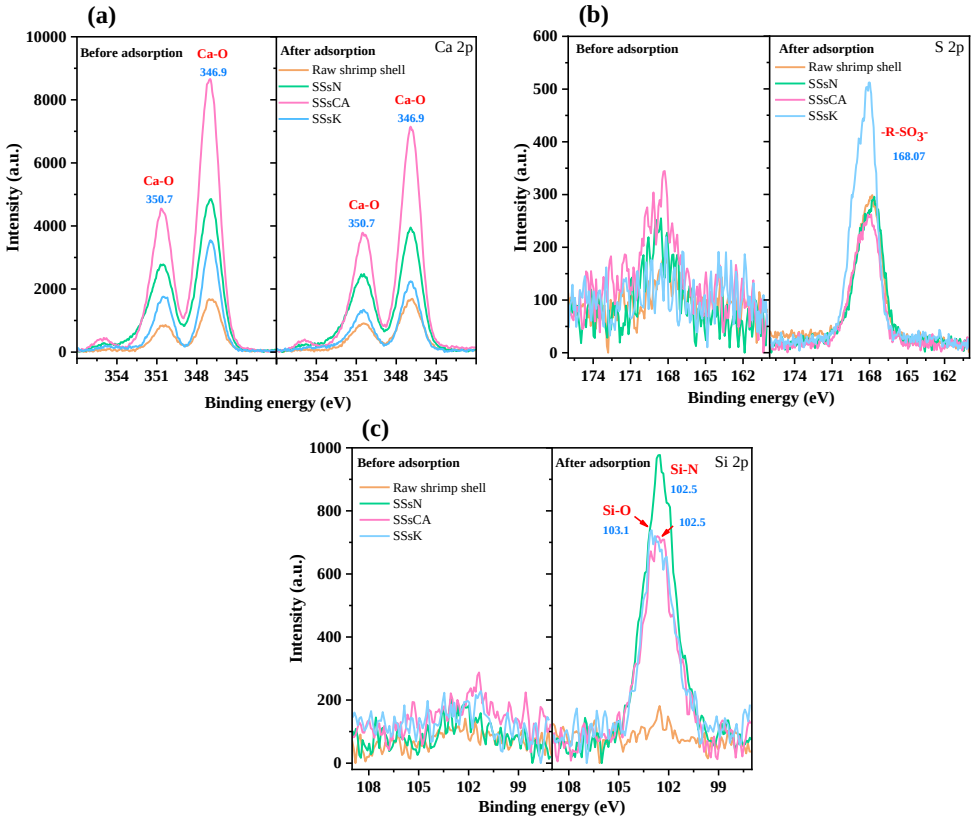

Figure 4.7 XPS spectra of SSs before and after MO adsorption (a) Ca 2p, (b) S 2p, and (c) Si 2p.

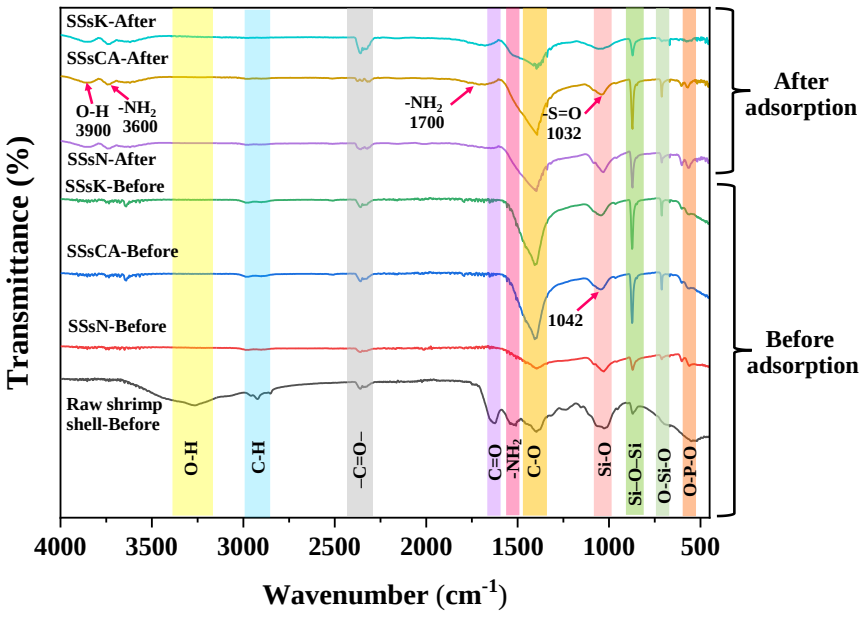

Figure 4.8 FTIR spectra of each SSs before and after MO adsorption.

Additionally, when reviewing previous literature, it is commonly observed that MO dye tends to self- aggregate, in aqueous solutions. There is still a noticeable presence of high adsorption capacity due to the intermolecular interactions in MO, such as the π–π interactions between the aromatic rings and the –N = N– groups within the dye molecule. Hence, the surface of adsorbent may accommodate more than one layer of molecules and not all adsorbed molecules are in contact with the surface of SSs [196, 197].

On the other hand, since MO molecule would be adsorbed mainly on the external surface because of large and complicated structure of MO molecule [181, 182]. After the aggregation of MO, aggregated MO was deposited or adsorbed on the outer surface of SSs. The maximum MO adsorption capacity (q_{max}) of SSs is in the good linearity to the external surface area rather than S_{BET} (see **Figure 4.9**). SSsCA exhibited the highest adsorption capacity (4033 mg/g) with the large external surface areas (13.29 m^2/g). Although the fit was relatively good, it was not perfect. This suggested that external surface area alone cannot fully explain the adsorption capacity. The degree of MO aggregation may also play a significant role in influencing the adsorption capacity. In addition, volume expansion was observed after adsorption on SSs at 1000 mg/L MO, which could be a result of MO aggregation (see **Figure 4.10).** Therefore, this helps explain the large adsorption capacity observed. Moreover, the adsorption performance of MO is closely linked to the external surface area of the adsorbent, which suggests that the rate-limiting step in this process is the mass transfer of MO from the bulk solution to the adsorbent surface. Since the diffusion within the pores seems less important, the process is controlled by how quickly MO molecules can move to the surface, where they interact with the adsorbent.

However, since this study focused on adsorption performance rather than the exact pre-adsorption state of the adsorbate, this remains a limitation. Two possible scenarios can be considered for the MO adsorption process. In the first scenario, MO molecules may undergo aggregation in solution before adsorption, forming larger molecular clusters that then interact with the adsorbent surface. In the second scenario, individual MO molecules may first attach to the adsorbent surface, and aggregation occurs subsequently as more molecules accumulate. Distinguishing between these two pathways is challenging and would require additional analyses. Understanding this process in greater detail could provide deeper insights into the adsorption mechanism.

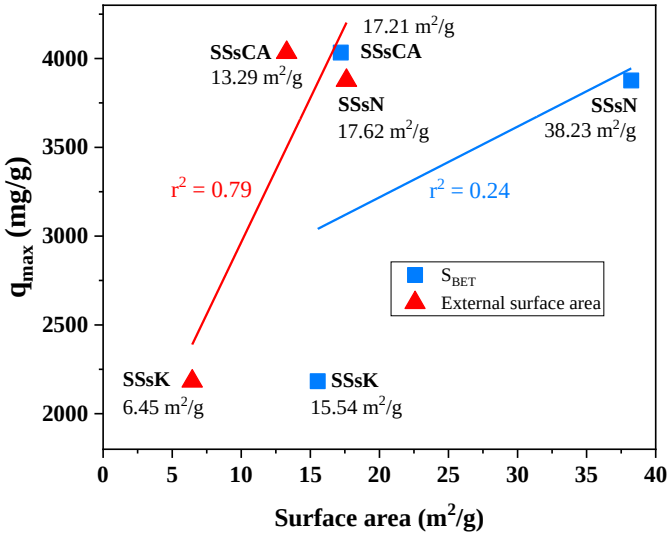

Figure 4.9 The relation between q_{max} and S_{BET} and external surface area.

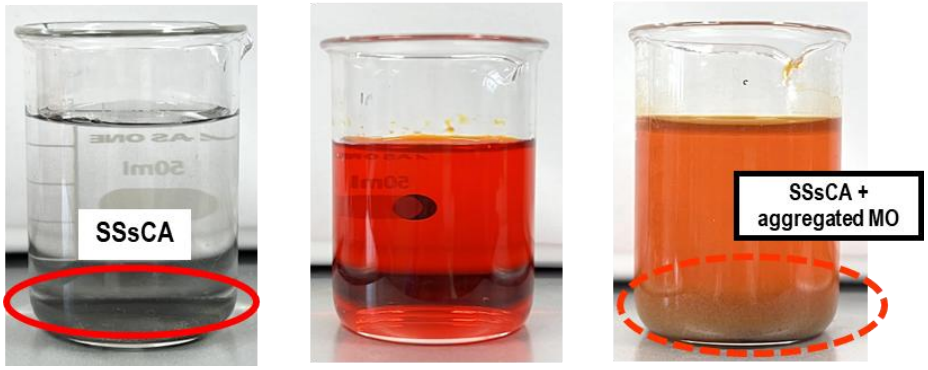

Figure 4.10 Adsorption kinetics of MO adsorption (1000 mg/L) by SSsCA.

Moreover, we found a previous study related to calcium-rich biochar with high removal efficiency, similar to the results in this work. Dai et al. (2018) [198] investigated calcium-rich biochar derived from crab shells (CRB) for Congo Red (CR) adsorption. Crab shells belong to the same crustacean group as shrimp shells in this study. CR is an anionic diazo dye with a larger structure than MO, which has one azo bond. CR was tested at concentrations up to 4000 mg/L, similar to the conditions in our study. The result demonstrated a superb adsorption capacity of 20,317 mg/g for CR (See **Table 1.2**). The study also highlighted the importance of Ca as a key factor in enhancing adsorption, which is consistent in this study. Although the study did not address the self-aggregation behavior of CR, it is known that CR can form larger

aggregates in solution due to π-π interactions between the aromatic rings of the dye [199]. This might be related to the high adsorption capacity observed in their work.

A previous study by Ahmed et al. (2018) [200] also reported a superb removal capacity for MO, with an adsorption capacity of 4483.9 mg/g. The hierarchically porous magnesium oxide (MgO) adsorbent was prepared using a method involving a precipitating agent, such as magnesium sulfate ($MgSO_4$) and ammonia (NH_3). The concentration range for the test was up to 2000 mg/L, similar to our work (See **Table 4.8**). However, their study proposed a different adsorption mechanism, focusing on the macropore structure properties that facilitate MO adsorption by enabling efficient transport to surface sites and multilayer adsorption. Notably, this study did not discuss self-aggregation behavior. In contrast, our work highlights the role of HDL formation in the adsorption process, where MO self-aggregation helps to enhance adsorption performance.

Table 4.8 Comparison of adsorption characteristics

Parameter	SSsCA	CRB	MgO
Source Material	Shrimp Shells	Crab Shells	MgO
Preparation Method	$Ca(OH)_2$ + Pyrolysis at 700°C for 1 h	Pyrolysis at 800°C for 2 h	$MgSO_4$ + NH_3
Adsorbent loading (mg/L)	500	500	1000
Dye type	Methyl orange	Congo red	Methyl orange
Concentration Range Tested (mg/L)	50 -3500	350-4000	0.1-2000
Efficiency (mg/g)	4033	20317	4483
Ca content (%)	82.7	65.4	-
S_{BET} (m^2/g)	17.21	81.57	63
Average pore size (nm)	2.33	4.22	12.03
Mechanisms	Ca-precipitation, Si-N linkage	Ca-precipitation, electrostatic attraction, hydrogen bonding and π-π interaction	Macropore structure, and other chemical adsorption

4.6.2 Dual characteristics including both reversible and irreversible adsorption processes.

The nature of MO molecules at low (≤ 100 mg/L) and high (>100 mg/L) concentrations, along with the released Ca^{2+} and exposed silanol-like surface sites are also key elements in explaining reversible and irreversible adsorption. This study found that adsorption is reversible at low MO concentration, while it becomes irreversible at high concentration. At low initial MO concentration, most MO molecules are monomers [192, 201] and can be easily desorbed from the SSs surface due to a lack of connectivity [202]. Additionally, the MO monomer adsorption was mainly or partially driven by complex formation between azo group N of MO and Si of SSs. This type of adsorption is less stable than that in high concentration system, which involves both Si-N linkages and SO_3^-–Ca^{2+} complexes (see **Figure 4.7c**). At high initial MO concentration, the MO molecules also tend to form polymers [192, 201], leading to multilayer adsorption where MO polymers complex with SSs. The desorption of the entire polymer chain may require simultaneous desorption of all adsorbed MO monomers (see **Figure 4.11**) [202]. The adsorption becomes irreversible when a few monomers remain attached on the SSs surface.

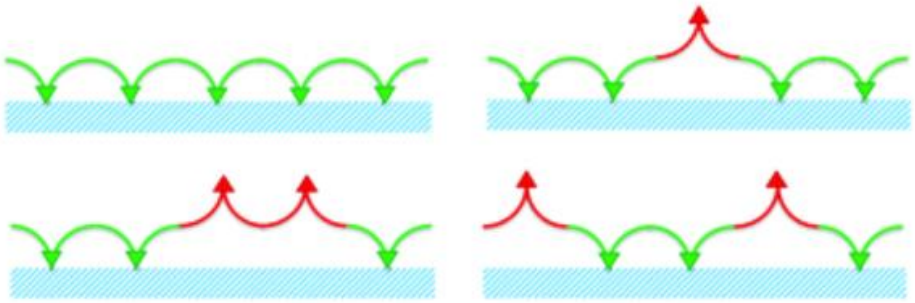

Figure 4.11 An illustration of the concept of irreversibility at high MO concentration system: while with time a monomer can be either adsorbed (green) or desorbed, desorption of the whole chain would require simultaneous desorption of all the adsorbed monomers [202].

4.7 Chapter Summary

This chapter focused on evaluating the ability of shrimp shell derived-adsorbent (SSs) to remove methyl orange (MO) dye as a model of anionic pollutant. Although SSs negative surface charge, the results indicated that all SSs could effectively adsorb MO dye effectively. In particular, SSsCA (fabricated by pyrolysis with $Ca(OH)_2$ modification) exhibited the best performance in terms of MO removal (q_{max}= 4033 mg/g).

The adsorption behavior of MO onto SSs is endothermic, primarily controlled by chemisorption, along with physisorption, as indicated by the kinetic, isotherm, and thermodynamic results. At high temperatures, the enhanced mobility and diffusion of MO molecules improve their movement toward the adsorbent surface, while the internal structure expands, allowing deeper penetration of SSs. The excellent MO adsorption was governed by hydroxylellestadite (HDL) inside SSs and the nature of MO molecules. The presence of HDL enabled SSs to demonstrate a large adsorption capacity by releasing Ca^{2+} and expose silanol-like surface properties for adsorbing anionic MO. MO adsorption is mainly driven by complex formation between azo group N of MO and Si of SSs. This study highlights the concentration-dependent nature of MO adsorption, which also influences its adsorption performance. The adsorption was reversible at low MO concentration (≤ 100 mg/L) because MO monomer (disconnecting MO). In contrast, it became irreversible at high concentration (>100 mg/L). MO formed polymer complex, leading to multilayer adsorption where MO polymers complex with SSs through both Si-N linkages and Ca^{2+} -SO_3^- complexes. Overall, this study highlights the importance of initial material concentration dependency of MO adsorption. Furthermore, since SSs exhibited excellent performance for MO adsorption, the removal of other anionic pollutants from shrimp aquaculture wastewater by using SSs might be feasible.

Chapter 5 Conclusion and recommendations

5.1 Overall conclusions

This thesis aims to efficiently utilize shrimp shell waste for the removal of anionic water contaminants by converting it into biochar-derived adsorbents. The adsorbents obtained from shrimp shells (SSs) were synthesized from shrimp shell waste via pyrolysis and alkali activation employing calcium hydroxide ($Ca(OH)_2$) and potassium hydroxide (KOH). Four formulations were developed and designated as SSsN (pyrolysis at 700 °C), SSsH (pyrolysis at 800 °C), SSsCA ($Ca(OH)_2$ + pyrolysis at 700 °C), and SSsK (KOH + pyrolysis at 700 °C). All SS samples were characterized to examine their physicochemical properties, as described in **Chapter 2**. The adsorbents were subsequently applied for wastewater treatment for removing phosphate (PO_4^{3-}) and methyl orange dye (MO) as representative anionic contaminants, as detailed in **Chapters 3 and 4,** respectively.

In **Chapter 2**: *Fabrication and characterization of the shrimp shell derived-adsorbent,* shrimp shell-derived adsorbent (SSs) were fabricated from shrimp shell waste through a pyrolysis process and alkali activation using calcium hydroxide ($Ca(OH)_2$) and potassium hydroxide (KOH). SSs demonstrated significant improvements in both physical and chemical characteristics, compared to raw shrimp shell. All samples exhibited enhanced surface area (S_{BET}) and pore volume (V_{pore}), with higher pyrolysis temperatures (800 °C) resulting in more significant enhancements than differing alkali activators. Shrimp shells are rich in Ca, which is distributed throughout the surface, as confirmed by EDS analysis, resulting in the formation of hydroxylellestadite (HDL), calcium carbonate ($CaCO_3$), calcium hydroxide ($Ca(OH)_2$), and potassium sodium calcium chloride carbonate hydrate (KSC). Samples after pyrolysis at 700 °C (SSsN and SSsCA) exhibited HDL and $CaCO_3$, whereas KOH-activated sample (SSsK) generated KSC. At 800 °C (SSsH), $CaCO_3$ converted into $Ca(OH)_2$. The formations, validated by XRD, FTIR, and XPS, may affect the adsorption of PO_4^{3-} and MO, as elaborated in the following chapter.

In **Chapter 3:** *Phosphate Removal and Recovery,* SSs were investigated their removal performance for PO_4^{3-} removal and recovery from solution. All SSs samples (SSsN, SSsCA, and SSsK) demonstrated significant effectiveness in PO_4^{3-} adsorption, with SSsCA exhibiting the greatest adsorption selectivity. The adsorption mechanism for PO_4^{3-} removal was dominated by chemical precipitation between Ca and P, forming stable Ca-P

groups in the adsorbent. Ca^{2+} could be released from HDL, $Ca(OH)_2$, and $Ca(CO)_3$. Ligand exchange and anion–π interactions also contributed to the PO_4^{3-} adsorption. The recovery ratio of PO_4^{3-} was determined through a case study in Southern Thailand, indicating a recovery efficiency (R%) of 69.54%, which corresponds to approximately 40,479 kg of PO_4^{3-} retrieved from pond water. This substantial decrease in an excess PO_4^{3-} represents a sustainable strategy for managing shrimp shell waste while offering an effective way of PO_4^{3-} recovery, thereby promoting the development of a circular system in shrimp aquaculture.

In **Chapter 4:** *Methyl orange removal*, SSsN, SSsCA, and SSsK were selected to remove methyl orange (MO) dye. As a results, SSsCA (q_{max}= 4033 mg/g) exhibited the best performance in terms of MO removal performance. The outstanding MO adsorption performance was attributed to the presence of HDL within SSs and the inherent characteristics of MO molecules. HDL facilitated a high adsorption capacity by releasing Ca^{2+} ions and providing silanol-like surface properties, which effectively captured the anionic MO through the formation of Si–N linkages and Ca^{2+}–SO_3^- complexes. This chapter also highlights the concentration-dependent nature of MO adsorption, which also influences its adsorption performance. The adsorption was reversible at low MO concentration (≤ 100 mg/L) because MO monomer (disconnecting MO). In contrast, at higher concentrations (>100 mg/L), the adsorption was irreversible due to the connectivity between polymeric complexes. The interactions between MO molecules continued agglomerate that ultimately increases the overall adsorption capacity. Due to the excellent MO adsorption performance of SSs, they could potentially be used to remove other anionic pollutants from shrimp aquaculture wastewater.

In conclusion, the SSs derived from shrimp shell waste has high potential to be used as an effective adsorbent for removing anionic water pollutants. The results demonstrated efficient PO_4^{3-} adsorption and significant MO removal, emphasizing its dual role in nutrient recovery and water purification. This "waste-to-wealth" approach, which transforms waste into valuable products, supports sustainability and a circular system in shrimp aquaculture.

5.2 Recommendations

This study demonstrates the excellent removal and recovery of phosphate (PO_4^{3-}) and anionic methyl orange (MO) dyes using a sustainable material derived from shrimp shell waste. Building on these findings, several key areas for future investigation are proposed.

1. Shrimp ponds also use seawater, not freshwater. Therefore, the adsorption

performance of SSs will likely differ in seawater. The study of PO_4^{3-} adsorption in seawater should be extended, as real shrimp ponds utilize seawater.

2. Since the majority of shrimp produced in Thailand are vannamei shrimp (whiteleg shrimp), which are cultured in both freshwater and seawater, this study specifically uses shrimp from seawater. Its findings may be directly applied to improve PO_4^{3-} recovery and nutrient recycling in vannamei shrimp farming systems.

3. In real shrimp pond wastewater, the mixture of various pollutants is present and impact the adsorption capacity of PO_4^{3-} and MO. The binary system experiment would provide more relevant insights for real-world applications. Future research should address this.

4. The potential leaching of Ca^{2+} and $CaOH^{+}$ from SSs after PO_4^{3-} adsorption should be investigated. While moderate levels of Ca^{2+} can enhance plant growth, excessive amounts or unfavorable pH conditions may adversely affect plant health.

5. The ability to utilize the recovered PO_4^{3-} as a fertilizer should be thoroughly evaluated, as it could offer significant benefits to the agricultural sector. Moreover, when using shrimp shell-derived adsorbents, they may adsorb various anionic pollutants. This means PO_4^{3-} and other pollutants could be adsorbed together. However, if we want to use the adsorbed PO_4^{3-} as a fertilizer, further treatment would be required to separate PO_4^{3-} from the other adsorbed pollutants. This separation will be an important focus for future research.

6. Scaling up the powdered adsorbent remains a significant challenge. The experiment used a magnetic stirrer to ensure uniform mixing of the adsorbent throughout the solution. However, in the initial proposed setup, aeration tanks were purposed (see **Figure 5.1**). The adsorption kinetics observed in the lab setup will differ from those in real applications within the aeration tank. The experiments were conducted under the simplest conditions to obtain baseline kinetic data, which are essential for developing a real adsorption model that can be applied in more complex conditions, such as those in the aeration tank. This aspect should be considered in the future work.

7. The detailed lifecycle assessment and economic analysis are crucial to evaluate the feasibility of scaling up the production and application of this adsorbent. As part of economic analysis. a simplified cost calculation approach is proposed in this work based on the electricity consumption for pyrolysis of waste wood as feedstock (0.5 kWh per kg of product produced) [203] (see **Appendix**). Other factors, such as equipment and maintenance costs, and waste disposal costs, must also be considered, as they significantly influence the overall cost estimate.

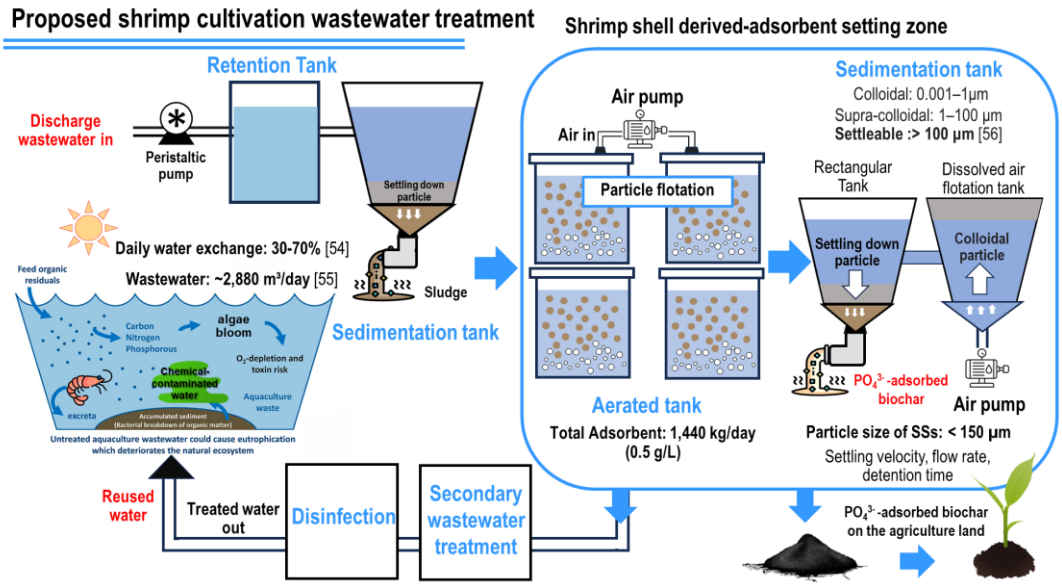

Figure 5.1 Proposed shrimp cultivation wastewater treatment.

5.3 List of Publications

Peer-Reviewed Journal Articles

1. Yamsomphong, K., Xu, H., Yang, P., Yotpanya, N., Yokoi, T., & Takahashi, F. (2025). *Transforming waste into wealth in sustainable shrimp aquaculture: Effective phosphate removal and recovery using shrimp shell-derived adsorbents.* Separation and Purification Technology, 357, 129982.

References

[1] R.-F. Chen, T. Liu, H.-W. Rong, H.-T. Zhong, C.-H. Wei, Effect of organic substances on nutrients recovery by struvite electrochemical precipitation from synthetic anaerobically treated swine wastewater, Membranes, 11 (2021) 594.

[2] M.Y. Jin, Q. Zhen, D. Xiao, G. Tao, X. Xing, P. Yu, C. Xu, Engineered non-covalent π interactions as key elements for chiral recognition, Nature Communications, 13 (2022) 3276.

[3] C. He, H. Lin, L. Dai, R. Qiu, Y. Tang, Y. Wang, P.-G. Duan, Y.S. Ok, Waste shrimp shell-derived hydrochar as an emergent material for methyl orange removal in aqueous solutions, Environ. Int., 134 (2020) 105340.

[4] R. Saravanathamizhan, V.T. Perarasu, K. Vetriselvan, Chapter 11 - Thermochemical conversion of biomass into valuable products and its modeling studies, in: M.P. Shah (Ed.) Green Approach to Alternative Fuel for a Sustainable Future, Elsevier, 2023, pp. 137-152.

[5] M. Kamali, L. Appels, E.E. Kwon, T.M. Aminabhavi, R. Dewil, Biochar in water and wastewater treatment - a sustainability assessment, Chemical Engineering Journal, 420 (2021) 129946.

[6] W. Liao, X. Zhang, S. Ke, J. Shao, H. Yang, S. Zhang, H. Chen, Effect of different biomass species and pyrolysis temperatures on heavy metal adsorption, stability and economy of biochar, Industrial Crops and Products, 186 (2022) 115238.

[7] FAO, The state of world fisheries and aquaculture. sustainability in action, (2020).

[8] K. Jeffery, S.C. Mangi, H. Conejo-Watt, A. Muench, K. Hyder, The potential of the UK inshore fleet to switch or integrate aquaculture to form a more holistic seafood production system, Ocean & Coastal Management, 202 (2021) 105503.

[9] T.A.T. Nguyen, K.A.T. Nguyen, C. Jolly, Is super-intensification the solution to shrimp production and export sustainability?, Sustainability, 11 (2019) 5277.

[10] Y.C. Shang, P. Leung, B.-H. Ling, Comparative economics of shrimp farming in Asia, Aquaculture, 164 (1998) 183-200.

[11] C.E. Boyd, R.P. Davis, A.A. McNevin, Perspectives on the mangrove conundrum, land use, and benefits of yield intensification in farmed shrimp production: A review, Journal of the World Aquaculture Society, 53 (2022) 8-46.

[12] IMARC, Shrimp market: global industry trends, share, size, growth, opportunity and forecast 2020-2025, Retrieved June, 25 (2020) 2020.

[13] R. Haque, P.B. Sawant, P. Sardar, T. Varghese, K.M. Xavier, N.K. Chadha, J.K. Sundaray, C. Haldar, P. Jana, S.S. Pattanaik, Shrimp shell waste-derived astaxanthin in synergistic

combination with its commercial variant augments gonadal maturation and upregulates vitellogenin gene expression of discus (Symphysodon aequifasciatus), Aquaculture, 562 (2023) 738828.

[14] T. Senphan, S. Benjakul, H. Kishimura, Characteristics and antioxidative activity of carotenoprotein from shells of Pacific white shrimp extracted using hepatopancreas proteases, Food Bioscience, 5 (2014) 54-63.

[15] P.T. Anh, T.T.M. Dieu, A.P. Mol, C. Kroeze, S.R. Bush, Towards eco-agro industrial clusters in aquatic production: the case of shrimp processing industry in Vietnam, Journal of cleaner production, 19 (2011) 2107-2118.

[16] J. Bautista, M. Jover, J. Gutierrez, R. Corpas, O. Cremades, E. Fontiveros, F. Iglesias, J. Vega, Preparation of crayfish chitin by in situ lactic acid production, Process Biochemistry, 37 (2001) 229-234.

[17] S. Chen, S. Jiang, H. Jiang, A review on conversion of crayfish-shell derivatives to functional materials and their environmental applications, Journal of bioresources and bioproducts, 5 (2020) 238-247.

[18] K.M. Eggink, R. Gonçalves, P.V. Skov, Shrimp Processing Waste in Aquaculture Feed: Nutritional Value, Applications, Challenges, and Prospects, Reviews in Aquaculture, (2024).

[19] A. Piotrowska-Kirschling, K. Szelągowska-Rudzka, J. Karczewski, J. Brzeska, Application of shrimp waste for the synthesis of polyurethane–chitosan materials with potential use in sorption of oil micro-spills in water treatment, Sustainability, 13 (2021) 5098.

[20] N. Yan, X. Chen, Sustainability: Don't waste seafood waste, Nature, 524 (2015) 155-157.

[21] G.M. Mathew, D.C. Mathew, R.K. Sukumaran, R. Sindhu, C.-C. Huang, P. Binod, R. Sirohi, S.-H. Kim, A. Pandey, Sustainable and eco-friendly strategies for shrimp shell valorization, Environmental Pollution, 267 (2020) 115656.

[22] N.P. Nirmal, C. Santivarangkna, M.S. Rajput, S. Benjakul, Trends in shrimp processing waste utilization: An industrial prospective, Trends Food Sci. Technol., 103 (2020) 20-35.

[23] J. Carvalho Pereira, A. Lemoine, P. Neubauer, S. Junne, Perspectives for improving circular economy in brackish shrimp aquaculture, Aquac. Res., 53 (2022) 1169-1180.

[24] C. Lalramchhani, A. Panigrahi, P.S.S. Anand, S. Das, T.K. Ghoshal, K. Ambasankar, C.P. Balasubramanian, Effect of varying levels of dietary protein on the growth performances of Indian white shrimp Penaeus indicus (H. Milne Edwards), Aquac., 519 (2020) 734736.

[25] D.P. Thakur, C.K. Lin, Water quality and nutrient budget in closed shrimp (Penaeus monodon) culture systems, Aquac. Eng., 27 (2003) 159-176.

[26] P.J. Walsh, P.A. Wright, Nitrogen metabolism and excretion, CRC Press, 1995.

[27] P. Chaikaew, N. Rugkarn, V. Pongpipatwattana, V. Kanokkantapong, Enhancing ecological-economic efficiency of intensive shrimp farm through in-out nutrient budget and feed conversion ratio, Sustain. Environ. Res., 29 (2019) 28.
[28] W. Sun, Phosphorus and nitrogen budget for inland, saline water shrimp ponds in Alabama, in, Auburn University, 2012.
[29] F. Li, J. Feng, X. Zhou, C. Xu, M. Haissam Jijakli, W. Zhang, F. Fang, Impact of rice-fish/shrimp co-culture on the N2O emission and NH3 volatilization in intensive aquaculture ponds, Science of The Total Environment, 655 (2019) 284-291.
[30] S.J. Funge-Smith, M.R.P. Briggs, Nutrient budgets in intensive shrimp ponds: implications for sustainability, Aquaculture, 164 (1998) 117-133.
[31] Z. Hu, J.W. Lee, K. Chandran, S. Kim, S.K. Khanal, Nitrous oxide (N2O) emission from aquaculture: a review, Environmental science & technology, 46 (2012) 6470-6480.
[32] M. Jasmin, N.M. Isa, M. Kamarudin, K. Lim, M. Karim, Evaluating Bacillus flexus as bioremediators for ammonia removal in shrimp culture water and wastewater and characterizing microbial communities in shrimp pond sludge, Brazilian Journal of Microbiology, 55 (2024) 529-536.
[33] S. Gräslund, B.-E. Bengtsson, Chemicals and biological products used in south-east Asian shrimp farming, and their potential impact on the environment — a review, Sci Total Environ., 280 (2001) 93-131.
[34] M. Shiri, S.A. Hashemifard, G. Abdi, The potential of microalgae Dunaliella salina to treat shrimp pond wastewater in a PAN/GO membrane bioreactor, Chemosphere, 318 (2023) 138001.
[35] B.T. Iber, N.A. Kasan, Recent advances in Shrimp aquaculture wastewater management, Heliyon, 7 (2021).
[36] T.B. Cahú, S.D. Santos, A. Mendes, C.R. Córdula, S.F. Chavante, L.B. Carvalho, H.B. Nader, R.S. Bezerra, Recovery of protein, chitin, carotenoids and glycosaminoglycans from Pacific white shrimp (Litopenaeus vannamei) processing waste, Process Biochemistry, 47 (2012) 570-577.
[37] T. Paul, S.K. Halder, A. Das, K. Ghosh, A. Mandal, P. Payra, P. Barman, P.K. Das Mohapatra, B.R. Pati, K.C. Mondal, Production of chitin and bioactive materials from Black tiger shrimp (Penaeus monodon) shell waste by the treatment of bacterial protease cocktail, 3 Biotech, 5 (2015) 483-493.
[38] J. Gómez-Estaca, A. Alemán, M.E. López-Caballero, G.C. Baccan, P. Montero, M.C. Gómez-Guillén, Bioaccessibility and antimicrobial properties of a shrimp demineralization extract blended with chitosan as wrapping material in ready-to-eat raw salmon, Food Chemistry,

276 (2019) 342-349.
[39] J. Li, W. Sun, H.S. Ramaswamy, Y. Yu, S. Zhu, J. Wang, H. Li, High pressure extraction of astaxanthin from shrimp waste (Penaeus Vannamei Boone): effect on yield and antioxidant activity, Journal of Food Process Engineering, 40 (2017) e12353.
[40] X. Chen, C. Li, X. Ji, Z. Zhong, P. Li, Recovery of protein from discharged wastewater during the production of chitin, Bioresour. Technol., 99 (2008) 570-574.
[41] S. Kannan, Y. Gariepy, G.S.V. Raghavan, Conventional Hydrothermal Carbonization of Shrimp Waste, Energy Fuels, 32 (2018) 3532-3542.
[42] N.P. Nirmal, C. Santivarangkna, M.S. Rajput, S. Benjakul, Trends in shrimp processing waste utilization: An industrial prospective, Trends in Food Science & Technology, 103 (2020) 20-35.
[43] R. Sowmya, N.M. Sachindra, Evaluation of antioxidant activity of carotenoid extract from shrimp processing byproducts by in vitro assays and in membrane model system, Food Chemistry, 134 (2012) 308-314.
[44] M.Y. Arancibia, M.E. López-Caballero, M.C. Gómez-Guillén, P. Montero, Chitosan coatings enriched with active shrimp waste for shrimp preservation, Food Control, 54 (2015) 259-266.
[45] S.S. Pattanaik, P.B. Sawant, K.A.M. Xavier, K. Dube, P.P. Srivastava, V. Dhanabalan, N.K. Chadha, Characterization of carotenoprotein from different shrimp shell waste for possible use as supplementary nutritive feed ingredient in animal diets, Aquac., 515 (2020) 734594.
[46] M. Fabbricino, L. Pontoni, Use of non-treated shrimp-shells for textile dye removal from wastewater, Journal of Environmental Chemical Engineering, 4 (2016) 4100-4106.
[47] F.-Y. Zheng, R. Li, S. Ge, W.-R. Xu, Y. Zhang, Nitrogen and phosphorus co-doped carbon networks derived from shrimp shells as an efficient oxygen reduction catalyst for microbial fuel cells, Journal of Power Sources, 446 (2020) 227356.
[48] O.M. Darwesh, Y.Y. Sultan, M.M. Seif, D.A. Marrez, Bio-evaluation of crustacean and fungal nano-chitosan for applying as food ingredient, Toxicology reports, 5 (2018) 348-356.
[49] B.E. Abdelmalek, A. Sila, Z. Ghlissi, M.A. Taktak, M.A. Ayadi, A. Bougatef, The influence of natural astaxanthin on the formulation and storage of marinated chicken steaks, Journal of Food Biochemistry, 40 (2016) 393-403.
[50] E. Gisbert, V. Fournier, M. Solovyev, A. Skalli, K.B. Andree, Diets containing shrimp protein hydrolysates provided protection to European sea bass (Dicentrarchus labrax) affected by a Vibrio pelagius natural infection outbreak, Aquaculture, 495 (2018) 136-143.
[51] S. Kannan, Y. Gariepy, G.V. Raghavan, Optimization and characterization of hydrochar

derived from shrimp waste, Energy & Fuels, 31 (2017) 4068-4077.
[52] T.e. al., Effect of shrimp shell waste on the properties of wheat gluten based-bioplastics, Journal of Polymers and the Environment, 26 (2018) 1775-1781.
[53] G. Yuan, Y. Jia, Y. Pan, W. Li, C. Wang, L. Xu, C. Wang, H. Chen, Preparation and characterization of shrimp shell waste protein-based films modified with oolong tea, corn silk and black soybean seed coat extracts, Polymer Testing, 81 (2020) 106235.
[54] D. Núñez-Gómez, A.A. de Almeida Alves, F.R. Lapolli, M.A. Lobo-Recio, Aplication of the statistical experimental design to optimize mine-impacted water (MIW) remediation using shrimp-shell, Chemosphere, 167 (2017) 322-329.
[55] D. Nunez-Gomez, C. Rodrigues, F.R. Lapolli, M.A. Lobo-Recio, Adsorption of heavy metals from coal acid mine drainage by shrimp shell waste: Isotherm and continuous-flow studies, Journal of Environmental Chemical Engineering, 7 (2019) 102787.
[56] M. Fabbricino, L. Pontoni, Use of non-treated shrimp-shells for textile dye removal from wastewater, Journal of Environmental Chemical Engineering, 4 (2016) 4100-4106.
[57] M.E.A. Ali, M.M.S. Aboelfadl, A.M. Selim, H.F. Khalil, G.M. Elkady, Chitosan nanoparticles extracted from shrimp shells, application for removal of Fe (II) and Mn (II) from aqueous phases, Separation Science and Technology, 53 (2018) 2870-2881.
[58] R. Andreazza, K.A. Heylmann, J. Cadaval, M.S. Quadro, S. Pieniz, F.d.O. Camargo, T.F. Afonso, C.F. Demarco, Copper adsorption by different extracts of shrimp chitin, Desalination and Water Treatment, 141 (2019) 220-228.
[59] T. Odoom-Wubah, Q. Li, R. Mulka, M. Chen, J. Huang, Q. Li, R. Luque, Calcified shrimp waste supported Pd NPs as an efficient catalyst toward benzene destruction, ACS Sustainable Chemistry & Engineering, 8 (2019) 486-497.
[60] L. Yan, P. Li, W. Zhou, Z. Wang, X. Fan, M. Chen, Y. Fang, H. Liu, Shrimp shell-inspired antifouling chitin nanofibrous membrane for efficient oil/water emulsion separation with in situ removal of heavy metal ions, ACS Sustainable Chemistry & Engineering, 7 (2018) 2064-2072.
[61] K. Kositkanawuth, M.L. Sattler, B. Dennis, Pyrolysis of macroalgae and polysytrene: a review, Curr. Sustainable/Renewable Energy Rep. , 1 (2014) 121-128.
[62] X. Liu, F. Shen, X. Qi, Adsorption recovery of phosphate from aqueous solution by CaO-biochar composites prepared from eggshell and rice straw, Sci. Total Environ., 666 (2019) 694-702.
[63] L. Dai, F. Tan, H. Li, N. Zhu, M. He, Q. Zhu, G. Hu, L. Wang, J. Zhao, Calcium-rich biochar from the pyrolysis of crab shell for phosphorus removal, J. Environ. Manage., 198

(2017) 70-74.
[64] Y. Zhu, Q. Zhao, D. Li, J. Li, W. Guo, Enhanced recovery of phosphorus in sewage sludge-derived biochar with CaCO3: Phosphorus speciation and slow-release phosphorus behavior, Sep. Purif. Technol., 311 (2023) 123325.
[65] W.A.W. Mahari, E. Azwar, S.Y. Foong, A. Ahmed, W. Peng, M. Tabatabaei, M. Aghbashlo, Y.-K. Park, C. Sonne, S.S. Lam, Valorization of municipal wastes using co-pyrolysis for green energy production, energy security, and environmental sustainability: A review, Chemical Engineering Journal, 421 (2021) 129749.
[66] N.K. Niazi, I. Bibi, M. Shahid, Y.S. Ok, S.M. Shaheen, J. Rinklebe, H. Wang, B. Murtaza, E. Islam, M.F. Nawaz, Arsenic removal by Japanese oak wood biochar in aqueous solutions and well water: Investigating arsenic fate using integrated spectroscopic and microscopic techniques, Science of the Total Environment, 621 (2018) 1642-1651.
[67] N.K. Niazi, I. Bibi, M. Shahid, Y.S. Ok, E.D. Burton, H. Wang, S.M. Shaheen, J. Rinklebe, A. Lüttge, Arsenic removal by perilla leaf biochar in aqueous solutions and groundwater: an integrated spectroscopic and microscopic examination, Environmental Pollution, 232 (2018) 31-41.
[68] M. Zhang, G. Song, D.L. Gelardi, L. Huang, E. Khan, O. Mašek, S.J. Parikh, Y.S. Ok, Evaluating biochar and its modifications for the removal of ammonium, nitrate, and phosphate in water, Water Research, 186 (2020) 116303.
[69] X. Gai, H. Wang, J. Liu, L. Zhai, S. Liu, T. Ren, H. Liu, Effects of feedstock and pyrolysis temperature on biochar adsorption of ammonium and nitrate, PloS one, 9 (2014) e113888.
[70] C.C. Hollister, J.J. Bisogni, J. Lehmann, Ammonium, nitrate, and phosphate sorption to and solute leaching from biochars prepared from corn stover (Zea mays L.) and oak wood (Quercus spp.), Journal of environmental quality, 42 (2013) 137-144.
[71] S. Hale, V. Alling, V. Martinsen, J. Mulder, G. Breedveld, G. Cornelissen, The sorption and desorption of phosphate-P, ammonium-N and nitrate-N in cacao shell and corn cob biochars, Chemosphere, 91 (2013) 1612-1619.
[72] Y. Yao, B. Gao, J. Chen, L. Yang, Engineered biochar reclaiming phosphate from aqueous solutions: mechanisms and potential application as a slow-release fertilizer, Environmental science & technology, 47 (2013) 8700-8708.
[73] D. Mohan, S. Rajput, V.K. Singh, P.H. Steele, C.U. Pittman Jr, Modeling and evaluation of chromium remediation from water using low cost bio-char, a green adsorbent, Journal of hazardous materials, 188 (2011) 319-333.
[74] K. Yakkala, M.-R. Yu, H. Roh, J.-K. Yang, Y.-Y. Chang, Buffalo weed (Ambrosia trifida

L. var. trifida) biochar for cadmium (II) and lead (II) adsorption in single and mixed system, Desalination and Water Treatment, 51 (2013) 7732-7745.
[75] D. Kołodyńska, R. Wnętrzak, J. Leahy, M. Hayes, W. Kwapiński, Z. Hubicki, Kinetic and adsorptive characterization of biochar in metal ions removal, Chemical Engineering Journal, 197 (2012) 295-305.
[76] X.-j. Tong, J.-y. Li, J.-h. Yuan, R.-k. Xu, Adsorption of Cu (II) by biochars generated from three crop straws, Chemical Engineering Journal, 172 (2011) 828-834.
[77] X. Xu, X. Cao, L. Zhao, H. Wang, H. Yu, B. Gao, Removal of Cu, Zn, and Cd from aqueous solutions by the dairy manure-derived biochar, Environmental Science and Pollution Research, 20 (2013) 358-368.
[78] H. Wang, H. Wang, H. Zhao, Q. Yan, Adsorption and Fenton-like removal of chelated nickel from Zn-Ni alloy electroplating wastewater using activated biochar composite derived from Taihu blue algae, Chemical Engineering Journal, 379 (2020) 122372.
[79] M. Zafar, N. Van Vinh, S.K. Behera, H.-S. Park, Ethanol mediated As (III) adsorption onto Zn-loaded pinecone biochar: experimental investigation, modeling, and optimization using hybrid artificial neural network-genetic algorithm approach, Journal of environmental sciences, 54 (2017) 114-125.
[80] L. Divband Hafshejani, A. Hooshmand, A.A. Naseri, A.S. Mohammadi, F. Abbasi, A. Bhatnagar, Removal of nitrate from aqueous solution by modified sugarcane bagasse biochar, Ecological Engineering, 95 (2016) 101-111.
[81] Q. Yin, H. Ren, R. Wang, Z. Zhao, Evaluation of nitrate and phosphate adsorption on Al-modified biochar: Influence of Al content, Science of The Total Environment, 631-632 (2018) 895-903.
[82] J. Yu, L. Tang, Y. Pang, G. Zeng, H. Feng, J. Zou, J. Wang, C. Feng, X. Zhu, X. Ouyang, Hierarchical porous biochar from shrimp shell for persulfate activation: A two-electron transfer path and key impact factors, Applied Catalysis B: Environmental, 260 (2020) 118160.
[83] J. Yu, H. Feng, L. Tang, Y. Pang, J. Wang, J. Zou, Q. Xie, Y. Liu, C. Feng, J. Wang, Insight into the key factors in fast adsorption of organic pollutants by hierarchical porous biochar, Journal of hazardous materials, 403 (2021) 123610.
[84] J. Liu, X. Yang, H. Liu, W. Cheng, Y. Bao, Modification of calcium-rich biochar by loading Si/Mn binary oxide after NaOH activation and its adsorption mechanisms for removal of Cu (II) from aqueous solution, Colloids and Surfaces A: Physicochemical and Engineering Aspects, 601 (2020) 124960.
[85] C. He, H. Lin, L. Dai, R. Qiu, Y. Tang, Y. Wang, P.-G. Duan, Y.S. Ok, Waste shrimp shell-

derived hydrochar as an emergent material for methyl orange removal in aqueous solutions, Environment international, 134 (2020) 105340.

[86] A.S. Eltaweil, A.M. Omer, H.G. El-Aqapa, N.M. Gaber, N.F. Attia, G.M. El-Subruiti, M.S. Mohy-Eldin, E.M. Abd El-Monaem, Chitosan based adsorbents for the removal of phosphate and nitrate: A critical review, Carbohydr. Polym., 274 (2021) 118671.

[87] S. Pap, C. Kirk, B. Bremner, M. Turk Sekulic, L. Shearer, S.W. Gibb, M.A. Taggart, Low-cost chitosan-calcite adsorbent development for potential phosphate removal and recovery from wastewater effluent, Water Res., 173 (2020) 115573.

[88] J. Jang, D.S. Lee, Effective phosphorus removal using chitosan/Ca-organically modified montmorillonite beads in batch and fixed-bed column studies, J. Hazard. Mater., 375 (2019) 9-18.

[89] M.E. Mahmoud, A.K. Mohamed, M.A. Salam, Self-decoration of N-doped graphene oxide 3-D hydrogel onto magnetic shrimp shell biochar for enhanced removal of hexavalent chromium, Journal of Hazardous Materials, 408 (2021) 124951.

[90] S. Chen, H. Cai, X. Du, P. Wu, X. Tao, J. Zhou, Z. Dang, G. Lu, Adsorption behavior of hierarchical porous biochar from shrimp shell for tris(2-chloroethyl) phosphate (TCEP): Sorption experiments and DFT calculations, Environmental Research, 219 (2023) 115128.

[91] M. Wang, J. Yan, Y. Xu, X. Zhou, Y. Diao, H. Wang, J. Bian, C. Liu, G. Quan, Mechanochemical modified nitrogen-rich biochar derived from shrimp shell: Dominant mechanism in pyridinic-N for aquatic methylene blue removal, Journal of Environmental Management, 329 (2023) 117049.

[92] X. Liu, C. He, X. Yu, Y. Bai, L. Ye, B. Wang, L. Zhang, Net-like porous activated carbon materials from shrimp shell by solution-processed carbonization and H3PO4 activation for methylene blue adsorption, Powder Technology, 326 (2018) 181-189.

[93] L. Qin, Z. Zhou, J. Dai, P. Ma, H. Zhao, J. He, A. Xie, C. Li, Y. Yan, Novel N-doped hierarchically porous carbons derived from sustainable shrimp shell for high-performance removal of sulfamethazine and chloramphenicol, Journal of the Taiwan Institute of Chemical Engineers, 62 (2016) 228-238.

[94] T. Sun, Y. Xu, Y. Sun, L. Wang, X. Liang, H. Jia, Crayfish shell biochar for the mitigation of Pb contaminated water and soil: Characteristics, mechanisms, and applications, Environmental Pollution, 271 (2021) 116308.

[95] L. Long, Y. Xue, Y. Zeng, K. Yang, C. Lin, Synthesis, characterization and mechanism analysis of modified crayfish shell biochar possessed ZnO nanoparticles to remove trichloroacetic acid, Journal of Cleaner Production, 166 (2017) 1244-1252.

[96] A.N.M. Faizal, C.H. Wen, N.R. Putra, A.S. Zaini, A. Agi, A.H. Nordin, M.A.A. Zaini, Crayfish shell biochar for methyl violet adsorption: Equilibrium and kinetic studies, Next Sustainability, 6 (2025) 100093.

[97] L. Yan, F.-X. Dong, Y. Li, P.-R. Guo, L.-J. Kong, W. Chu, Z.-H. Diao, Synchronous removal of Cr(VI) and phosphates by a novel crayfish shell biochar-Fe composite from aqueous solution: Reactivity and mechanism, J. Environ. Chem. Eng., 10 (2022) 107396.

[98] J.-H. Park, J.J. Wang, R. Xiao, B. Zhou, R.D. Delaune, D.-C. Seo, Effect of pyrolysis temperature on phosphate adsorption characteristics and mechanisms of crawfish char, Journal of colloid and Interface Science, 525 (2018) 143-151.

[99] H. Flower, M. Rains, Y. Taşcı, J.-Z. Zhang, K. Trout, D. Lewis, A. Das, R. Dalton, Why is calcite a strong phosphorus sink in freshwater? Investigating the adsorption mechanism using batch experiments and surface complexation modeling, Chemosphere, 286 (2022) 131596.

[100] B. Wu, J. Wan, Y. Zhang, B. Pan, I.M. Lo, Selective phosphate removal from water and wastewater using sorption: process fundamentals and removal mechanisms, Environ. Sci. Technol., 54 (2019) 50-66.

[101] G. Bharath, B.S. Latha, E.H. Alsharaeh, P. Prakash, N. Ponpandian, Enhanced hydroxyapatite nanorods formation on graphene oxide nanocomposite as a potential candidate for protein adsorption, pH controlled release and an effective drug delivery platform for cancer therapy, Anal. Methods, 9 (2017) 240-252.

[102] Y. Liu, J. Huang, H. Li, Synthesis of hydroxyapatite–reduced graphite oxide nanocomposites for biomedical applications: oriented nucleation and epitaxial growth of hydroxyapatite, J. Mater. Chem. B, 1 (2013) 1826-1834.

[103] D. Mohan, A. Sarswat, Y.S. Ok, C.U. Pittman, Organic and inorganic contaminants removal from water with biochar, a renewable, low cost and sustainable adsorbent – A critical review, Bioresour. Technol., 160 (2014) 191-202.

[104] M. Wang, J. Yan, Y. Xu, X. Zhou, Y. Diao, H. Wang, J. Bian, C. Liu, G. Quan, Mechanochemical modified nitrogen-rich biochar derived from shrimp shell: Dominant mechanism in pyridinic-N for aquatic methylene blue removal, J. Environ. Manag., 329 (2023) 117049.

[105] J. Yu, X. Li, M. Wu, K. Lin, L. Xu, T. Zeng, H. Shi, M. Zhang, Synergistic role of inherent calcium and iron minerals in paper mill sludge biochar for phosphate adsorption, Sci. Total Environ., 834 (2022) 155193.

[106] W.A. Wan Mahari, K. Waiho, E. Azwar, H. Fazhan, W. Peng, S.D. Ishak, M. Tabatabaei, P.N.Y. Yek, F. Almomani, M. Aghbashlo, S.S. Lam, A state-of-the-art review on producing

engineered biochar from shellfish waste and its application in aquaculture wastewater treatment, Chemosphere, 288 (2022) 132559.
[107] H. Kazemi Shariat Panahi, M. Dehhaghi, Y.S. Ok, A.-S. Nizami, B. Khoshnevisan, S.I. Mussatto, M. Aghbashlo, M. Tabatabaei, S.S. Lam, A comprehensive review of engineered biochar: Production, characteristics, and environmental applications, J. Clean. Prod., 270 (2020) 122462.
[108] K. Mesecke, W. Malorny, L.N. Warr, Understanding the effect of sulfate ions on the hydrothermal curing of autoclaved aerated concrete, Cem. Concr. Res., 164 (2023) 107044.
[109] T. Hirsch, B. Lothenbach, Phase stabilities and thermodynamic properties of crystalline phases in CaO–SiO2–H2O above 100° C, Cem. Concr. Res., 177 (2024) 107412.
[110] S. Kang, J. Lee, S.-M. Park, D.S. Alessi, K. Baek, Adsorption characteristics of cesium onto calcium-silicate-hydrate in concrete powder and block, Chemosphere, 259 (2020) 127494.
[111] S. Pap, P.P.J. Gaffney, B. Bremner, M. Turk Sekulic, S. Maletic, S.W. Gibb, M.A. Taggart, Enhanced phosphate removal and potential recovery from wastewater by thermo-chemically calcinated shell adsorbents, Science of The Total Environment, 814 (2022) 152794.
[112] J. Zhang, J. Jin, M. Wang, R. Naidu, Y. Liu, Y.B. Man, X. Liang, M.H. Wong, P. Christie, Y. Zhang, Co-pyrolysis of sewage sludge and rice husk/bamboo sawdust for biochar with high aromaticity and low metal mobility, Environ. Res., 191 (2020) 110034.
[113] W.-Y. Huang, D. Li, Z.-Q. Liu, Q. Tao, Y. Zhu, J. Yang, Y.-M. Zhang, Kinetics, isotherm, thermodynamic, and adsorption mechanism studies of La(OH)3-modified exfoliated vermiculites as highly efficient phosphate adsorbents, J. Chem. Eng., 236 (2014) 191-201.
[114] Y. Feng, Y. Luo, Q. He, D. Zhao, K. Zhang, S. Shen, F. Wang, Performance and mechanism of a biochar-based Ca-La composite for the adsorption of phosphate from water, J. Environ. Chem. Eng., 9 (2021) 105267.
[115] S. Zeng, E. Kan, Sustainable use of Ca(OH)2 modified biochar for phosphorus recovery and tetracycline removal from water, Sci. Total Environ., 839 (2022) 156159.
[116] M. Lillo-Ródenas, J. Marco-Lozar, D. Cazorla-Amorós, A. Linares-Solano, Activated carbons prepared by pyrolysis of mixtures of carbon precursor/alkaline hydroxide, Journal of Analytical and Applied Pyrolysis, 80 (2007) 166-174.
[117] M. Musa, M. Sanagi, H. Nur, W.W. Ibrahim, Understanding pore formation and structural deformation in carbon spheres during KOH activation, Sains Malays, 44 (2015) 613-618.
[118] M.R. Parsa, A.L. Chaffee, The effect of densification with alkali hydroxides on brown coal self-heating behaviour and physico-chemical properties, Fuel, 240 (2019) 299-308.
[119] W. Zhang, Y. He, Y. Wang, G. Li, J. Chen, Y. Zhu, Comprehensive investigation on the

gasification reactivity of pyrolysis residue derived from Ca-rich petrochemical sludge: Roles of microstructure characteristics and calcium evolution, Energy Convers. Manag., 253 (2022) 115150.

[120] L. Cao, Z. Ouyang, T. Chen, H. Huang, M. Zhang, Z. Tai, K. Long, C. Sun, B. Wang, Phosphate removal from aqueous solution using calcium-rich biochar prepared by the pyrolysis of crab shells, Environ. Sci. Pollut. Res., 29 (2022) 89570-89584.

[121] A. Ullrich, K. Garbev, U. Schweike, M. Köhler, B. Bergfeldt, P. Stemmermann, CaCl2 as a mineralizing agent in low-temperature recycling of autoclaved aerated concrete: Cl-Immobilization by formation of chlorellestadite, Minerals, 12 (2022) 1142.

[122] E. Ferraz, J.A. Gamelas, J. Coroado, C. Monteiro, F. Rocha, Recycling waste seashells to produce calcitic lime: characterization and wet slaking reactivity, Waste Biomass Valori., 10 (2019) 2397-2414.

[123] H. Moussout, H. Ahlafi, M. Aazza, C. Sekkate, Kinetic and mechanism studies of the isothermal degradation of local chitin, chitosan and its biocomposite bentonite/chitosan, Cellulose, 25 (2018) 5593-5609.

[124] T. Nalini, S.K. Basha, A.M. Mohamed Sadiq, V.S. Kumari, K. Kaviyarasu, Development and characterization of alginate / chitosan nanoparticulate system for hydrophobic drug encapsulation, J. Drug Deliv. Sci. Tech., 52 (2019) 65-72.

[125] N. Wu, Y. Wang, R. Liu, Q. Wen, H. Liu, X. Xiong, Structural evolution and synthesis mechanism of ytterbium disilicate powders prepared by cocurrent chemical coprecipitation method, Ceram. Int., 48 (2022) 11545-11554.

[126] W. Yan, D. Liu, D. Tan, P. Yuan, M. Chen, FTIR spectroscopy study of the structure changes of palygorskite under heating, Spectrochim Acta A Mol Biomol Spectrosc., 97 (2012) 1052-1057.

[127] M.V. Reddy, M. Pathak, Sol-gel combustion synthesis of Ag doped CaSiO3: in vitro bioactivity, antibacterial activity and cytocompatibility studies for biomedical applications, Mater. Tech., 33 (2018) 38-47.

[128] S. Singh, D. Singh, Structural and optical properties of green emitting Y 2 SiO 5: Tb 3+ and Gd 2 SiO 5: Tb 3+ nanoparticles for modern lighting applications, Rare Metals, 40 (2021) 3289-3298.

[129] Y.N. Fang, C. Ritter, T.J. White, Crystal chemical characteristics of ellestadite-type apatite: implications for toxic metal immobilization, Dalton Transactions, 43 (2014) 16031-16043.

[130] Y. Banno, R. Miyawaki, K. Momma, M. Bunno, A CO3-bearing member of the

hydroxylapatite–hydroxylellestadite series from Tadano, Fukushima Prefecture, Japan: CO3-SO4 substitution in the apatite–ellestadite series, Mineralogical Magazine, 80 (2016) 363-370.
[131] E. Eren, H. Gumus, N. Ozbay, Equilibrium and thermodynamic studies of Cu(II) removal by iron oxide modified sepiolite, Desalination, 262 (2010) 43-49.
[132] N. Li, N. Farzadnia, C. Shi, Microstructural changes in alkali-activated slag mortars induced by accelerated carbonation, Cem. Concr. Res., 100 (2017) 214-226.
[133] M. Lanzón, J.A. Madrid-Mendoza, D. Navarro-Moreno, V.E. García-Vera, Use of eggshell waste: A green and effective method for the synthesis of pure calcium hydroxide suspensions, Constr. Build. Mater., 377 (2023) 131106.
[134] J.-H. Gan, C.-H. Xu, H.-Z. Zhu, F. Mao, F. Yang, Q. Zhou, S.-Q. Sun, Analysis and discrimination of ten different sponges by multi-step infrared spectroscopy, Chin. Chem. Lett., 26 (2015) 215-220.
[135] C. Liu, X. Wang, S. Yang, Z. Ren, C. Li, Z. Hu, Utilization of polyepoxysuccinic acid as a green depressant for the flotation separation of smithsonite from calcite, Miner. Eng., 168 (2021) 106933.
[136] D.H. Chu, M. Vinoba, M. Bhagiyalakshmi, I.H. Baek, S.C. Nam, Y. Yoon, S.H. Kim, S.K. Jeong, CO 2 mineralization into different polymorphs of CaCO 3 using an aqueous-CO 2 system, RSC Adv., 3 (2013) 21722-21729.
[137] D. Wei, Q. Du, S. Guo, D. Jia, Y. Wang, B. Li, Y. Zhou, Structures, bonding strength and in vitro bioactivity and cytotoxicity of electrochemically deposited bioactive nano-brushite coating/TiO2 nanotubes composited films on titanium, Surf. Coat. Technol., 340 (2018) 93-102.
[138] J. Baltrusaitis, C.R. Usher, V.H. Grassian, Reactions of sulfur dioxide on calcium carbonate single crystal and particle surfaces at the adsorbed water carbonate interface, Phys. Chem. Chem. Phys., 9 (2007) 3011-3024.
[139] T. Wang, B. Feng, Y. Guo, W. Zhang, Y. Rao, C. Zhong, L. Zhang, C. Cheng, H. Wang, X. Luo, The flotation separation behavior of apatite from calcite using carboxymethyl chitosan as depressant, Miner. Eng., 159 (2020) 106635.
[140] Z. Wang, C. Zhang, Polyvinylidene fluoride cladded calcite tablet for phosphate removal and reclamation from aqueous solution, J. Environ. Chem. Eng., 7 (2019) 103429.
[141] A. Das, H. Li, R. Kataki, P.S. Agrawal, N. Moyon, B. Gurunathan, S.L. Rokhum, Terminalia arjuna bark–A highly efficient renewable heterogeneous base catalyst for biodiesel production, Renew. Energy, 212 (2023) 185-196.
[142] N. Gilbert, Environment: The disappearing nutrient. Nature News 461, 716–718., Resour.

Conserv. Recycl., 93 (2014) 178-187.
[143] T. Aketo, K. Waga, Y. Yabu, Y. Maeda, T. Yoshino, A. Hanada, K. Sano, T. Kamiya, H. Takano, T. Tanaka, Algal biomass production by phosphorus recovery and recycling from wastewater using amorphous calcium silicate hydrates, Bioresour. Technol., 340 (2021) 125678.
[144] B.K. Martini, T.G. Daniel, M.Z. Corazza, A.E. de Carvalho, Methyl orange and tartrazine yellow adsorption on activated carbon prepared from boiler residue: Kinetics, isotherms, thermodynamics studies and material characterization, J. Environ. Chem. Eng. , 6 (2018) 6669-6679.
[145] Z. Wang, J. Su, X. Hu, A. Ali, Z. Wu, Isolation of biosynthetic crystals by microbially induced calcium carbonate precipitation and their utilization for fluoride removal from groundwater, J. Hazard. Mater., 406 (2021) 124748.
[146] N. Bouchelkia, H. Tahraoui, A. Amrane, H. Belkacemi, J.-C. Bollinger, A. Bouzaza, A. Zoukel, J. Zhang, L. Mouni, Jujube stones based highly efficient activated carbon for methylene blue adsorption: Kinetics and isotherms modeling, thermodynamics and mechanism study, optimization via response surface methodology and machine learning approaches, Process Saf. Environ. Prot., 170 (2023) 513-535.
[147] J.O. Eduah, E.K. Nartey, M.K. Abekoe, S.W. Henriksen, M.N. Andersen, Mechanism of orthophosphate (PO4-P) adsorption onto different biochars, Environmental Technology & Innovation, 17 (2020) 100572.
[148] J.-H. Park, J.J. Wang, R. Xiao, B. Zhou, R.D. Delaune, D.-C. Seo, Effect of pyrolysis temperature on phosphate adsorption characteristics and mechanisms of crawfish char, J. Colloid Interface Sci., 525 (2018) 143-151.
[149] L. Yan, F.-X. Dong, Y. Li, P.-R. Guo, L.-J. Kong, W. Chu, Z.-H. Diao, Synchronous removal of Cr(VI) and phosphates by a novel crayfish shell biochar-Fe composite from aqueous solution: Reactivity and mechanism, Journal of Environmental Chemical Engineering, 10 (2022) 107396.
[150] Y. Deng, M. Li, Z. Zhang, Q. Liu, K. Jiang, J. Tian, Y. Zhang, F. Ni, Comparative study on characteristics and mechanism of phosphate adsorption on Mg/Al modified biochar, Journal of Environmental Chemical Engineering, 9 (2021) 105079.
[151] Q. Yang, X. Wang, W. Luo, J. Sun, Q. Xu, F. Chen, J. Zhao, S. Wang, F. Yao, D. Wang, X. Li, G. Zeng, Effectiveness and mechanisms of phosphate adsorption on iron-modified biochars derived from waste activated sludge, Bioresource Technology, 247 (2018) 537-544.
[152] S. Khandaker, Y. Toyohara, G.C. Saha, M.R. Awual, T. Kuba, Development of synthetic

zeolites from bio-slag for cesium adsorption: Kinetic, isotherm and thermodynamic studies, Journal of Water Process Engineering, 33 (2020) 101055.

[153] A. Manyatshe, Z.E. Cele, M.O. Balogun, T.T. Nkambule, T.A. Msagati, Chitosan modified sugarcane bagasse biochar for the adsorption of inorganic phosphate ions from aqueous solution, J. Environ. Chem. Eng., 10 (2022) 108243.

[154] L. Li, Q. Chen, C. Zhao, B. Guo, X. Xu, T. Liu, L. Zhao, A novel chitosan modified magnesium impregnated corn straw biochar for ammonium and phosphate removal from simulated livestock wastewater, Environ. Technol. Innov., 26 (2022) 102519.

[155] W.-T. Chen, C.-W. Lin, P.-K. Shih, W.-L. Chang, Adsorption of phosphate into waste oyster shell: thermodynamic parameters and reaction kinetics, Desalin. Water Treat., 47 (2012) 86-95.

[156] N.Y. Mezenner, A. Bensmaili, Kinetics and thermodynamic study of phosphate adsorption on iron hydroxide-eggshell waste, J. Chem. Eng., 147 (2009) 87-96.

[157] W. Konicki, M. Aleksandrzak, E. Mijowska, Equilibrium, kinetic and thermodynamic studies on adsorption of cationic dyes from aqueous solutions using graphene oxide, Chem. Eng. Res. Des., 123 (2017) 35-49.

[158] Y. Zhang, S. Pan, H. Shen, M. Hu, Amino-functionalized Nano-size Composite Materials for Dispersive Solid-Phase Extraction of Phosphate in Water Samples, Anal. Sci. , 28 (2012) 887-892.

[159] L. Pazourková, G.S. Martynková, M. Šupová, Ca-deficient hydroxyapatite synthesis on the bioapatite bovine bone substrate study, Mater. Today: Proc., 52 (2022) 227-231.

[160] K.R. Mohamed, S.M. Mousa, G.T. El Bassyouni, Fabrication of nano structural biphasic materials from phosphogypsum waste and their in vitro applications, Mater. Res. Bull., 50 (2014) 432-439.

[161] P. Cheng, Y. Liu, L. Yang, Q. Ren, X. Wang, Y. Chi, H. Yuan, S. Wang, Y.-X. Ren, Phosphate adsorption using calcium aluminate decahydrate to achieve low phosphate concentrations: Batch and fixed-bed column studies, J. Environ. Chem. Eng., 11 (2023) 109377.

[162] S. Pérez, J. Muñoz-Saldaña, J.A. Garcia-Nunez, N. Acelas, E. Flórez, Unraveling the Ca–P species produced over the time during phosphorus removal from aqueous solution using biocomposite of eggshell-palm mesocarp fiber, Chemosphere, 287 (2022) 132333.

[163] B. Demri, D. Muster, XPS study of some calcium compounds, J. Mater. Process. Technol., 55 (1995) 311-314.

[164] D. Fang, L. Huang, Z. Fang, Q. Zhang, Q. Shen, Y. Li, X. Xu, F. Ji, Evaluation of porous calcium silicate hydrate derived from carbide slag for removing phosphate from wastewater,

Chem. Eng. J., 354 (2018) 1-11.
[165] F. Pan, H. Wei, Y. Huang, J. Song, M. Gao, Z. Zhang, R. Teng, S. Jing, Phosphorus adsorption by calcium chloride-modified buckwheat hulls biochar and the potential application as a fertilizer, J. Clean. Prod., 444 (2024) 141233.
[166] J. Wang, Y. Pan, R. Feng, H. Cui, B. Gong, L. Zhang, Z. Gao, X. Cui, H. Zhang, Z. Jia, Effect of electrolyte composition on the microstructure and bio-corrosion behavior of micro-arc oxidized coatings on biomedical Ti6Al4V alloy, J. Mater. Res. Technol. , 9 (2020) 1477-1490.
[167] D. Mitrogiannis, M. Psychoyou, I. Baziotis, V.J. Inglezakis, N. Koukouzas, N. Tsoukalas, D. Palles, E. Kamitsos, G. Oikonomou, G. Markou, Removal of phosphate from aqueous solutions by adsorption onto Ca (OH) 2 treated natural clinoptilolite, J. Chem. Eng., 320 (2017) 510-522.
[168] J. Li, L. Cao, B. Li, H. Huang, W. Yu, C. Sun, K. Long, B. Young, Utilization of activated sludge and shell wastes for the preparation of Ca-loaded biochar for phosphate removal and recovery, J. Clean. Prod., 382 (2023) 135395.
[169] D. Potphode, M.S. Sayed, T. Lama Tamang, J.-J. Shim, High-performance binder-free flower-like (Ni0.66Co0.3Mn0.04)2(OH)2(CO3) array synthesized using ascorbic acid for supercapacitor applications, Chem. Eng. J., 378 (2019) 122129.
[170] S.S. Emmanuel, A.A. Adesibikan, E.A. Opatola, C.O. Olawoyin, A pragmatic review on photocatalytic degradation of methyl orange dye pollutant using greenly biofunctionalized nanometallic materials: A focus on aquatic body, Appl. Organomet. Chem., 37 (2023) e7108.
[171] H. Alyasi, H. Mackey, G. McKay, Adsorption of Methyl Orange from Water Using Chitosan Bead-like Materials, Mol., 28 (2023) 6561.
[172] E.A. Mohamed, A.Q. Selim, S.A. Ahmed, L. Sellaoui, A. Bonilla-Petriciolet, A. Erto, Z. Li, Y. Li, M.K. Seliem, H2O2-activated anthracite impregnated with chitosan as a novel composite for Cr (VI) and methyl orange adsorption in single-compound and binary systems: Modeling and mechanism interpretation, Chem. Eng. J., 380 (2020) 122445.
[173] M.U. Dao, H.S. Le, H.Y. Hoang, V.A. Tran, V.D. Doan, T.T.N. Le, A. Sirotkin, V.T. Le, Natural core-shell structure activated carbon beads derived from Litsea glutinosa seeds for removal of methylene blue: Facile preparation, characterization, and adsorption properties, Environ. Res., 198 (2021) 110481.
[174] Z. Zeng, S. Ye, H. Wu, R. Xiao, G. Zeng, J. Liang, C. Zhang, J. Yu, Y. Fang, B. Song, Research on the sustainable efficacy of g-MoS2 decorated biochar nanocomposites for removing tetracycline hydrochloride from antibiotic-polluted aqueous solution, Sci. Total

Environ., 648 (2019) 206-217.
[175] M.L. Firmansyah, S. Abdel-Azeim, N. Ullah, Efficient adsorption of methyl red, methyl orange and bromothymol blue by polyamine resin: Role of linearity and size of carboxylate in enhanced encapsulation and molecular matching, J. Mol. Liq., 411 (2024) 125792.
[176] L. Meili, P.V.S. Lins, M.T. Costa, R.L. Almeida, A.K.S. Abud, J.I. Soletti, G.L. Dotto, E.H. Tanabe, L. Sellaoui, S.H.V. Carvalho, A. Erto, Adsorption of methylene blue on agroindustrial wastes: Experimental investigation and phenomenological modelling, Progress in Biophysics and Molecular Biology, 141 (2019) 60-71.
[177] A. Waheed, M. Mansha, I.W. Kazi, N. Ullah, Synthesis of a novel 3, 5-diacrylamidobenzoic acid based hyper-cross-linked resin for the efficient adsorption of Congo Red and Rhodamine B, J. Hazard. Mater., 369 (2019) 528-538.
[178] J. Wang, W. Chen, M. Zhang, R. Zhou, J. Li, W. Zhao, L. Wang, Optimize the preparation of Fe 3 O 4-modified magnetic mesoporous biochar and its removal of methyl orange in wastewater, Environ. Monit. Assess., 193 (2021) 1-20.
[179] S. Chen, Y. Huang, X. Han, Z. Wu, C. Lai, J. Wang, Q. Deng, Z. Zeng, S. Deng, Simultaneous and efficient removal of Cr(VI) and methyl orange on LDHs decorated porous carbons, Chem. Eng. J., 352 (2018) 306-315.
[180] I. Ali, I. Burakova, E. Galunin, A. Burakov, E. Mkrtchyan, A. Melezhik, D. Kurnosov, A. Tkachev, V. Grachev, High-speed and high-capacity removal of methyl orange and malachite green in water using newly developed mesoporous carbon: kinetic and isotherm studies, ACS omega, 4 (2019) 19293-19306.
[181] Y. Li, K. Zhou, M. He, J. Yao, Synthesis of ZIF-8 and ZIF-67 using mixed-base and their dye adsorption, Micropor Mesopor. Mat., 234 (2016) 287-292.
[182] B.L. Tran, H.-Y. Chin, B.K. Chang, A.S. Chiang, Dye adsorption in ZIF-8: The importance of external surface area, Micropor Mesopor. Mat., 277 (2019) 149-153.
[183] E. Çağlar, Y.O. Donar, A. Sinağ, I. Biroğul, S. Bilge, K. Aydincak, O. Pliekhov, Adsorption of anionic and cationic dyes on biochars, produced by hydrothermalcarbonization of waste biomass: effect of surface functionalization and ionicstrength, Turk. J. Chem., 42 (2018) 86-99.
[184] B. Li, Q. Wang, J.-Z. Guo, W.-W. Huan, L. Liu, Sorption of methyl orange from aqueous solution by protonated amine modified hydrochar, Bioresour. Technol., 268 (2018) 454-459.
[185] B. Zhang, Y. Wu, L. Cha, Removal of methyl orange dye using activated biochar derived from pomelo peel wastes: performance, isotherm, and kinetic studies, J. Disper. Sci. Technol., (2019).

[186] N.X. Loc, P.T.T. Tuyen, L.C. Mai, D.T.M. Phuong, Chitosan-modified biochar and unmodified biochar for methyl orange: Adsorption characteristics and mechanism exploration, Toxics, 10 (2022) 500.

[187] H. Alijani, Z. Shariatinia, A. Aroujalian Mashhadi, Water assisted synthesis of MWCNTs over natural magnetic rock: An effective magnetic adsorbent with enhanced mercury(II) adsorption property, Chem. Eng. J., 281 (2015) 468-481.

[188] I. Ghodbane, O. Hamdaoui, Removal of mercury (II) from aqueous media using eucalyptus bark: kinetic and equilibrium studies, J. Hazard. Mater., 160 (2008) 301-309.

[189] M. Jain, S.A. Khan, A. Sahoo, P. Dubey, K.K. Pant, Z.M. Ziora, M.A. Blaskovich, Statistical evaluation of cow-dung derived activated biochar for phenol adsorption: Adsorption isotherms, kinetics, and thermodynamic studies, Bioresour. Technol., 352 (2022) 127030.

[190] D. Mohan, K.P. Singh, V.K. Singh, Trivalent chromium removal from wastewater using low cost activated carbon derived from agricultural waste material and activated carbon fabric cloth, Journal of hazardous materials, 135 (2006) 280-295.

[191] H. Demiral, İ. Demiral, F. Tümsek, B. Karabacakoğlu, Adsorption of chromium(VI) from aqueous solution by activated carbon derived from olive bagasse and applicability of different adsorption models, Chemical Engineering Journal, 144 (2008) 188-196.

[192] H. Chen, A. Zhong, J. Wu, J. Zhao, H. Yan, Adsorption behaviors and mechanisms of methyl orange on heat-treated palygorskite clays, Ind. Eng. Chem. Res., 51 (2012) 14026-14036.

[193] R. Al-Qassar Bani Al-Marjeh, Y. Atassi, N. Mohammad, Y. Badour, Adsorption of methyl orange onto electrospun nanofiber membranes of PLLA coated with pTSA-PANI, Environ. Sci. Pollut. Res., 26 (2019) 37282-37295.

[194] E. Mertcan, N. Orakdogen, Bioactive interpenetrating hybrids of poly (hydroxyethyl methacrylate-co-glycidyl methacrylate): Effect of polysaccharide types on structural peculiarities and multifunctionality, Int. J. Biol. Macromol., (2023) 127807.

[195] Y. Ueno, K. Ajito, Y.Y. Maruo, Study of reactor-NO 2-gas diffusion in a porous glass chip by near-infrared Raman spectroscopy, Physical Chemistry Chemical Physics, 4 (2002) 2341-2345.

[196] I. Daou, Y. Dehmani, H. Moussout, D.S.P. Franco, J. Georgin, M.E. Bakkali, M. Tahaikt, A. Shaim, O. Zegaoui, S. Abouarnadasse, N. El Messaoudi, Adsorption of methyl orange and methylene blue from aqueous solutions on pure bentonite: statistical physical modeling provides an analytical interpretation, Environmental Monitoring and Assessment, 196 (2024) 1057.

[197] R. Lafi, W. Mabrouk, A.Y.A. Al Zahrani, A. Hafiane, S.M.A.S. Keshk, I. Montasser, Methyl Orange Adsorption onto Modified Extracted Cellulose from Olive Stones: Kinetics, Isotherms, Thermodynamic, Mechanism Studies, and Desorption, Water Conservation Science and Engineering, 9 (2024) 38.

[198] L. Dai, W. Zhu, L. He, F. Tan, N. Zhu, Q. Zhou, M. He, G. Hu, Calcium-rich biochar from crab shell: an unexpected super adsorbent for dye removal, Bioresource technology, 267 (2018) 510-516.

[199] S.A. Al-Thabaiti, E.S. Aazam, Z. Khan, O. Bashir, Aggregation of Congo red with surfactants and Ag-nanoparticles in an aqueous solution, Spectrochimica Acta Part A: Molecular and Biomolecular Spectroscopy, 156 (2016) 28-35.

[200] S. Ahmed, Y. Guo, D. Li, P. Tang, Y. Feng, Superb removal capacity of hierarchically porous magnesium oxide for phosphate and methyl orange, Environmental Science and Pollution Research, 25 (2018) 24907-24916.

[201] H. Chen, H. Yan, Z. Pei, J. Wu, R. Li, Y. Jin, J. Zhao, Trapping characteristic of halloysite lumen for methyl orange, Appl. Surf. Sci., 347 (2015) 769-776.

[202] S. Napolitano, Irreversible adsorption of polymer melts and nanoconfinement effects, Soft Matter, 16 (2020) 5348-5365.

[203] D. Gahane, D. Biswal, S.A. Mandavgane, Life cycle assessment of biomass pyrolysis, BioEnergy Research, 15 (2022) 1387-1406.

[204] P.S. Kumar, L. Korving, M.C.M. van Loosdrecht, G.-J. Witkamp, Adsorption as a technology to achieve ultra-low concentrations of phosphate: Research gaps and economic analysis, Water Research X, 4 (2019) 100029.

Appendix

A.1 Effect of pyrolysis temperature temperatures

To preliminarily investigate the effect of pyrolysis temperature, shrimp shell-derived adsorbents (SSs) were prepared through pyrolysis at various temperatures, specifically 400°C, 500°C, 600°C, and 700°C. The preparation method follows the procedure outlined in **Chapter 2.1: Section 2.1.2**. The 2 g of pyrolyzed samples were then exposed to 200 mL of Methyl Orange (MO) solution (10 mg/L) and stirred for 240 minutes. The removal efficiency was subsequently measured, and the results are presented in **Figure A.1**. It can be observed that as the temperature increases, the removal performance improves. The pyrolysis sample at 700°C shows a significant improvement compared to the 600°C sample. Therefore, 700°C was selected as the starting temperature for further investigation.

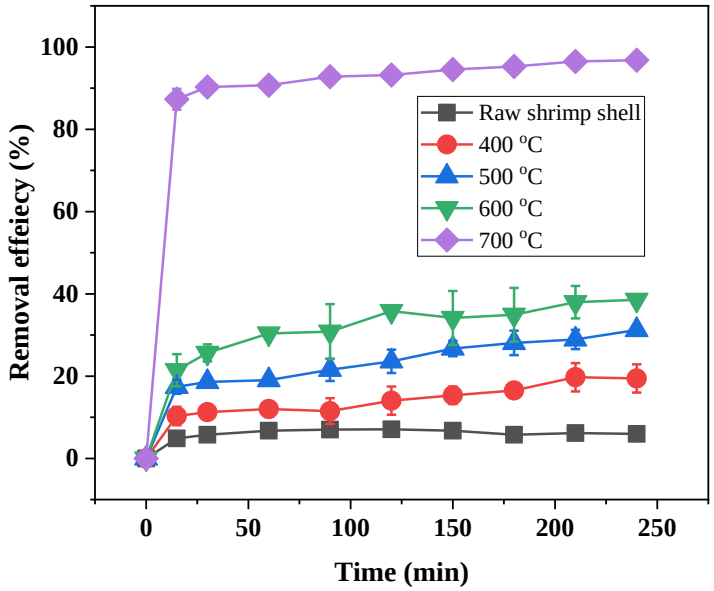

Figure A.1. Effect of pyrolysis temperate on MO removal efficiency.

A.2 Chemical cost of Shrimp shell derived adsorbent

This section provides a simplified calculation for the chemical costs associated with fabricating shrimp shell-derived adsorbents (SSs). It should be note that all chemicals used in the fabrication process for this study were of analytical reagent (AR) grade.

Step 1: Summary of chemical price list

AR grade chemicals	Volume per unit (g)	Price per unit* (円)
KOH pellet	500	2,100
▪ 500 g of KOH used: 1 kg of SSsK	500	2,100
$Ca(OH)_2$ powder	500	2,200
▪ 50 g of $Ca(OH)_2$ used :100 g of SSsCA	500	2,200

*Chemical price obtained from FUJIFILM Wako Pure Chemical

Step 2: Calculation of cost per unit

The cost per unit of adsorption production was calculated based on energy consumption for the production of 1 kg of SSs. Using data from a previous study, the electricity consumption for pyrolysis of waste wood as feedstock was determined to be 0.5 kWh per kg of product produced [203] (see Table A.3). Since the yield varies and affects the amount of energy required for production, the energy consumption was adjusted accordingly for each sample. For the alkali activation process, the electricity consumption of the magnetic stirrer (REXIM RSH-6DN, Japan) was 1.08 kWh. This was added to the energy required for pyrolysis to produce of SSaCA and SSsK.

Sample	**Electricity usage (kWh)**	**Time usage (h)**	**Yield (mg/time)**	**Electricity consumption for pyrolysis (kWh)**	**Electricity consumption for pyrolysis (kWh)/ 1 kg**
SSsN	0.5	1.75	17.44	0.88	50.17
SSsH	0.5	1.86	14.38	0.93	64.67
SSsCA	0.5	1.75	26.40	0.88	33.14
SSsK	0.5	1.75	21.02	0.88	41.63
Magnetic stirrer					
Power (kW)		**Time usage (h)**		**Electricity consumption for pyrolysis (kWh)/ 1 kg**	
1.08		2		2.16	

SSs sample	Chemical cost (円)	Electricity consumption of SSs				
		Alkali activation electricity consumption (kWh/kg)	Electricity consumption for pyrolysis (kWh/kg)	Total electricity consumption (kWh/kg)	Electricity rate in Japan** (円/kWH)	Total (円)/kg
SSsN	-	-	50.17	50.17	29	1455
SSsH	-	-	64.67	64.67		1535
SSsCA	2,100	2.16	33.14	35.30		3124
SSsK	2,200	2.16	41.63	43.79		3470
*Commercial activated carbon from coconut peel						1956

* Commercial activated carbon price obtained from Monotaro
**Electricity Rates for January 2024 by TEPCO Energy Partner, Inc., Japan

SSsN had the lowest total cost (1455 円/kg) since it only involved pyrolysis with no chemical costs. SSsCA and SSsK involved both alkali activation and pyrolysis, leading to higher costs due to additional chemical expenses. Therefore, the production of SSs is economically feasible, especially for samples SSsN and SSsH, which are more affordable compared to commercial activated carbon. However, if commercial-grade chemicals were used instead of AR grade chemicals, the cost could be significantly reduced. Moreover, with increased production scale, energy use might be decreased, making the process more cost-efficient. Recently, a small-scale pyrolysis plant with a 500 kg/day capacity, consuming only 3 kW to 9 kW of electricity, further enhancing its economic viability (source: Henan Doing Environmental Protection Technology Co., Ltd).

The detailed calculation of the adsorption cost per kg of PO_4^{3-} removed, using SSsN, which has the lowest production cost.

Given Data for SSsN:

- Production cost = 1,455 yen/kg adsorbent
- Adsorption capacity = 162.04 mg/g = 162.04 g/kg adsorbent

Step-by-Step Calculation:

1. **Convert Adsorption Capacity to kg PO_4^{3-} Removed per kg Adsorbent**

$$162.04 \text{ g } PO_4^{3-} = \frac{162.04}{1000} \text{ kg } PO_4^{3-}$$

2. **Calculate Adsorption Cost per kg P Removed**

$$\frac{\text{Production cost (yen/kg adsorbent)}}{PO_4^{3-}\text{removed (kg } PO_4^{3-}\text{/kg adsorbent)}}$$

$$\frac{1{,}455 \text{ yen}}{0.162 \text{ kg } PO_4^{3-}} = 8{,}981.48 \text{ yen/kg } PO_4^{3-}$$

3. **Convert to USD (Assuming 1 USD ≈ 150 yen)**

$$\frac{8{,}981.48 \text{ yen}}{150 \text{ yen/USD}} = 59.88 \text{ USD/kg } PO_4^{3-}$$

Therefore, the adsorption cost per kg of PO_4^{3-} removed in this study was calculated to be 59.88 USD/kg PO_4^{3-} using SSsN. When compared to other commercial porous adsorbent, which typically range from \$100 to \$200 per kg PO_4^{3-} for PO_4^{3-} removal [204], SSsN demonstrates a more cost-effective approach to reducing PO_4^{3-} levels.